ON THE CHARACTERISATION OF COPPER INDIUM DISELENIDE BASED PHOTOVOLTAIC DEVICES

NICOLAS MATOME THANTSHA

Submitted in partial fulfilment of
the requirements for the degree of

MAGISTER SCIENTIAE

in the Faculty of Science

at the Nelson Mandela Metropolitan University

January 2006

Supervisor: Doctor E E van Dyk

This work is dedicated to the memory of my uncle

Lesley Moloto

Acknowledgements

My sincere thanks to:

- My supervisor, Dr. E.E. van Dyk for his superb guidance, enthusiasm and encouragement throughout this project.
- Miss C. Radue for her valuable assistance and encouragement.
- Mr. F. Vorster, for his usefull discussions in some of the experimental work.
- Messrs D. O'Connor, J.B. Wessels for their technical assistance.
- My friend, Andile 'Ace' Gxasheka for his advice and encouragement.
- All members of the Physics department for their friendship, assistance and encouragement.
- The South African National Research Foundation, Vodacom and the Nelson Mandela Metropolitan University for their financial support.
- My biological mother, my uncle Joe and his wife Zodwa, Yoliswa Velebayi, Mr and Mrs Ramohlale, and the rest of the family, for their encouragement, financial support and sacrifices they made throughout my years of study.
- Finally, *for every mountain…thank you LORD.*

SUMMARY

Photovoltaic (PV) modules based on thin film systems of $CuInSe_2$ (CIS) and its alloys on low cost substrates are promising candidates to meet the long term efficiency, reliability and manufacturing cost goals. The attention to the CIS solar cell technology is because of the high absorption coefficient of the solar cell absorber layer.

Solar cells and PV modules are conventionally assessed by measuring the current-voltage characteristic of the device. This thesis presents an assessment procedure developed capable of assessing the device parameters with reference to I-V measurements. This thesis then characterizes the performance of the CIS based solar cells and modules in conjunction with other PV modules of different technologies such as crystalline Silicon modules by analyzing the light and dark I-V measurements of the devices. The light and dark I-V characteristics of PV devices were investigated and device parameters were extracted from the I-V data. The extraction and interpretation of these device parameters has a variety of important applications. It has been proven that the device parameters can be used for quality control during production and to provide insights into the operation of the PV devices, thereby improving the efficiency of the devices.

The assessment comprises light I-V measurements at standard test conditions (STC), irradiance dependence measurements, parasitic series and shunt resistances measurements and the dark I-V measurements of the PV devices.

The PV modules assessed comprise different technologies, namely, thin film based modules (CIS and a-Si) and multicrystalline Si and Edged-defined Film-fed Growth Si (EFG-Si). The dark I-V measurements results showed that the EFG-Si module has acceptable shunt (900 Ω) and series (0.4 Ω) resistances, thereby leading to the higher power output depicted from the light I-V measurements. The low quality cells of a-Si module were so low that the fill factor was the smallest (43%). In addition, the dark I-V measurements results revealed that CIS modules are less dependent to temperature at high voltages.

The results obtained in this study indicate that the knowledge of I-V characteristics provide an understanding of PV device performances. Furthermore, the understanding of the irradiance and temperature dependence of PV modules is essential in that it provides the prediction of the module performance when deployed outdoors.

Keywords: *Photovoltaic modules, current-voltage characteristics, device parameters, series and shunt resistances, effect of irradiance.*

CONTENTS

CHAPTER 1

INTRODUCTION

1.1 $CuInSe_2$ SOLAR CELLS TECHNOLOGY IN SOUTH AFRICA

One of the promising strategies of lowering the cost of photovoltaic (PV) energy is the use of thin film technologies. The significant advances that have been made around the world in the performance of $CuInSe_2$ (CIS) solar cells during the past few years have placed this material system as the leading candidate for the second generation thin film technology. Part of the main reason for the rapid development of CIS thin film technology is the discovery of a number of reaction processes that lead to highly efficient absorber layer formation [Alberts, 1998].

The high efficiency potential of thin film CIS solar cells has been demonstrated in a number of laboratories. Reports have shown that from about 2.5 billion people worldwide not connected to the electric network, 18 million are from South African rural communities. In South Africa thin film technology solar cells in recent years have attracted a number of higher education institutions like the University of Johannesburg (UJ), University of Pretoria (UP) and Nelson Mandela Metropolitan University (NMMU) [Weekend Post, 2005]. The collaborations between these institutions have seen South Africa as one of many countries advancing the thin film technology. In a joint research project of producing the CIS-based solar cells for commercialization; UP focuses on the fundamental of thin film PV materials, UJ prepares and manufactures the thin film PV devices, and the studies at NMMU focus on evaluation of the PV devices.

The use of thin film PV devices has attracted more researchers, and therefore more understanding is needed on how the thin film PV devices operate under certain conditions.

1.2 OBJECTIVES OF THIS STUDY

The main objective of this study was to characterize CIS solar cells and modules. The primary aim was to develop an assessment procedure capable of assessing the current-voltage (I-V) characteristics of solar cells and PV modules. This requires the study of dark and light I-V characterizations of solar cells and modules. In order to achieve the dark I-V characterization of PV devices, a system was built and commissioned. The light I-V characterization procedure utilized a system used at NMMU for indoor measurements. The dark and light I-V characteristic systems allowed the assessment of device parameters.

Four CIS modules were used in this study with two other modules of different technologies as references. These six PV modules were assessed subject to their I-V characteristics.

1.3 METHODOLOGY

Chapter 2 describes the fundamentals of the PV effect. The description is based on the source of light and how the light is absorbed by semiconducting materials. The solar radiation and its distribution are also discussed.

In chapter 3, I-V characteristics of a *p-n* junction solar cell are described. The descriptions include deriving the fundamental equations for the dark and light I-V characteristics of ideal and non-ideal solar cells. The effects of irradiance and parasitic resistances on I-V characteristics are also discussed.

Chapter 4 investigates the structure and formation of a CIS-based solar cell and how the current flows through it. The performance of CIS solar cells and modules is presented in the form of dark and light I-V characterization.

Chapter 5 deals with the dark I-V characteristics of solar cells and PV modules. It presents the results obtained using the dark I-V systems built at NMMU. The results presented include the effects of parasitic resistances and temperature on PV modules.

In chapter 6, the light I-V characteristics of PV modules are investigated. The results presented in this chapter include the effect of irradiance on PV modules and the determination of series and shunt resistances.

Chapter 7 gives the conclusions drawn from all the results obtained in this study. At the end, three appendices are presented. Appendix A presents the calibration results obtained using the system and Appendix B lists the algorithm of the software programme written for data acquisition and remote controlling of instruments. Appendix C, lists the research outputs associated with this study.

1.4 REFERENCES

Alberts, V. (1998), "Solar cell devices based on polycrystalline $CuInSe_2$ thin films," *South African Journal of Science*, **29**, no. 7.

Weekend Post (2005), "Top Scientists in R17m to spread the light," *published in the Weekend Post Newspaper January 2005*, pp 8.

CHAPTER 2

FUNDAMENTALS OF THE PHOTOVOLTAIC EFFECT

2.1 INTRODUCTION

In order to understand how a solar cell works, a little background theory in semiconductor physics is required. For simplicity, the description in this chapter is limited to describing the fundamentals of photovoltaic technology. The most common types of solar cells are based on the photovoltaic effect, which occurs when light falling on a two-layer semiconductor material produces a potential difference between the two layers. This chapter describes the nature of light and its source. The study also explains the theory behind photovoltaic effect.

2.2 WHAT IS LIGHT

"When the sun comes up in the morning living things wake from their sleep; animals busy themselves with the responsibilities of family life; plants unfold their leaves, drinking in the sunshine that powers the manufacturing processes of their living cells. Then the world goes to sleep as the sun drags the last of its rays over the edge of the horizon. The light is gone, and the activity slows" [Cook, 1957]. We know when light is there, and when its not, but how much do we really know about it at all – what is light?

In the ancient times, Greek philosophers thought about the mystery of light when they observed some of its peculiar behavior. According to their findings, light was a stream of particles emitted by a luminous object [Cook, 1957]. They recognized that light travels in a straight line and that a narrow ray of light striking on a mirror or a flat surface is reflected at an angle, similar to a ball bouncing off a wall.

For thousands of years, many philosophers debated the nature of light, using the particle theory as a starting point. In time, there were problems with this theory; it

was discovered that light rays actually bent as they moved from one transparent surface to another. For example, when light rays fall on to a glass surface at an angle, the rays change their direction and when they emerge on the other side of the glass they bend back to their original directions. It was not possible to explain the bending of light in terms of light as stream of particles.

It was only during the seventeenth century that English physicist Sir Isaac Newton established the modern understanding of light. In his series of experiments, he passed a narrow beam of sunlight through a triangular prism and allowed the light to shine on a screen after emerging from the other side of the prism. He observed a continuous band of coloured light; a spectrum formed by all the colours of the rainbow. Newton postulated that light coming from the sun consist of pure rays, for which each one causes a different colour sensation as it reaches the human eye.

2.3 PHOTONS

Nearly 200 years later, Einstein postulated that light was delivered in packets of definite sizes depending on its wavelength. When light strikes the metal of a photoelectric cell, each packet, or quantum of light causes an atom to emit an electron. The number of quanta reaching the metal is determined by the amount of light striking it (intensity) and the size of the quanta is fixed by the wavelength of the light beam.

Einstein, in his analysis on the photoelectric effect, showed that the emission of electrons from a metal that has been exposed to light can best be explained by assuming that the energy of a light beam is not evenly spread over the whole beam, but is concentrated in certain regions. These localized concentrations of energy which are propagated like particles, are called *photons* – the name which was proposed by Arthur Holly Compton in the 1920s [Ditchborn, 1976].

Moreover, the most readily measured property of photons is their energy. The different colours of light for example, are thought of as representing photons of

different energy. According to Einstein, the energy of the incoming photons, E_ν, is directly proportional to the frequency of the light, ν:

$$E_\nu = h\nu \tag{2.1}$$

where the proportionality constant, *h*, is known as Planck's constant.

Photons acting in countless billions form electromagnetic waves which we recognize as light. But, where do these photons, quanta of electromagnetic radiation originate?

2.4 THE POWER FROM THE SUN

The Sun, is a typical star at the center of our solar system, around which all its planets, including the Earth, rotate. It is the largest object in our solar system and contains approximately 98% of the total solar system mass. The distance between the Sun and the Earth is about 150 million km, and it takes light about eight minutes to reach Earth, making it the closest star to Earth [Cook, 1957]. The Sun has the characteristics listed in Table 2.1. The Sun's surface temperature is about 6000 *K*, while the temperature of its core reaches several million kelvin.

Table 2.1: *Characteristics of the sun.*

Mass (kg)	1.989×10^{30}
Equatorial radius (km)	6.96×10^{5}
Mean density (gm/cm^3)	1.410
Mean surface temperature (K)	6.0×10^{3}
Age (billion years)	4.5

The Sun is the source of light and heat for our solar system. Deep in the core of the Sun, where temperatures reach millions of kelvin, energy is liberated through thermonuclear fusion. During the fusion process, large amounts of hydrogen ions fuse together, creating helium and emitting energy in the form of heat and electromagnetic radiation. The heat remains in the Sun and is instrumental in

maintaining the thermonuclear reaction. The electromagnetic radiation (including visible light, infra-red light, and ultra-violet radiation) streams out into space in all directions, becoming the driving force for all life in our solar system.

2.4.1 Solar radiation

During the fusion process, however, a steady state is achieved because the Sun radiates energy from its surface into outer space. The total radiation power, *J*, may be calculated using Stefan's Law which states that the total energy radiated, P, per unit surface area, *A*, of a black body in unit time is proportional to the fourth power of its thermodynamic temperature, *T*:

$$J \equiv \frac{P}{A} = \sigma T^4 \tag{2.2}$$

where $\sigma = 5.67 \times 10^{-8} Wm^{-2} K^{-4}$ is the Stefan-Boltzman constant,

$$A = 4\pi R^2$$

where *R* is the radius of the Sun.

The Sun does not radiate uniformly at all frequencies. Solar radiation, S_λ, is described by Planck's Law which states that the spectral radiation is proportional to the inverse of the wavelength to the power five:

$$S_\lambda = \frac{2\pi c^2 h}{\lambda^5}\left(\frac{1}{e^{hc/\lambda kT} - 1}\right) \tag{2.3}$$

where: λ is the wavelength, *k* the Boltzmann constant, *h* Planck's constant, *c* the speed of light, and *T* is the temperature.

Total power radiated by the Sun is $3.83\times10^{26}W$. The solar radiation outside the Earth's atmosphere is called extraterrestrial radiation and the total energy reaching the atmosphere per second is $1.76\times10^{5}TW$, which translates to 1353 W/m^2.

2.4.2 Direct and Diffuse radiation

The amount of extraterrestrial radiation from the Sun surfacing the Earth is affected by atmospheric absorption and reflection of sunlight. Figure 2.1 illustrates the factors that contribute to the attenuation of extraterrestrial radiation.

Molecules in the Earth's atmosphere absorb part of the direct radiation forming isolated lines throughout the radiation spectrum. Some of these molecules e.g. air molecules, may also scatter higher energy beams (blue lines), giving rise to the blue appearance of the sky.

It is evident from figure 2.1 that only a part of the extraterrestrial radiation reaches the Earth's surface as direct radiation. Other incident light is a result of diffuse solar radiation due to the reflection by atmospheric constituents like clouds. Some of the reflected beams are scattered back into space. The incoming solar radiation on a horizontal plane at the Earth's surface, therefore, consists of both direct and diffuse radiation.

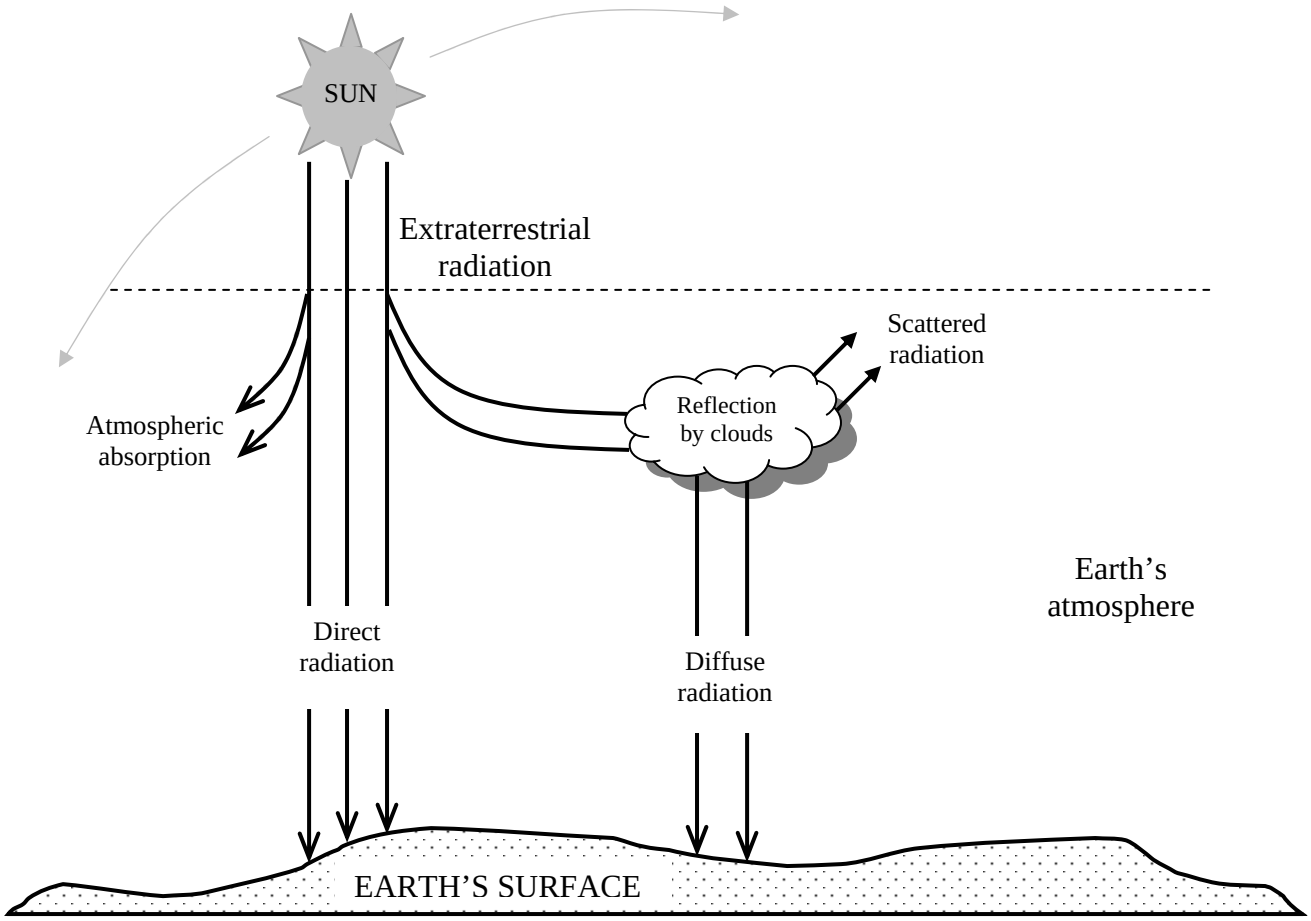

Figure 2.1: *Solar radiation in the atmosphere.*

2.4.3 Distribution of solar radiation

According to McVeigh (1977), a common method of describing relative levels of solar radiation, is Air Mass (AM). Air Mass is the path length of radiation through the atmosphere, as illustrated in figure 2.2. The Air Mass is the ratio of A0 to B0. The zenith path, B0, defines the unity of air mass (AM 1). The sun is at a zenith when it is directly overhead perpendicular to Earth's surface. The angle, θ, formed between zenith position and the sun ray, is called the zenith distance. AM 0 refers to the extraterrestrial radiation, that is, radiation before it gets attenuated by Earth's atmosphere. At $\theta \approx 48.2^0$, the equivalent of 1.5 of the noontime air mass (AM 1.5) attenuates the sunlight [Zweibel, 1990]

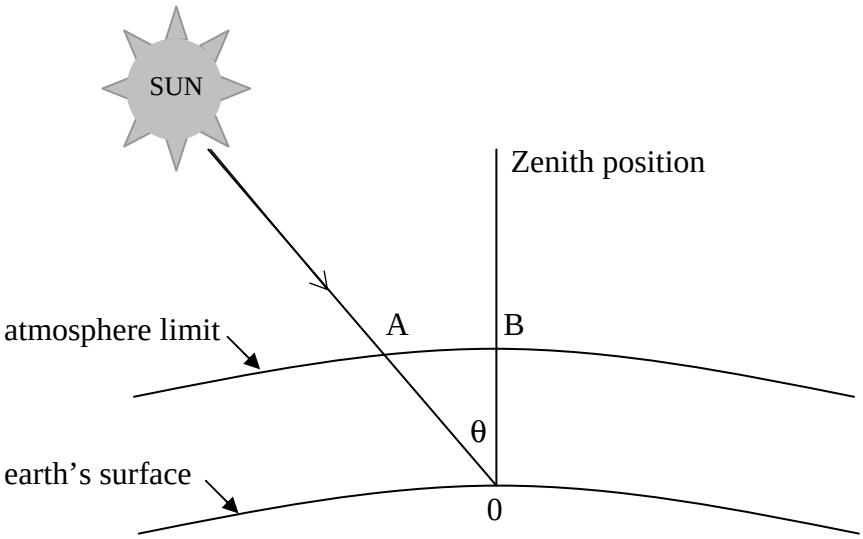

Figure 2.2: *Radiation at the surface of the earth.*

The total specific radiant flux per area that reaches Earth's surface is called irradiance and is measured in W/m^2. Extraterrestrial sunlight has an irradiance of about 1353 W/m^2 and about 300 W/m^2 is lost to reflection and atmospheric absorption, leaving only about 1000 W/m^2 irradiance incident on the Earth's surface.

The radiation of the surface of the Sun is described by a blackbody radiation at a temperature of about 6000 K with the peak intensity being in the spectral region detected as visible light, as shown in figure 2.3. Extraterrestrial radiation (AM0) and AM 1.5 spectrums are also shown in figure 2.3. AM 1.5 indicates that the direct beam path of the Sun's rays travels through 1.5 times the thickness of the Earth's atmosphere. The AM 1.5 spectrum is then regarded as the spectral distribution with standard solar irradiance of 1000 W/m^2.

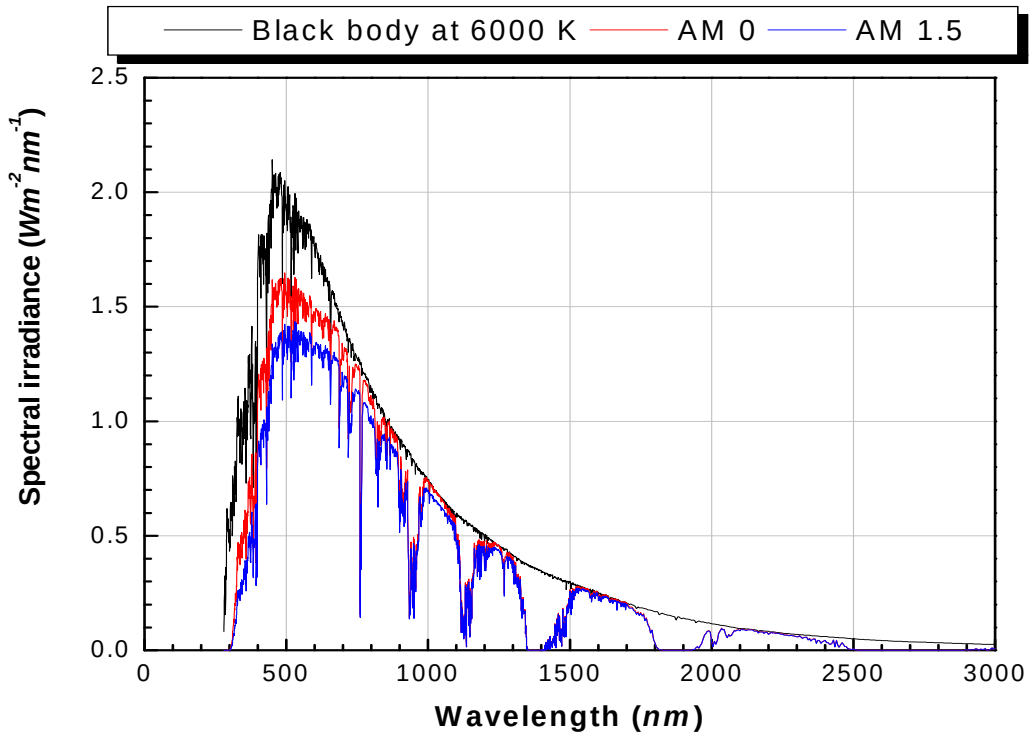

Figure 2.3: *Spectral distribution of solar radiation.*

2.5 THE *p-n* JUNCTION.

When a uniformly *p-type* (excess of holes) semiconductor is joined to a uniformly *n-type* (excess of electrons) semiconductor, the configuration produces the *p-n junction*. The *p-* and *n-* type semiconductor materials are shown in figure 2.4a with their respective energy level diagrams. Note that in the *p-type* material the Fermi level is near the top edge of the valence band and near the bottom edge of the conduction band in the *n-type*. There are excess conduction band electrons compared to holes in the *n-type* material, while the hole concentration is greater in the *p-type* material.

The difference in carrier concentrations sets up an initial diffusion current in which electrons diffuse from the *n-region* to the *p-region* and holes diffuse from the *p-region* to the *n-region*. During redistribution, the carriers near the junction edge of the two materials diffuse away leaving behind ionized impurities. Donors on the *n-*

side give electrons and leave behind a positively charged ion, and acceptors on the *p-side* give up the extra holes (taking on extra electrons) leaving behind a negatively charged ion. The free carrier distribution establishes a depletion region around the junction where there are no free carriers present [Kano, 1998]. The depletion region is often known as the space charge region because charged ions are left behind in this region, as shown in figure 2.4b.

The free donor and acceptor impurity ions in the depletion region are no longer balanced by the free charges that were there. As a result, an electric field builds up directed from positive charges on the *n-side* towards the negative charge on the *p-side*. Free carriers in the field experience a force and a drift current is created that opposes the diffusion current. As diffusion continues, the electric field gets stronger and the drift current increases. At some point the drift current balances the diffusion current, reaching thermal equilibrium in which there is no net current flow.

The conventional energy level diagram shown in figure 2.4b illustrates the movement of free carriers. In this situation the electrons need extra energy to move up the step from *n-type* to *p-type* across the junction. Coming the other way, electrons drop down into the *n-type* region with extra kinetic energy. This means electrons rather move to *n-side* than *p-side*. The size of this energy barrier can be defined in terms of a junction voltage V_{bi}. This means the amount of energy converted from kinetic energy to potential energy when electrons cross the depletion region, is eV_{bi} where e is the charge on a single electron. This result in electrons gathered together in the *n-type* material. Similarly, free holes gather in the *p-type* material.

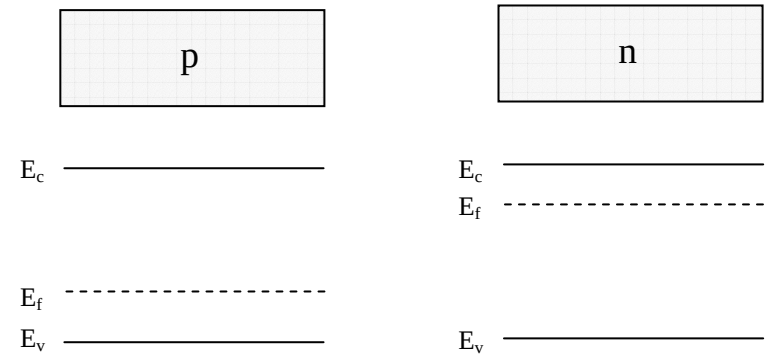

(a)

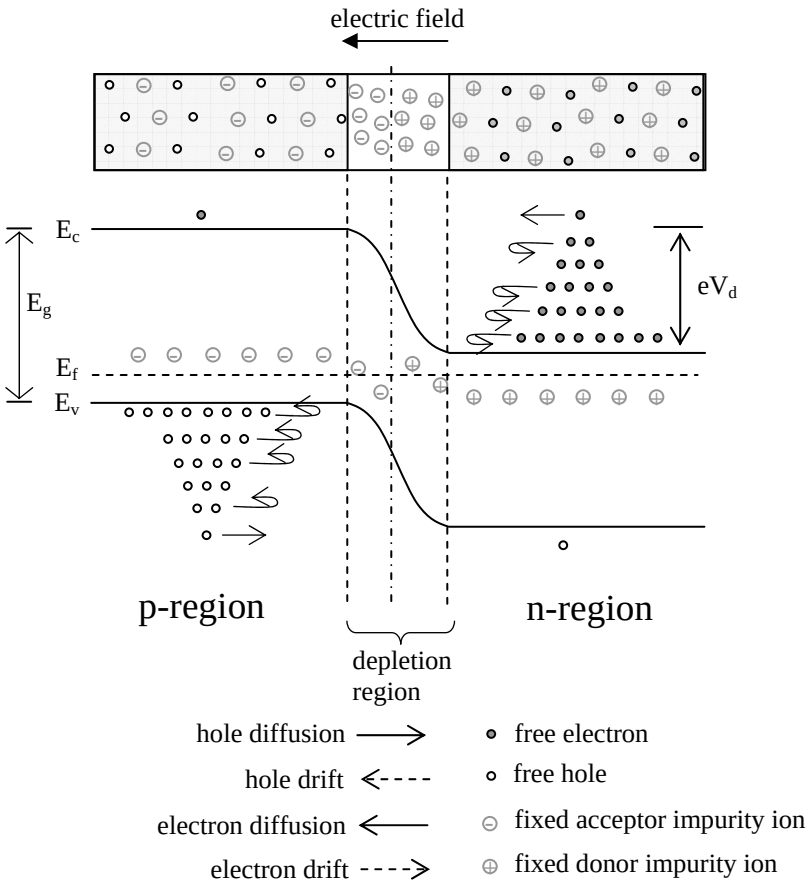

(b)

Figure 2.4*: a) Isolated p- and n-type semiconductor materials, b) Combined p- and n-type semiconductor materials showing carriers flow [Kano, 1998].*

By definition, V_{bi}, is the total difference between electrostatic potentials of the *n-type* and *p-type* neutral regions [Sze, 1981]:

$$V_{bi} = \frac{kT}{q} \ln\left(\frac{N_A N_D}{n_i^2} \right) \tag{2.4}$$

with: $q =$ elementary charge.

$k =$ Boltzman's constant.

$T =$ absolute temperature.

$n_i =$ intrinsic carrier concentration.

N_A and $N_D =$ concentrations of immobile acceptor and donor ions respectively.

The *p-n* junction is the key to the successful operation of the photovoltaic device as well as many other semiconductor devices.

2.5.1 Equilibrium *p-n* junction.

At thermal equilibrium, the net current flowing through the *p-n* junction is zero [Sze, 1985]. This implies that for each charge carrier, diffusion current due to the concentration gradient is compensated by a drift current of equal magnitude. Thus, the net electron current density, J_n, at steady state is given by:

$$\begin{aligned} J_n &= J_n(drift) + J_n(diffusion) \\ &= q\mu_n nE + qD_n \frac{dn}{dx} \\ &= 0 \end{aligned} \tag{2.5}$$

where: $\mu_n =$ electron mobility.

$n =$ electron concentration.

$E =$ electric field.

$D_n =$ diffusion coefficient.

Similarly, net hole current density $J_p = 0$ at thermal equilibrium.

2.6 DEVELOPMENT OF PHOTOVOLTAIC TECHNOLOGY

In 1839, Edmond Becquerel discovered the concept known as the photovoltaic (PV) effect which describes the release of positive and negative charge carriers in a solid when light strikes its surface. PV is the science of turning energy produced by the sun into electricity. However, it was not until 1883 that the first solar cell was built by Charles Fritts, who coated the semiconductor selenium with an extremely thin layer of gold to form the junction for the device that was only around 1% efficient. After Shockley had developed a model for the *p-n junction*, scientists at Bell laboratories prepared a solar cell in 1954. To understand PV power, one must understand the fundamentals of how the device is utilized to convert sunlight into electricity.

2.7 THE IRRADIATED PHOTOVOLTAIC CELL

In practice, a *p-n junction* is formed such that electrical contacts can be made on the two ends of the junction to form a two-terminal device called a junction diode which conducts an electric current in one direction and blocks it in the other. The electrical contacts enable the connections to external circuit.

When light is incident on a *p-n junction* device, the thermal equilibrium of the device is disturbed. Incident photons on a solar cell are absorbed within the interior of the *p-n junction* and as a result, some of the bound electrons in valence band acquire sufficient energy from the photon to escape from their atoms, becoming free electrons and leaving holes behind. This is known as the generation of electron-hole pairs. Only photons with energy greater than or equal to the energy of the band gap of the material get absorbed and contribute to the electron-hole pair generation.

2.8 PHOTON ABSORPTION

When a photon is absorbed in the *p-n* junction, its energy is transferred to an electron in the crystal lattice [Messel, 1975]. This electron is normally at the upper level of the

valence band and is tightly bound in covalent bonds between neighbouring atoms. It is therefore unable to move far. After the absorption of energy from the photon the electron then makes the transition to the bottom level of the conduction band and becomes a free carrier. The bond from which the electron was ejected is left with a mobile hole.

The transition of electrons from the valence band to conduction band is heavily dependant on the detailed band structure of the semiconductor. Semiconductors for which the minimum of the conduction band occurs at the same wavevector, k, as the maximum of the valence band, are referred to as the direct bandgap semiconductors. The energy band for a direct bandgap semiconductor is shown in figure 2.5a. Figure 2.5b, illustrates an indirect bandgap semiconductor, where the minimum of the conduction band does not occur at the same wavevector as the maximum of the valence band.

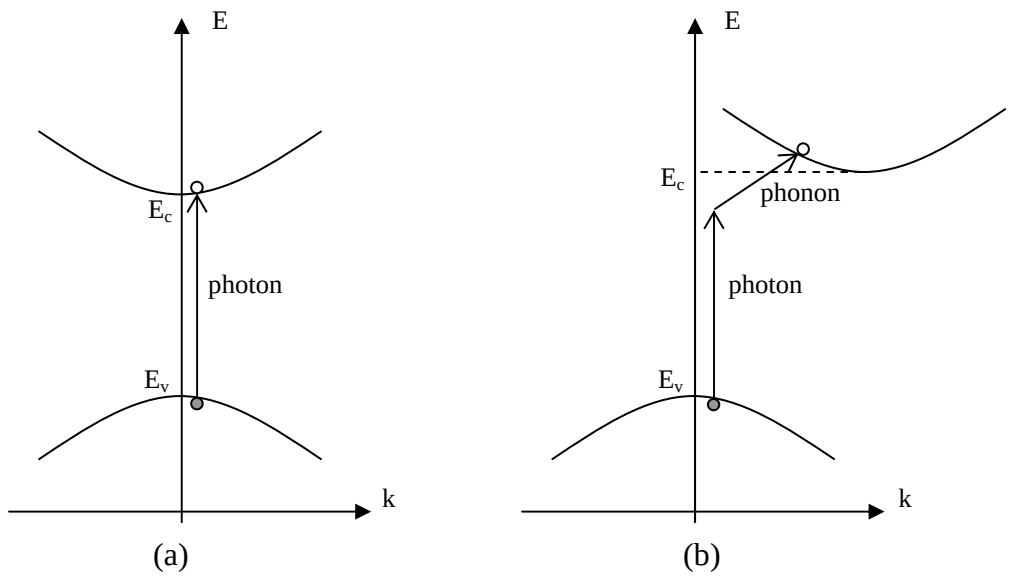

Figure 2.5: *E-k diagrams: a) Absorption of photon in a direct bandgap semiconductor, b) Photon absorption in an indirect semiconductor.*

Photon absorption occurs if an empty state in the conduction band is available. This is when the energy and momentum of the empty state equals the energy of an electron plus incident photon energy. Because photons travel at the speed of light, they have little momentum relative to their energy. The electron, therefore, makes an almost

vertical transition in the *E-k* diagram. However, for an indirect bandgap semiconductor, a simple interaction of an incident photon with an electron in the valence band will not provide the correct energy and momentum corresponding to that of an empty state in the conduction band. As a result, absorption of the photon requires the help of another particle, namely a phonon which is a particle associated with lattice vibrations. Phonons have small energy and large momentum compared to that of a photon. Conservation of energy and momentum can therefore be obtained in the absorption process as illustrated in figure 2.5b. Because the absorption process involves a phonon in addition to the electron and photon, the probability of having an interaction is lower than a simple electron-photon interaction in a direct bandgap semiconductor.

Not all incoming photons are absorbed. There are several reasons for this. Part of the light is reflected at the surface of the solar cell, or passes through the cell. In some cases, electrons and holes recombine before arriving at their destination for collection. Moreover, the intensity of sunlight at the surface of a semiconductor device can be described by the absorption equation given by Beer's Law which states that the intensity I of the light at the depth x in the semiconductor, is given as:

$$I(x) = I_0 e^{-\alpha x} \tag{2.4}$$

where I_0 is the intensity of the light before hitting the surface of the material, and α is the absorption coefficient of the material. Thus, if the energy of the incident photon is lower than the energy bandgap of the material, the electron won't have sufficient energy to make the band gap transition, and hence no electron-hole pair can be generated.

Those electrons and holes created by the photons will eventually disappear by recombining with each other unless they are physically separated into different regions of the material. Due to the built-in electric field, electrons accumulate in the *n-type* region as negative charge carriers, and in the *p-type* region holes accumulate as positive charge carriers [Lorenzo, 1994]. If an external load is connected, as shown in

figure 2.6, electrons will flow externally from *n*-type side to the direction of the *p*-type side. This movement constitutes a current through the load.

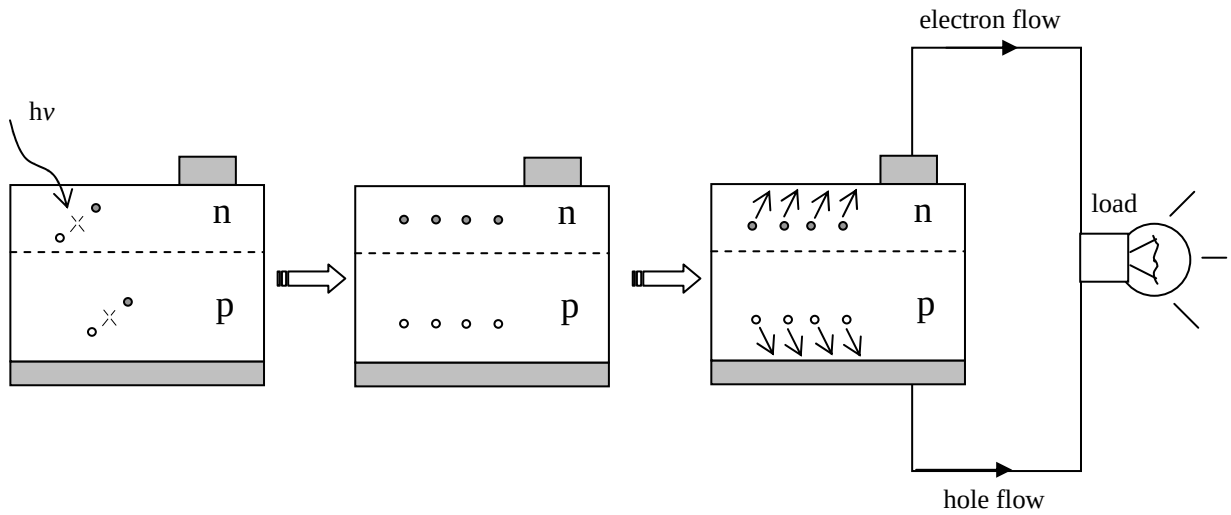

Figure 2.6: *The illustration of electron-hole pair generation and how they are utilized to drive the current through the load.*

2.9 SUMMARY

The objective of this chapter was to discuss the nature of solar energy and the fundamentals of photovoltaic technology. An explanation of photovoltaic technology was discussed with special reference to the photovoltaic cells, which by their nature, convert solar radiation to electricity. The science of turning solar energy into electric energy, the photovoltaic effect, was discussed. The solar spectrum as similar to black body at 6000 K, was discussed with reference to the extraterrestrial and AM 1.5 spectra.

It was discussed that only a fraction of the total solar radiation reaches the Earth's surface. The radiation that does reach the Earth's surface is the indirect source of nearly every type of energy used today. The PV effect depends on incident light for the generation of electron-hole pairs. The dependence of photon absorption on the band structure of the semiconductor was also presented together with the science of solar cells with reference to the thermal equilibrium of a *p-n* junction.

2.10 REFERENCES

Cook J.G. (1997). *We live by the sun*. George G. Harrap and Co. LTD. London, pp 19-24.

Ditchborn R.W. (1976). *Light*. Academic press. **1**, pp 62

Kano K. (1998). *Semiconductor devices*. Prentice-Hall, Inc. New Jersey, pp 121-135.

Lorenzo E. (1994), Translated by Philip Davies, *Solar Electricity: Engineering of Photovoltaic Systems*, PROGENSA.

Messel H and Butter S.T. (1975). *Solar Energy*. Pergamon Press. New York, pp 99-102.

McVeigh J.C**.** (1977). *Sun Power*. Pergamon Press. New York.

Sze S.M. (1985), *Physics of Semiconductor Devices*, John Wiley and Sons, pp 71-74.

Zweibel K. (1990), *Harnessing Solar Power*, Plenum Press, pp 95.

CHAPTER 3

CURRENT-VOLTAGE CHARACTERISATION OF SOLAR CELLS AND PHOTOVOLTAIC MODULES

3.1 INTRODUCTION

The preceding chapter introduced the physics of an illuminated *p-n* junction formed when *p*-type semiconductor material combines with similar lattice *n*-type semiconductor material. The basic property of a *p-n* junction diode is that it has the ability to conduct an electric current in one direction and block it in the other. Further understanding of photovoltaic (PV) technology can be gained by interpreting the current-voltage (I-V) characteristics of a *p-n* junction. Solar cell I-V characterisation measures current and voltage, and from these measurements, the performance parameters of solar modules, e.g. efficiency, can be obtained. These parameters can be used for quality control during production and also to provide insights into the operation of the devices.

The objective of this chapter is to discuss performance parameters of *p-n* junction devices and the factors that affect their effective operation. The I-V characterisation of solar cells and modules can be performed under illumination or under dark conditions. Dark I-V characterisation yields information regarding diode parameters and parasitic resistances, while light I-V characterisation is used mainly for determining performance parameters, e.g. open-circuit voltage, short circuit current, power output and the fill factor of the module.

The I-V characteristics of both ideal and non-ideal *p-n* junctions will be discussed. The description in an ideal case is based upon the unbiased and biased *p-n* junction. Models describing ideal and non-ideal solar cells, are described and an explanation of the operation of the device is presented.

3.2 Current-Voltage characteristics of an ideal *p-n* junction

A *p-n* junction has specific characteristics under low-level recombination rates. In characterising ideal *p-n* junctions, we assume that [Goetzberger, 1994, and Sze, 1985]:

1. The regions outside boundaries are neutral;
2. The injected minority carrier concentrations are small compared to the majority carrier concentrations;
3. There are no generation and recombination processes in the space charge region (SCR). This implies that carrier currents remain constant across the SCR boundaries;
4. Carrier concentrations at the junction boundaries are related through V_{bi}, the buit-in potential.

3.2.1 Unbiased *p-n* junction

When a *p-n* junction is unbiased, no external voltage is applied to the device and the situation remains at thermal equilibrium as discussed in section 2.5. Considering the above assumptions, the majority carrier concentration is equal to the doping concentration in both *p*- and *n*-regions. Therefore, equation 2.4 can be modified to,

$$V_{bi} = \frac{kT}{q}\ln\left(\frac{p_{p0}}{p_{n0}}\right)$$

or

$$p_{p0} = p_{n0}\exp\left(\frac{qV_{bi}}{kT}\right) \tag{3.1}$$

where p_{p0} and p_{n0} are the hole concentrations at thermal equilibrium in the *p*- and *n*-regions, respectively.

Thus, from equation 3.1 the majority carrier concentration at the junction boundaries increases exponentially by the factor $\exp\left(\frac{qV_{bi}}{kT}\right)$.

3.2.2 Forward biased *p-n* junction

If an electric bias with $V > 0$ is connected at both ends of *p-n* junction in such a way that the positive terminal is connected to the *p*-side and the negative terminal to the *n*-side, then the concentration of free carriers increases. Figure 3.1a illustrates the flow of free carriers within the biased *p-n* junction. The applied voltage reduces the potential barrier across the SCR, and as a result more electrons from *n*-side can travel to the *p*-side. Similarly, holes are injected from the *p*-side to the *n*-side. The reduction of the potential barrier decreases the width of depletion region, due to the weakening of drift current. That is, diffusion current dominates in the net current (equation 2.5). It is assumed that the carrier concentrations at the junction boundaries are related by the potential barrier. Therefore, equation 3.1 can be modified to:

$$p_p = p_n \exp\left(\frac{q(V_{bi} - V_a)}{kT}\right) \tag{3.2}$$

where p_p and p_n are the nonequilibrium hole concentrations at the junction boundary in the *p*- and *n*-sides, respectively.

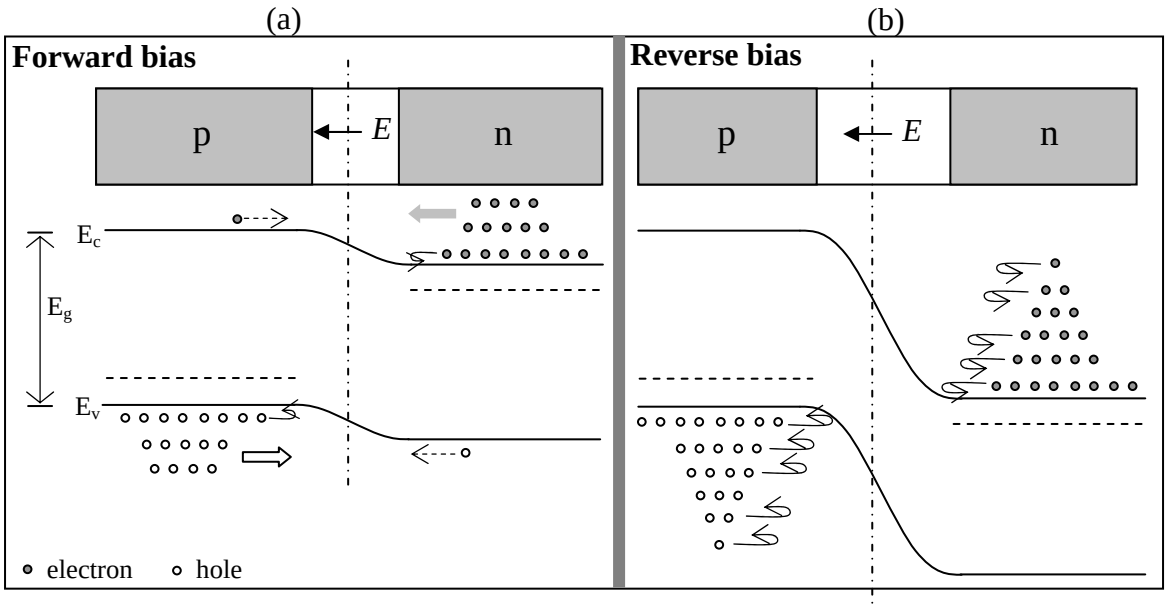

Figure 3.1: *Structures and Energy band diagrams of the p-n junction under; (a) forward bias and (b) reverse bias, showing change in SCR.*
(This chapter uses the following notation ∘ electrons ∘ hole)

3.2.3 Reverse biased *p-n* junction

During reverse bias, the SCR widens and hence there is an increase in the potential barrier height, as shown in Figure 3.1b. The diffusion currents are reduced by the resistances due to the higher potential barrier, resulting in a small reverse leakage current. As shown in figure 3.1b, almost all the carriers are reflected back to the side where they are the majority. For solar cell applications, reverse biasing is not relevant, but the low reverse current or saturation current, plays an essential part in the physics of solar cells.

3.2.4 Ideal diode current

When the external voltage V_a is applied across the *p-n* junction, as shown in Figure 3.2, the SCR and the built-in potential, V_{bi}, are modified as discussed in section 3.2.2. This results in a net current, I_{ideal}, flowing through the *p-n* junction device. Consider the modified depletion region edges to be x_n' and $-x_p'$ as illustrated in figure 3.2.

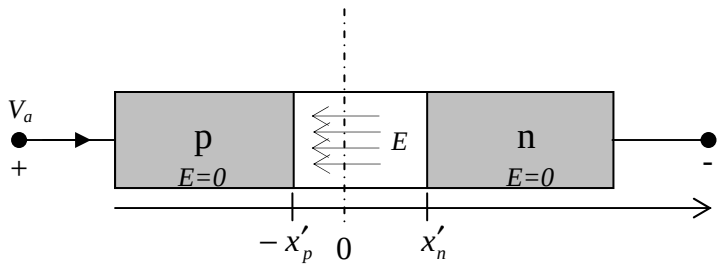

Figure 3.2: *Forward biased p-n junction showing modified SCR.*

The minority carrier concentrations at the edges of the depletion region, x_n', are given by,

$$p_n(x_n') = p_{n0} \exp\left(\frac{qV_a}{kT}\right)$$

or

$$p_n(x_n') - p_{n0} = p_{n0}\left[\exp\left(\frac{qV_a}{kT}\right) - 1\right] \tag{3.3a}$$

and

$$n_p(-x_p') - n_{p0} = n_{p0}\left[\exp\left(\frac{qV_a}{kT}\right) - 1\right] \tag{3.3b}$$

Equations 3.3 show that there is an excess population of minority carrier at the junction edges. Thus, the minority carrier densities at the edges of SCR are modified [Sapoval and Hermann, 1995]. Let the deviations be,

$$p'(x_n') = p_n(x_n') - p_{n0} = p_{n0}\left[\exp\left(\frac{qV_a}{kT}\right) - 1\right] \tag{3.4}$$

and

$$n'(-x_p') = n_p(-x_p') - n_{p0} = n_{p0}\left[\exp\left(\frac{qV_a}{kT}\right) - 1\right] \tag{3.5}$$

where p' and n' are modified carrier densities.

Since for low-level injection, $E \approx 0$, therefore, the carrier current densities at x_n' and $-x_p'$ are,

$$J_h = q\frac{D_h}{L_h}p'(x_n') \text{ for } x \geq x_n'$$

$$J_e = q\frac{D_e}{L_e}n'(-x_p') \text{ for } x \leq -x_p'$$

where: D_h and D_e are diffusion constants for holes and electrons respectively

and L_h and L_e are diffusion lengths for holes and electrons respectively

Ignoring recombination of holes and electrons in the SCR, the equations can be written as:

$$\begin{aligned} J_h(x_n') &= J_h(-x_p') \\ &= q\frac{D_h}{L_h}p_{n0}\left[\exp\left(\frac{qV_a}{kT}\right) - 1\right] \end{aligned} \tag{3.6}$$

and

$$J_e(-x_p') = J_e(x_n')$$
$$= q\frac{D_e}{L_e}n_{p0}\left[\exp\left(\frac{qV_a}{kT}\right)-1\right] \tag{3.7}$$

The total ideal carrier current density is the sum of equation 3.6 and 3.7, and the total ideal current is therefore deduced as:

$$I_{ideal} = A\left[J_h(x_n') + J_e(-x_p')\right]$$
$$= qA\left(n_{p0}\frac{D_e}{L_e} + p_{n0}\frac{D_h}{L_h}\right)\left[\exp\left(\frac{qV_a}{kT}\right)-1\right]$$

or

$$I_{ideal} = I_0\left[\exp\left(\frac{qV_a}{kT}\right)-1\right] \tag{3.8}$$

Where; $I_0 = qA\left(n_{p0}\frac{D_e}{L_e} + p_{n0}\frac{D_h}{L_h}\right)$, the reverse saturation current which depends on the doping concentration.

3.3 Current-Voltage characteristics of non-ideal *p-n* junction

In contrast to the ideal case, in a non-ideal *p-n* junction, recombination and generation of electrons and holes occurs. In a forward biased *p-n* junction, carrier concentrations in the SCR increase to above their equilibrium values, which give rise to carrier recombination in the region, as illustrated in Figure 3.3. During forward biasing electrons are injected from the *n*-region to *p*-region where they become minority carriers and eventually they may recombine with the existing majority carriers [Mazer, 1997]. The same effect occurs for holes in the *p*-region. This effect gives rise to currents in both *n*- and *p*-regions. Also, recombination of carriers in the SCR constitutes the current in that region. Therefore, the total diode current is given as the

sum of currents due to the recombination of carriers both in the SCR and in the quasi-neutral regions. Equation 3.8 is thus modified to,

$$I_{nonideal} = I_{01}\left[\exp\left(\frac{qV_a}{nkT}\right)-1\right] + I_{02}\left[\exp\left(\frac{qV_a}{nkT}\right)-1\right] \qquad (3.9)$$

where: I_{01} = the reverse saturation current due to recombination of carriers in the quasi-neutral regions;

I_{02} = the reverse saturation current due to recombination and generation of carriers in the SCR; and

n = the ideality factor.

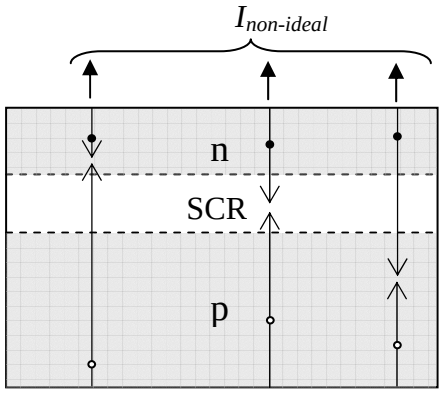

Figure 3.3: *Forward biased of a non-ideal p-n junction.*

Equation 3.9 describes the semiconductor diode when voltage losses across and within the quasi-neutral regions are neglected. For an ideal solar cell, the plot of *log(I)* versus applied voltage V_a would yield straight line provided $V >> \frac{nkT}{q}$ [Schroder, 1998; 201]. Non-idealities will result in the curve deviating from linearity in low and high current regions and is addressed in the next section.

3.4 Current-Voltage characterization of a solar cell under dark conditions: effect of series and shunt resistance.

When there is a current flow through a *p-n* junction solar cell under forward bias, there are resistances within the *p-n* junction device that impede the current carriers. These are called parasitic resistances and cause voltage losses across the device. In this section the equations developed in the preceding section are used to discuss the effect of parasitic resistances on the I-V characteristic of a solar cell under dark conditions.

When free carriers get separated by the built-in field within a *p-n* junction, electrons travel to the surface of the *n*-region to be collected, and holes drift to the surface of the *p*-side. Electrons travel long distances to reach metal contacts. Along the way they may experience some series resistance. This resistance results in carriers losing their potential, and they may not reach the metal contacts. This series resistance is due to the contact between the metal and the semiconductor, the resistivity of the semiconductor (quasi-neutral regions have an inherent resistance determined by the doping and dimensions of the regions), or the series resistance of the connecting wires. The series resistance of a solar cell is represented by R_s in figure 3.4.

At low current levels, the voltage drop, IR_s, across the series resistance is negligible compared to the applied voltage, V_a, across the depletion region. This is due to the strong built-in field that moves the carriers to the surfaces of the quasi-neutral regions. At high current levels, however, due to the weak electric field, carriers reduce speed and therefore increase the chance of experiencing series resistance. Series resistance effectively increases the applied voltage V_a relative to the internal voltage *V*. Thus,

$$V_a = V + IR_s \tag{3.10}$$

where I is the diode current and R_s is the series resistance.

Another voltage loss is due to the parallel paths within the lattice. These paths are referred to as shunts and are located within the electric field region. They are likely to impede the flow of carriers. In figure 3.4, the total shunt resistance is represented by R_{sh}. At lower current levels, built-in fields are stronger and the shunts tend to allow leakage of currents. In the bulk of the semiconductor, away from the field region, shunts may interact with passing carriers. The leakage current reduces the solar cell current to below its optimum whenever a carrier is lost due to shunting. This leakage current, I_{sh}, is related to the applied voltage by,

$$I_{sh} = \frac{V_a}{R_{sh}} \tag{3.11}$$

Incorporating the parasitic resistance effects, the equivalent model shown in figure 3.4 describes the solar cell. The model takes into account mechanisms due to the diffusion and recombination of carriers, and parasitic resistance. The dark current I_{dark}, is the sum of the currents due to these transport mechanisms and leakage current.

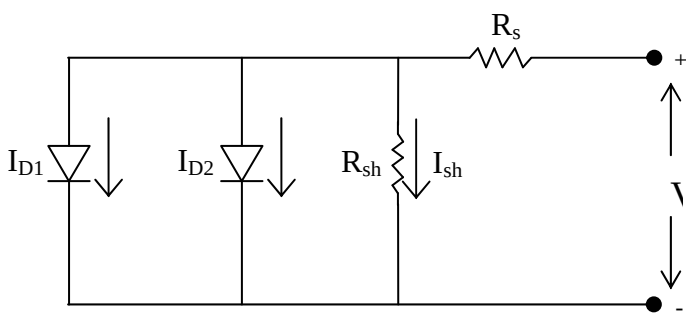

Figure 3.4: *An equivalent circuit of a non-ideal solar cell.*

The fundamental equation corresponding to the model in figure 3.4 gives I_{dark},

$$I_{dark} = I_{nonideal} - I_{sh} \tag{3.12}$$

and substituting equation 3.10 into equation 3.9 gives:

$$I_{non-ideal} = I_{01}\left[\exp\left(\frac{q(V+IR_s)}{n_1 kT}\right)-1\right] + I_{02}\left[\exp\left(\frac{q(V+IR_s)}{n_2 kT}\right)-1\right] \tag{3.13}$$

Substituting equation 3.11 and equation 3.13 into equation 3.12:

$$I_{dark} = I_{01}\left[\exp\left(\frac{q(V+IR_s)}{n_1 kT}\right)-1\right] + I_{02}\left[\exp\left(\frac{q(V+IR_s)}{n_2 kT}\right)-1\right] - \frac{(V+IR_s)}{R_{sh}} \tag{3.14}$$

with: I_{01} = the ideal diode saturation current.

I_{02} = the non-ideal diode saturation current.

n_1 and n_2 = diode ideality factors.

Consider figure 3.5; which is a typical dark I-V curve of a solar module. At low current levels the effect of shunting dominates. In this range the diode ideality factor $n_2 \approx 2$, and this implies that the recombination of carrier in the SCR is predominant [Luque, 2003]. Thus the second and third terms in equation 3.14 dominate. At higher current levels with $n_2 \approx 2$, and the effects of series resistance dominate the I-V characteristic. At mid range levels, the ideal case is predominant and the first term in equation 3.14 dominates, yielding $n_1 \approx 1$.

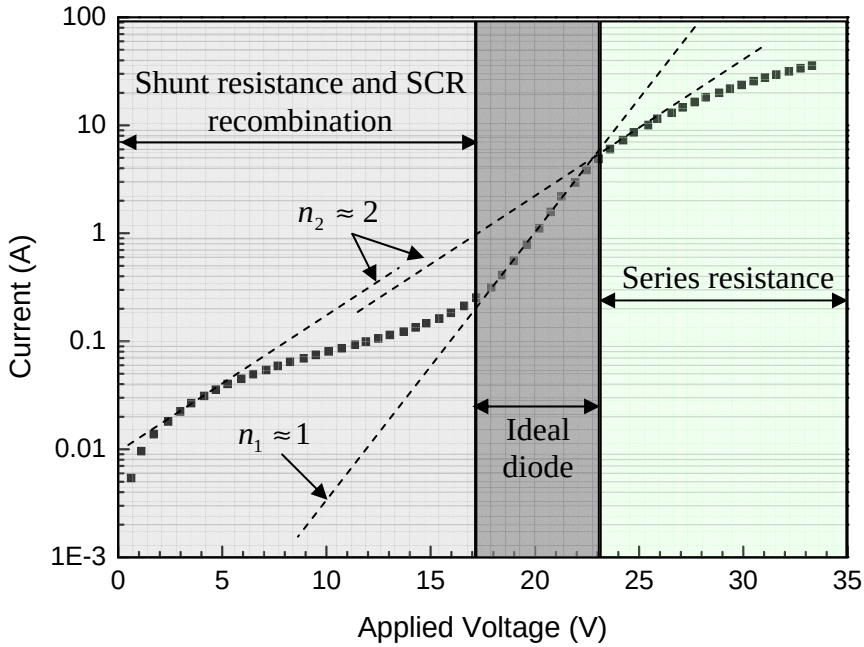

Figure 3.5: *Dark I-V characteristic of a typical solar module.*

3.5 Current-Voltage characteristics of a solar cell under illumination.

When a solar cell is illuminated and connected to a load, the electrons and holes acquire sufficient energy to move towards the surfaces of the *p-n* junction, as illustrated in figure 3.6. These current carriers contribute to the net current that circulates through the load from the *p*-side to the *n*-side. Also shown in the figure are the two opposing currents, photogenerated current, I_L, which is due to the carrier generation, and dark current, I_D, which is due to recombination of carriers and which is very much dependent on an applied voltage. Not all generated electron-hole pairs are separated by the built-in electric field, some of the separated free carriers recombine resulting in the recombination or dark current. The photogenerated current is therefore reduced by the dark current. Using the representation in figure 3.6, the current, *I*, through the external circuit can be derived from Kirchoff's current law:

$$I = I_L - I_D \tag{3.15}$$

where $I_D =$ dark current.

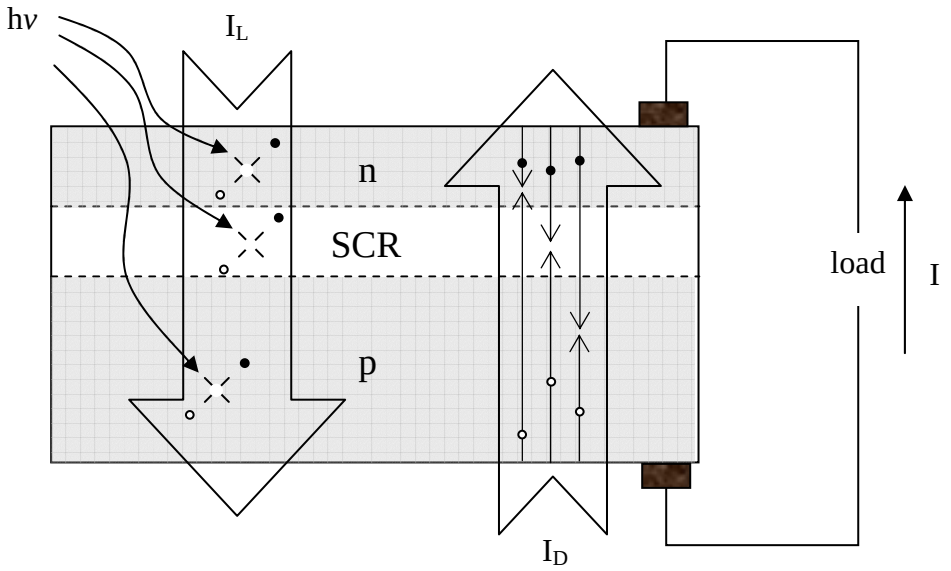

Figure 3.6: *Internal current in a solar cell when illuminated [Lorenzo, 1994].*

For simplicity, the one-diode model of an ideal solar cell is considered. Figure 3.7 represents the equivalent circuit of an ideal *p-n* junction solar cell. It consists of a diode and a current source in parallel to one another. The dark current and current source represents dark and photogenerated currents respectively. The dark current, I_D, is given by equation 3.8 and substituting this into equation 3.15 gives the current I:

$$I = I_L - I_0\left[\exp\left(\frac{qV}{nkT}\right) - 1\right] \tag{3.16}$$

where $I_0 =$ ideal saturation current.

Equation 3.16 is known as the fundamental characteristic equation of an ideal solar cell as represented in figure 3.7.

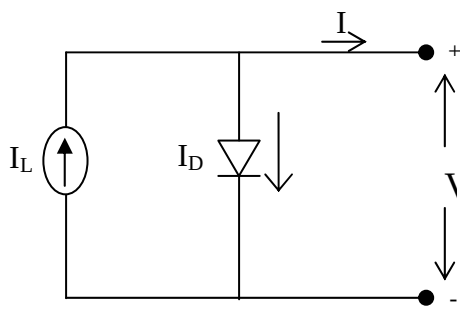

Figure 3.7: *Equivalent circuit of an ideal p-n junction solar cell [Lasnier, 1990]*

For a real solar cell, the total current in an external circuit is influenced by other factors, including series and shunt resistance. From equations 3.14 and 3.16, the total current I is given by:

$$I = I_L - I_{01}\left[\exp\left(\frac{q(V + IR_s)}{kT}\right) - 1\right] - I_{02}\left[\exp\left(\frac{q(V + IR_s)}{nkT}\right) - 1\right] - \frac{(V + IR_s)}{R_{sh}} \tag{3.17}$$

Equation 3.17 is known as the two-diode fundamental equation used to characterize solar cells. Figure 3.8 illustrates the equivalent circuit of a solar cell described by equation 3.17.

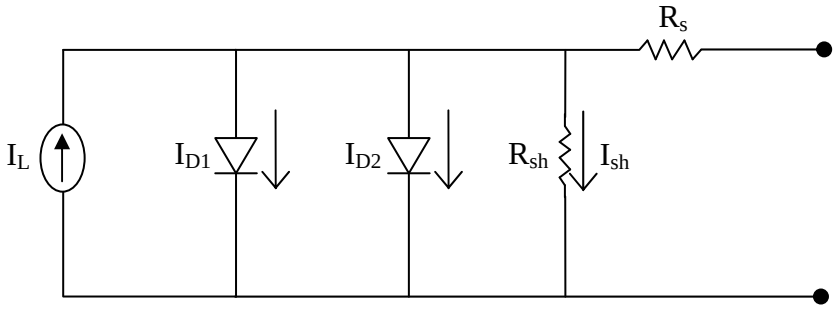

Figure 3.8: *Two-diode equivalent circuit of an illuminated solar cell.*

The I-V characteristic curve represented by equation 3.17 is shown in figure 3.9 for an EFG-Si solar cell. The performance parameters, short circuit current I_{sc}, open circuit voltage V_{0c} and the voltage, V_{mp} and current I_{mp} at maximum output power, and the maximum output power $P_{\max}$ are indicated. Also shown in the figure are the regions influenced by the parasitic series and shunt resistances, R_s and R_{sh}. Device parameter values that were determined from dark I-V measurements, for the solar cell for which the I-V curve is shown in figure 3.9, are listed in Table 3.1.

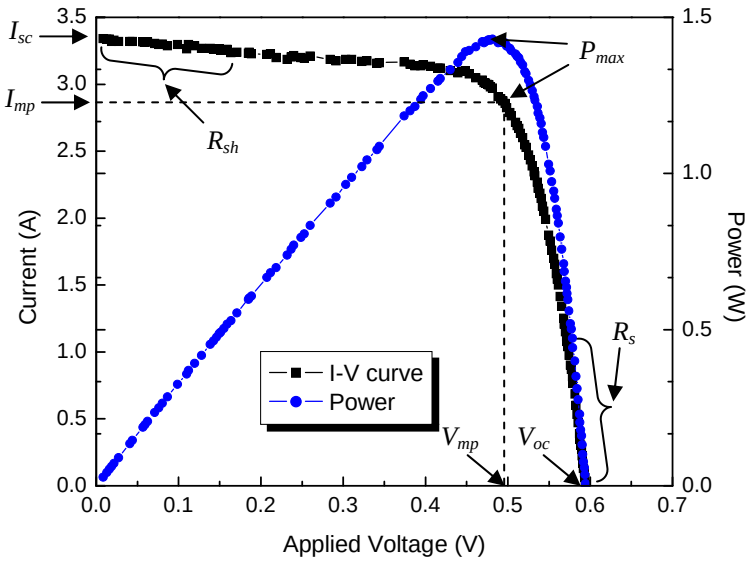

Figure 3.9: *A simulated I-V characteristic of a solar cell and its power curve.*

Table 3.1: *Parameters of the solar cell's I-V characteristics.*

I_{01}	$1.54\times10^{-4}\,A$
I_{02}	$2.0\times10^{-5}\,A$
R_{sh}	$2.4\times10^{1}\ \Omega$
R_s	$1.07\times10^{-2}\ \Omega$
n	2.26

Equation 3.17 can be written as [Luque, 2003]:

$$I = I_L - I_0\left[\exp\left(\frac{q(V+IR_s)}{nkT}\right)-1\right]-\frac{(V+IR_s)}{R_{sh}} \tag{3.18}$$

with: $n =$ ideality factor ($n \approx 1$ representing ideal case and $n > 1$ representing non-ideal case)

Often R_s is neglected and R_{sh} is taken to be infinite. Therefore, if a solar cell is short circuited, a short circuit current I_{sc} occurs which is approximately equivalent to the photogenerated current I_L. At this stage the terminal voltage is zero. If no load is connected, *I=0*, and the open circuit voltage V_{oc}, can be measured at the terminals. Thus, when *I=0* equation 3.18 yields V_{oc} as:

$$V_{oc} = \frac{nkT}{q}\left[\ln\left(I_{sc}-\frac{V_{oc}}{R_{sh}}+1\right)-\ln I_0\right] \tag{3.19}$$

The assumption that $R_{sh} = \infty$ implies that $R_{sh} >> \frac{V_{oc}}{I_{sc}}$ and $\left(I_{sc}-\frac{V_{oc}}{R_{sh}}\right) >> 1$, therefore equation 3.19 becomes:

$$V_{oc} = \frac{nkT}{q}\left[\ln I_{sc} - \ln I_0\right] \tag{3.20}$$

Equation 3.18 can be used to determine n and I_0 from the gradient and y-intercept of the plot of V_{oc} versus $\ln I_{sc}$ straight line graph [Meyer, 2002].

The electrical output power at any given I-V point is given by Joule's law as $P = IV$, as depicted in figure 3.9. At the voltage extremes, V_{oc} and I_{sc}, no power is generated. An irradiated cell provides power output for a voltage region between $0V$ and V_{oc}. The specific point of operation where the output power is at its maximum is called maximum power, $P_{\max}$, which corresponds to voltage V_{mp}, and current I_{mp}. $P_{\max}$ can then be determined using [Sze, 1981]:

$$P_{\max} = I_{mp} \times V_{mp} \approx I_L \left[V_{oc} - \frac{nkT}{q} \ln\left(\frac{qV_{mp}}{nkT} + 1 \right) - \frac{nkT}{q} \right] \qquad (3.21)$$

The efficiency η, of a solar cell can be calculated from $P_{\max}$, the area A of the cell, and the irradiance E, as follows:

$$\eta = \frac{P_{\max}}{E \times A} \qquad (3.22)$$

It is evident from equation 3.22 that efficiency of a solar cell depends on the maximum output power of solar cell. PV cells or modules are rated by their $P_{\max}$ measured under standard test conditions (STC), which means an illumination of $1000 W/m^2$, 25 °C cell temperature at the test, and a spectrum equivalent to Air mass 1.5.

3.6 Effect of irradiance on the I-V curve

When the irradiance level increases, the number of generated electron-hole pairs separating and inducing the photogenerated current, increases. Figure 3.10 shows two I-V curves obtained at different irradiance levels, 614 W/m^2 and 1000 W/m^2. It can be

seen that, I_{sc} is higher at higher irradiance levels since the photogenerated current, I_L, depends on the irradiance level. Voltage also depends on the irradiance level, and the relationship between I_{sc} and irradiance, and V_{oc} and irradiance is given by [Lorenzo, 1994]:

$$I_{sc} = xI_{sc,1-sun} \tag{3.23}$$

and

$$V_{oc} = V_{oc,1-sun} + \delta \ln x \tag{3.24}$$

where *1-sun* represents an irradiance of 1000 W/m^2 of irradiance, x is the level of irradiance, and δ is a dimensionless coefficient that is solar cell technology specific.

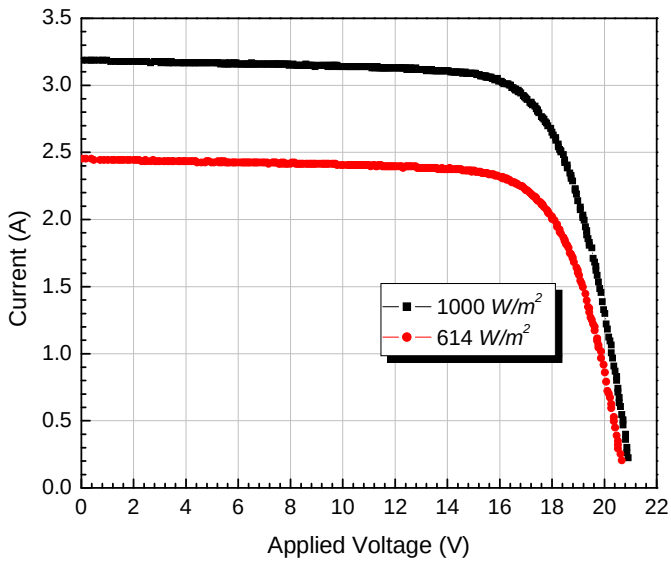

Figure 3.10: *I-V characteristics of a solar module at different irradiance levels.*

3.7 Effect of parasitic series and shunt resistance

The parasitic resistances, R_s and R_{sh}, are discussed in section 3.4.1. R_s and R_{sh} affect the efficiency of a solar cell and module. Their influence reduces the fill factor, which is the main quality consideration for a solar cell [Wenham et al, 1995]. As

shown in figure 3.9, that R_{sh} affects the I-V curve at higher current levels, and R_s affects the I-V curve at higher voltage levels. The effect of R_s and R_{sh} on solar cells and modules is further confirmed by dark I-V measurements (see Chapter 5). From equation 3.17, R_s and R_{sh} can be described as the slopes of the I-V curve [Schroder, 1998]:

$$R_s = -\frac{dV}{dI} \text{ at } I = 0 \tag{3.25}$$

and

$$R_{sh} = -\frac{dV}{dI} \text{ at } V = 0 \tag{3.26}$$

Two I-V characteristics of a solar cell measured at two different irradiance levels and constant temperature can be used to determine R_s. The slope of a line draw through points corresponding to a fixed current below the respective I_{sc} on each curve, gives [van Dyk et al., 2004]:

$$R_s = \frac{\Delta V}{\Delta I} \tag{3.27}$$

A high series resistance increases voltage drop and hence the fill factor of a solar cell is reduced. Solar cells having a low shunt resistance, cause a reduction in module efficiency [Meyer, 1999].

In addition, from equation 3.19, V_{oc} is reduced by R_{sh}. Equation 3.19 can be rearranged and written as:

$$I_{sc} - I_0\left[\exp\left(\frac{qV_{oc}}{nkT}\right) - 1\right] = \frac{V_{oc}}{R_{sh}} \tag{3.28}$$

At lower irradiance levels, the second term approaches zero and equation 3.28 then becomes [Schroder, 1998]:

$$I_{sc} \approx \frac{V_{oc}}{R_{sh}} \tag{3.29}$$

From equation 3.29, $\frac{1}{R_{sh}}$ is the slope of I_{sc} versus V_{oc} yielding R_{sh}.

3.8 SUMMARY

The main objective of this chapter was to understand the physics of *p-n* junction solar cells. The basis of solar cell operation is the *p-n* junction formed between *p*-doped and *n*-doped semiconductor materials with the same lattice structure. With the application of forward bias, current flows through the diode, while with the application of reverse bias, current is blocked. The relationship between the diode current and the applied voltage was discussed.

Performance parameters of solar cells and PV modules such as I_{sc}, V_{0c}, $P_{\max}$, η and FF used to describe I-V characteristic curve, were discussed. Parasitic series- and shunt resistances which affect the FF of the solar module were discussed. The effect of irradiance on PV modules was also discussed.

3.9 REFERENCES

Goetzberger A., Knobloch J. and Voss B. (1994), *Crystalline Silicon Solar Cells*, John Wiley and Sons Ltd, pp 50-64.

Lasnier F. and Ang T.G. (1990), *Photovoltaic Engineering Handbook*, Adam Hilger, pp 72.

Lorenzo E. (1994), Translated by Philip Davies, *Solar Electricity: Engineering of Photovoltaic Systems*, PROGENSA, pp 84.

Luque A. and Hegedus S. (2003), *Handbook of Photovoltaic Science and Engineering*, John Wiley and Sons, pp 102.

Mazer J.A. (1997), *Solar Cells: An introduction to crystalline Photovoltaic Technology*, Kluwer Academic Publications, pp 89.

Meyer E.L. (1999), *Investigation of Properties and Energy Rating of Photovoltaic Modules*, University of Port Elizabeth, MSc-dissertation, pp 17-23.

Meyer E.L. and van Dyk E.E. (2002), "Extraction of I_0 and n from I_{sc} and V_{oc} measurements," *Journal of Applied Physics*, pp 71.

Sapoval B. and Hermann C. (1995), Translated by A.R. King, *Physics of Semiconductors*, Springer-Verlag, pp 207.

Schroder D.K. (1998), *Semiconductor Material and Device Characterization*, John Wiley and Sons, pp 209-214.

Sze S.M. (1981), *Physics of Semiconductor Devices*, John Wiley and Sons, pp 793-796.

Sze S.M. (1985), *Physics of Semiconductor Devices*, John Wiley and Sons, pp 88.

van Dyk E.E. and Meyer E.L. (2004), "Analysis of the effect of parasitic resistances on the performance of Photovoltaic Modules," *Renewable Energy*, **29**.

Wenham S.R., Green M.A., Watt M.E. (1995), *Applied Photovoltaics*, Centre for Photovoltaic Devices and Systems, pp 42.

CHAPTER 4

EVOLUTION OF COPPER INDIUM DISELENIDE ($CuInSe_2$) BASED SOLAR CELLS AND MODULES.

4.1 INTRODUCTION

Thin film solar cells are a hundred times thinner and potentially lighter than conventional crystalline silicon solar cells. Semiconductor layers used in thin film solar cells mostly are two to three microns thick. The advantage of thin film solar cells is their ability to produce low cost electrical power without harmful emissions. Traditional crystalline silicon solar cells require relatively large amounts of semiconducting material, making them expensive to manufacture and increasing their cost in the market, while thin film solar cells require less semiconductor material and hence they can be made for less money.

The most common materials used in thin film solar cell technologies, are amorphous silicon (a-Si), or the polycrystalline semiconductor materials: cadmium telluride (CdTe) and copper indium diselenide (CIS) and copper indium gallium diselenide (CIGS). The a-Si solar cells have been available commercially for many years and the technology is employed in solar-powered watches and calculators. In both a-Si and CdTe solar cells, the cell structure in its simplest form has a single sequence of *p-i-n* layers [Zweibel, 1995]. CIS-based solar cells, however, have as their basis the *p-n* heterojunction, which is formed between the *n*-type zinc oxide (ZnO) and the *p*-type CIS semiconductor materials. The advantage of the CIS solar modules over a-Si and CdTe solar modules is their stability when deployed outdoors for the period of nearly ten years at the National Renewable Energy Laboratory (NREL) [Zweibel, 1990; Karg, 1993].

The characterization of the chalcopyrite CIS structure was first reported by Hahn in early 1953 [Hahn, 1953]. During the 1970s, scientists at Bell Laboratories explored the technology by preparing the first CIS-based solar cell. They made it by

effectively evaporating *n*-type CdS onto single-crystal *p*-type CIS [Wanger, 1974]. These crystalline CIS solar cells were deployed outdoors in New Jersey and their efficiencies per cell were 12% [Shay, 1975]. Because much focus has since been shifted to the growing thin film technologies researchers have lost interest in single-crystal CIS solar cell technology. The first thin film CIS-based solar cell based was manufactured using film deposition [Kazmerski, 1976]. Boeing then fabricated CIS solar cells by evaporating CIS elemental sources onto a ceramic substrate coated with molybdenum (Mo) electrodes, and then completed the device by evaporating an indium doped CdS layer onto the CIS/Mo structure. The efficiency, which was the first for these CIS solar cell type, was found to be 9.4% [Mickelsen, 1981].

The technology was adopted by many research groups around the world, resulting in the improved efficiency of the CIS based solar cells. One of the major advances made was to alloy CIS with gallium (Ga) to form CIGS cells. This allows the band-gap profile to be optimized to increase the photon absorption and carrier diffusion rate, and with the incorporation of Ga, the CIS with a bandgap of 1.02 eV bandgap was increased to 1.1 eV -1.2 eV and the absorber layer became CIGS.

In this chapter, the structure of the CIS solar cell is discussed in terms of the formation and operation of a *p-n* heterojunction. The fabrication processes and characteristics of the CIS solar cells and modules are then discussed. Finally, typical current-voltage characteristics of CIS solar modules, obtained under both illumination and dark conditions, are presented.

4.2 STRUCTURE OF THE $CuInSe_2$ SOLAR CELLS.

4.2.1 Device materials

The dominant structure in a CIS solar cell is the CIS absorber layer which is made out of the CIS semiconductor material. CIS is a compound made of elements of different groups in the Periodic Table; Cu from Group I, In from Group III and Se from Group VI. CIS semiconductor coatings are deposited by combining sputtered fluxes of Cu

and In with an evaporated flux of Se. Equation 4.1 shows the chemical formation of the CIS compound semiconductor:

$$Cu_2Se + 2InSe + Se \rightarrow 2CuInSe_2 \tag{4.1}$$

With its diamond crystal structure, the CIS compound is an example of chalcopyrite semiconductors. The unit cell crystal structure of the chalcopyrite CIS compound is illustrated in figure 4.1, and the corresponding parameters are listed in table 4.1.

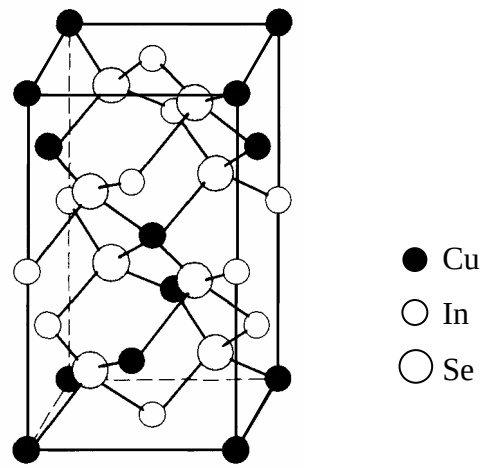

Figure 4.1: *The unit cell of chalcopyrite $CuInSe_2$ structure.*

Table 4.1: Properties of CIS [Neumann., 1986].

Lattice parameters	$a_0 = 5.78\ Å$ $c = 11.62\ Å$
Energy gap (E_g)	$1.02\ eV$
Effective mass (m_e)	electrons ≈ 0.09 holes ≈ 0.71

CIS is a unique material in that it is a semiconducting material with one of the highest bandedge absorption. This implies that even in its polycrystalline form, non-radiative recombination centers can be strongly suppressed, leading to its ability to be used in photovoltaic applications.

One of the main characteristics of CIS is its ability to absorb a large amount of electromagnetic radiation. This is due to its relatively high absorption coefficient.

4.2.2 Optical and electrical properties of $CuInSe_2$ materials.

CIS is a direct bandgap semiconductor, that is, photon absorption can occur as discussed in Chapter 2. Since the valence and conduction bands are nearly parabolic in real space, the absorption coefficient, α, as a function of photon energy, $h\nu$, near the band-gap follows a dependence of the form [Neumann, 1986]:

$$\alpha = \frac{A}{h\nu}\left(h\nu - E_g\right)^2 \tag{4.2}$$

where E_g is the bandgap energy and A is the proportionality constant that depends on the density of states associated with the absorption of photons [Luque, 2003]. It has been reported that CIS has an absorption coefficient of greater than $10^5 cm^{-1}$ [Kazmerski, 1983].

CIS can either be doped as *n*-type or *p*-type, depending on the doping impurities. Cu-rich CIS films are regarded as *p-type* materials, while with excess In, CIS can either be *n*- or *p*-type [Noufi, 1984].

4.2.3 The p-n heterojunction formed by $CuInSe_2$ and ZnO materials.

When two crystal semiconductors with different energy bandgaps are combined, a heterojunction is formed. An example of a heterojunction device is a CIS solar cell, where the junction is formed by contacting ZnO and CIS. Thus, when the *n*-type ZnO with an energy gap of $3.35eV$ is combined with the *p*-type CIS with an energy gap of $1.02eV$ (listed in table 4.1), the *p-n* heterojunction is formed. The first ideal heterojunction energy band diagram model was proposed in the 19th century. Figure 4.2 illustrates ideal energy band diagrams for *p*-CIS and *n*-ZnO [Tyagi, 1991].

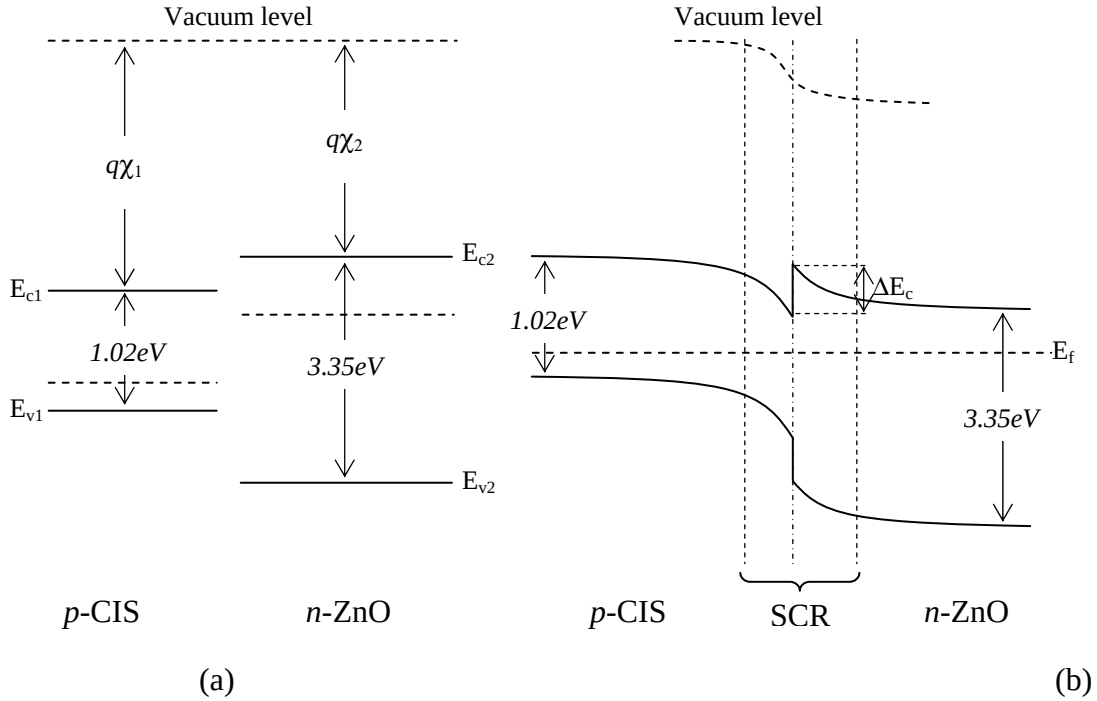

Figure 4.2: *Ideal energy band diagrams; a) Neutral p-CIS and n-ZnO bands and b) The p-n heterojunction at equilibrium.*

Figure 4.2a shows neutral isolated energy-band diagrams for *p*-CIS and *n*-ZnO materials. Because of the different energy bandgaps, the two semiconductors have different electron affinities, $q\chi$. The electron affinity is defined as the energy required to remove an electron from the bottom of the conduction band, E_c, to the vacuum potential level.

The formation of an ideal *p-n* heterojunction between the two semiconductors is indicated in figure 4.2b. The difference in electron affinity implies that semiconductors with lower energy band gaps have higher electron affinities [Sze, 1981]. As in homojunction devices carrier transport is influenced, during the contact of *p*-CIS and *n*-ZnO phases.

That is, when *p*-CIS and *n*-ZnO regions are separated, immobile donor ions which are positively charged in *n*-region, are balanced by mobile electrons, while in the *p*-region the negatively charged immobile acceptor ions are balanced by mobile holes. When the two materials connect, however, electrons diffuse from the *n*-ZnO side to the *p*-

CIS, while holes diffuse in the opposite direction to the electron movement. The electron-hole flow continues, building the space charge region (SCR) until the Fermi energy is the same everywhere in the material. Similar to a *p-n* homojunction, the SCR created consist of ionized donors on the *n*-ZnO side and ionized acceptors on the *p*-CIS side.

Since E_{c1} and E_{c2} are parallel to the vacuum potential level, as indicated in figure 4.2b, and because the Fermi level is constant, there is an abrupt discontinuity, ΔE_c, at the interface. It can be seen from figure 4.2b that ΔE_c is the difference between the electron affinities of the two materials [Tyagi, 1991; 292]:

$$\Delta E_c = q(\chi_1 - \chi_2) \tag{4.3}$$

Equation 4.3 describes the discontinuity of the conduction band within the SCR, and is due to the difference in energy of the electrons.

In figure 4.2 the ideal case was considered, which neglected the generation and recombination of carriers at the interface of the two dissimilar materials. In reality or the non-ideal situation, however, the matching of two lattice types with different atoms on both sides may introduce some interface states in the SCR [Streetman, 1990]. These states may cause shunting paths within the *p-n* heterojunction, and, as has been discussed in Chapter 2, shunts lower the efficiency of a practical *p-n* heterojunction device.

4.2.4 Current in a p-n heterojunction.

From figure 4.2, electrons in the *n*-ZnO side (wide bandgap) need to overcome a lower barrier than the holes in the *p*-CIS side (narrow bandgap). This means that the wide bandgap *n*-ZnO injects more carriers across the junction than the narrow bandgap *p*-CIS semiconductor. The movement of carriers in a non-ideal *p-n*

heterojunction results in a flow of current and from equation 3.13, the current is given as:

$$I = I_0\left[\exp\left(\frac{q(V + IR_s)}{nkT}\right) - 1\right] + \frac{(V + IR_s)}{R_{sh}} \tag{4.4}$$

where the symbols have their usual meaning.

Equation 4.4 describes the non-ideal current-voltage characteristic of a CIS/ZnO *p-n* heterojunction under dark conditions. It has been discussed in Chapter 3 that *p-n* junction devices behave like diodes under dark conditions. CIS solar cells, therefore, can operate like diodes under dark conditions and equation 4.4 can be used to determine its current-voltage characteristic.

When a CIS/ZnO *p-n* heterojunction device is illuminated and connected to an external load, the photogenerated current, I_L, is opposed by the dark current, I_D (equation 4.4) and shunt current, I_{sh}. Therefore the current, *I*, through the load is given as:

$$I = I_L - I_D - I_{sh} \tag{4.5}$$

Substituting equations 3.16 and 4.4 into equation 4.5 yields:

$$I = I_L - I_0\left[\exp\left(\frac{q(V + IR_s)}{nkT}\right) - 1\right] + \frac{(V + IR_s)}{R_{sh}} \tag{4.6}$$

4.2.5 Fabrication of $CuInSe_2$ solar cell.

There are several techniques used to fabricate and produce CIS thin films and CIS solar cells can be fabricated by depositing a Cu-In(Ga)-Se precursor layer on Molybdenum (Mo) coated soda lime glass, sintering the particulate layer to form a dense CIS film, coating the CIS with CdS and ZnO, and depositing a metal grid

[Eberspacher et al., 2000]. Figure 4.3 shows the schematic representation of a typical CIS based solar cell. The top layer *n*+-ZnO acts as a window layer, admitting photons of less than its energy bandgap. The thin *i*-ZnO layer is the intrinsic semiconductor layer that acts as a passivator between the *n*+-ZnO and CdS layers. The CdS acts as a buffer layer which controls the interface states within the CIS/ZnO *p*-*n* heterojunction. The *p*-CIS type layer act as the absorber layer. The main role of the Mo is to act as the other bottom electrical contact, to capture the charge carriers.

The *n*+-ZnO layer is selected as the window layer because of its wide bandgap that is transparent to incident light. This layer allows almost all incident light to reach the absorber layer, which is the *p*-CIS material with a low bandgap that readily absorbs photons. The photons then generate electrons and holes very near the junction. The window layer also reduces series resistance in the cell, and its thickness does not reduce the transmittance of light. As a result, photon generated electrons can easily flow laterally in the window layer to reach the electrical contacts.

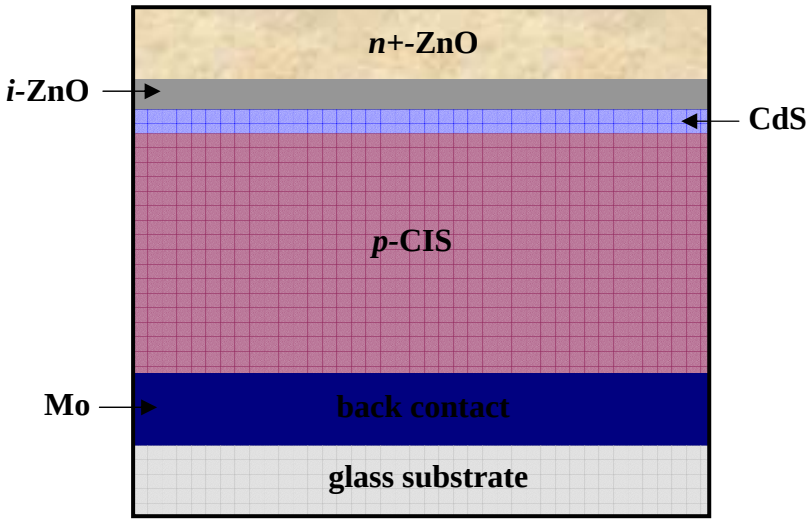

Figure 4.3: *Schematic indication of a $CuInSe_2$ solar cell [Carlson, 1996].*

Common methods for fabricating CIS thin films include deposition of Cu-In by thermal co-evaporation from elemental sources [Mattox, 1998]. Another common method in fabricating CIS thin film is the two-step deposition process. In this process

the CIS absorber layer can be prepared by depositing Cu-In metallic alloys, followed by selenization using H_2Se gas [Alberts, 2000].

4.3 PERFORMANCE OF $CuInSe_2$ SOLAR CELLS AND MODULES.

To illustrate the performance of $CuInSe_2$ based solar cells and modules, a CIS module from Siemens Solar products (ST) was used in this study. Figure 4.4 shows the current-voltage characteristics of the ST10 CIS module under dark conditions and illumination.

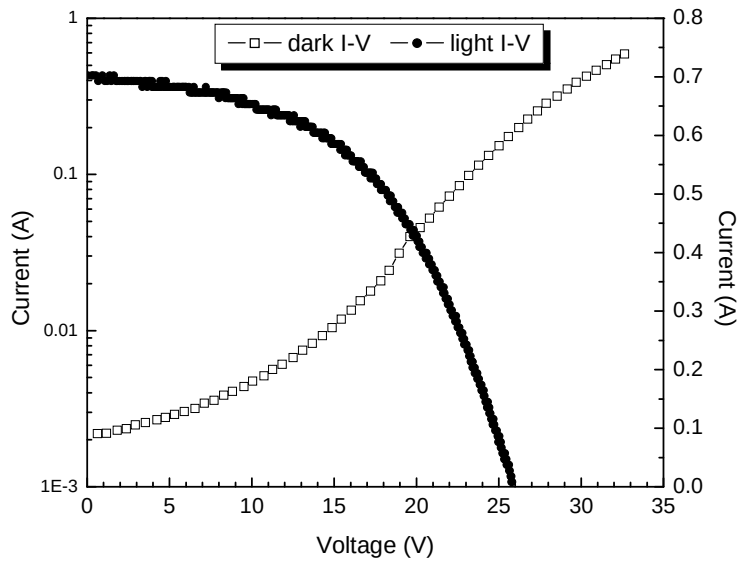

Figure 4.4: *I-V characteristics of the CIS module measured under illumination and dark conditions.*

Parameters obtained from the light and dark I-V measurements are listed in tables 4.2 and 4.3, respectively. For the light I-V characteristic, measurements were performed using the SPIRE SUN-240 solar simulator at Standard Test Conditions (STC), where the irradiance is $1000 W/m^2$, cell temperature is 25°C and global spectrum is AM 1.5. The dark I-V measurements were performed using the method discussed in Chapter 5.

Table 4.2: Performance parameters of the CIS module using light I-V measurements.

P_{max} (W)		I_{sc} (A)		V_{oc} (V)		FF	η
RATED	STC	RATED	STC	RATED	STC	STC	STC
10.0	9.31	0.61	0.70	25.0	25.97	0.51	7.88

Table 4.3: Performance parameters of the CIS module using dark I-V measurements.

I_{01} (A)	I_{02} (A)	R_{sh} (Ω)	R_s (Ω)	n (/ cell)
1.725E-9	2.162E-6	2250	1.26	1.42

4.4 SUMMARY

The objectives of this chapter were to obtain a fundamental understanding of the chalcopyrite $CuInSe_2$ semiconductor and its ability to be employed in photovoltaic applications. The formation of *p-n* heterojunctions between *p*-CIS and *n*-ZnO semiconductors having different bandgaps but similar lattice structures, was discussed. The I-V characteristics of a *p-n* heterojunction when illuminated and under the dark conditions were described. The description of the materials used for producing CIS solar cells was presented. A Brief summary of some of the common methods used to prepare CIS thin film solar cells was presented. The CIS solar module manufactured by Siemens was used to illustrate the CIS solar device performance, and its performance parameters obtained using I-V characteristics were presented under light and dark conditions. Chapters 5 will present the dark I-V characteristics of solar cells and PV modules, while Chapter 6 will discuss the light I-V characteristics.

4.5 REFERENCES

Alberts V., Klenk M. and Bucher E. (2000), "Material losses and compositional changes in two-step processed $CuInSe_2$ thin films," *Japan Journal of Physics*, **39**; pp 5776-5780.

Carlson D.E., Arya R.R., Bennett M., Chen L.F., Jansen K., Li Y.M. and Newton J. (1996), "Commercialization of multijunction amorphous silicon modules," *Proceedings of the 25th IEEE Photovoltaic Specialists Conference*; pp 1023-1028.

Hahn H. and Anorg Z.(1953), *Allg. Chem.* **271**, pp 153-170.

Karg F., Probst V., Harms H., Rimmash J., Rieidi W., Mitwalski A. and Kiedl A. (1993), *Proceedings 23rd IEEE Photovoltaic Specialists Conference*, Louisville, pp 441.

Kazmerski L. (1983), *J. Vac. Sci. Technol.*, ***1***

Kazmerski L., White F. Morgan G. (1976), *Applied Physics Letter*, **29**, pp 268-269.

Luque A. and Hegedus, S. (2003), *Handbook of Photovoltaic Science and Engineering*, John Wiley and Sons, pp 574.

Mattox R., *"Handbook of Physical Vapor Deposition (PVD) Processing."* Noyes Pupl., Park Ridge, NJ.

Mickelsen R. and Chen W. (1981), *Proceedings 15th IEEE Photovoltaic Specialist Conference*, pp 800-804.

Neumann H. (1986), *Solar Cells*, **16**, pp 317-333.

Noufi R., Axton R. and Herrington C. (1984), *Applied Physics Letter*, **45**

Shay J., Wanger S. and Kasper H. (1975), *Applied Physics Letter*, **27**, pp 89-90.

Streetman B.G. (1990), *"Solid State Electronic Devices,"* Prentice-Hall, pp 189.

Sze S.M. (1981), *Physics of Semiconductor Devices*, John Wiley and Sons.

Tyagi M.S. (1991), *"Introduction to semiconductor materials and devices,"* John Wiley and Sons, pp 291.

Wanger S., Shay J., Migliorato P. and Kasper H. (1974), *Applied Physics Letter*, **25**, pp 434.

Zweibel K. (1990), *Harnessing Solar Power*, Plenum Press.

CHAPTER 5

DARK CURRENT-VOLTAGE CHARACTERISTICS OF SOLAR CELLS AND PHOTOVOLTAIC MODULES.

5.1 INTRODUCTION

The current-voltage (I-V) characterization under illumination is described in Chapter 6, while this chapter describes the I-V characterization under dark conditions. Dark I-V measurements are commonly used to analyze the electrical characteristics of solar cells and modules, providing an effective way to determine fundamental device parameters without the need for a solar simulator. The dark I-V measurement procedure does not provide information regarding short-circuit current or open-circuit voltage, but is more sensitive than light I-V measurements in determining the other electrical parameters, such as series resistance, shunt resistance, and diode parameters (ideality factor and reverse saturation current).

Various methods and procedures for finding parasitic, series and shunt resistances, and diode parameters, have been described before [Chegaar, 2004]. Extraction of junction parameters with special emphasis on low series resistance under no illumination [Kaminski, 1999], is an example. Other techniques for determining electrical parameters, involve the use of the I-V curve taken under both illumination and dark conditions [Van Kerschaver, 1997].

This chapter starts by describing the methods used to perform dark I-V characteristics of solar cells and photovoltaic (PV) modules. These methods are then discussed in terms of the instruments and the experimental procedures used. PV modules manufactured using various types of semiconductor materials were used in this study. The method used to extract device parameters from the dark I-V profile is presented. Results obtained are presented and analysed. A summary and concluding remarks are presented at the end.

5.2 METHODOLOGY

The objective of this study was to analyze electrical characteristics of photovoltaic devices by evaluating their I-V characteristics without incident light. It has been mentioned in Chapter 3 that reverse biasing is not important in solar cell technology. In this study we therefore present dark I-V characteristics of solar cells and PV modules with reference to a forward biased *p-n* junction device.

The first phase in this process was to perform I-V measurements in a system that allowed current measurements between 10^{-2} A and 10^{-5} A. This system is referred to as a low current measurement system. The significance of evaluating solar cells and PV modules at low currents is to increase the sensitivity so that shunt resistances of solar cells and PV modules can be determined.

Solar panels have different power ratings and hence different potentials and currents. The low current measurement system used initially had a fairly low current limit. Because of this, the complete dark I-V profile could not be obtained for all PV devices, particularly modules. The second phase of this work was thus to expand measurements to higher currents by designing a system that would not limit current measurements, and thus accommodate PV modules. This system is referred to as the high-current measurement system, and was built with the current range extended to 20 A. The stability of the current measurements using this system is such that the low current limit is of the order of 10^{-3} A, yielding a range that enables one to obtain an improved dark I-V profile with reference to the dark I-V profile described by King (1997).

During dark I-V measurements, the photogenerated current is eliminated by placing the sample (solar cell or PV module) in a dark enclosure. The sample is forward biased to a preset voltage, and the resulting current is measured, obtaining the I-V relationship. The I-V data generated is analyzed and the necessary device parameters are determined. The device parameters are then used to discuss the performance of the solar cell and module.

5.3 LOW CURRENT MEASUREMENTS.

5.3.1 System description and experimental procedure

In order to perform dark I-V measurements, a dark I-V system which was built at the University of Port Elizabeth was used. The system consists mainly of a pA meter / dc voltage source, a sample holder, and a C-V / I-V mode selector. Figures 5.1 and 5.2 show photographs and schematic diagram illustrating the equipment used to perform C-V / I-V measurements. A computer controls the pA meter / dc voltage source. Only the C-V / I-V mode was operated manually. For this study, the I-V mode was selected to perform dark I-V measurements.

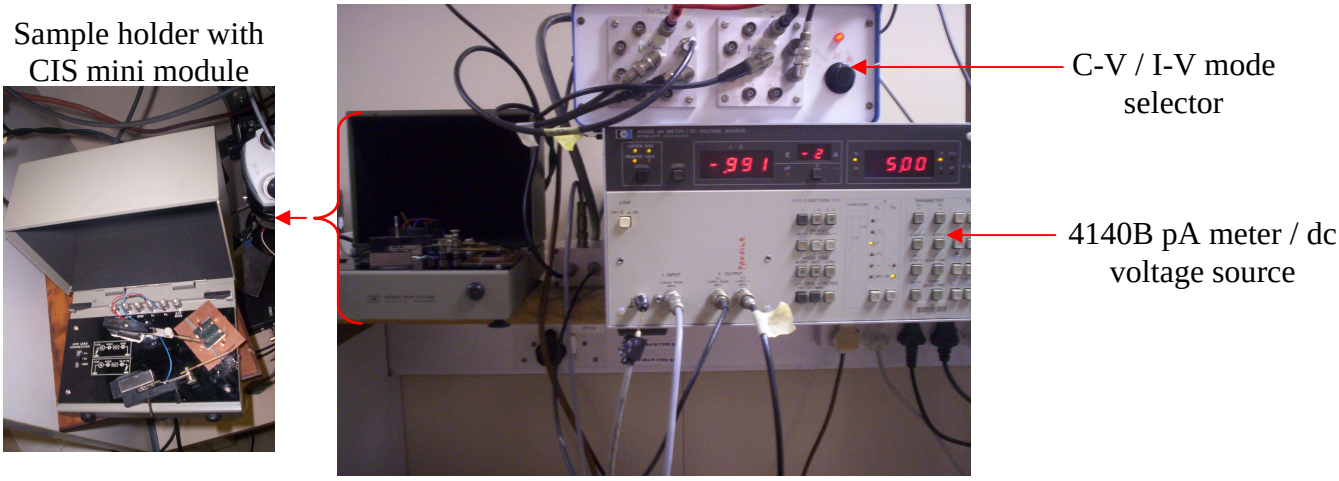

Figure 5.1: *Dark I-V system for low current measurements.*

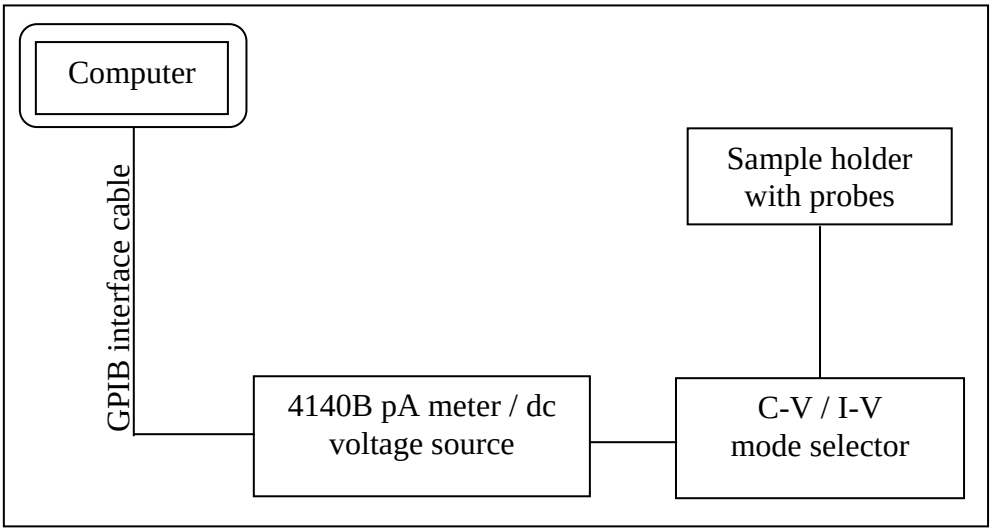

Figure 5.2: *Schematic diagram of the equipment shown in figure 5.1.*

5.3.1.1 The pA meter / dc voltage source.

The Hewlett Packard 4140B pA meter / dc voltage source unit was used to apply voltage across a solar cell or PV module, and measure the current. This instrument is an electrical characterization tool having features that make it ideal for I-V measurements, since it can make accurate I-V measurements automatically by simultaneously measuring the voltage and current. This is due to the picoammeter and two programmable voltage source units, one voltage source operates only as a constant voltage generator and the other supports the internal system. The main reason for using this instrument is its ability to perform I-V measurements accurately between 1.00×10^{-5} to $\pm1.99\times10^{-2}$ A. Measurement results are sent via a GPIB interface to a computer, allowing for data acquisition and remote control for further processing.

5.3.1.2 The sample holder.

A sample holder was used to make electrical contract to a solar cell or PV module. This sample holder has positive and negative probes mounted on the stage of a black box as shown in figure 5.1. The flexibility of these probes enables the operator to make physical contact to the sample that is being studied. During measurements the box is closed to obtain dark I-V conditions.

5.3.1.3 The C-V / I-V mode selector.

The C-V / I-V mode selector was used in this study to allow the connection between the pA meter / dc voltage source and the sample that is being studied. The I-V mode was selected for dark I-V measurements.

5.3.2 System software.

The system software was programmed using HPVEE. The software enables the communication between the instruments and a computer. This study used a program written by L. Wu specifically for performing dark I-V measurements [James, 2002].

The program uses calibration equations to obtain the dark I-V profile of the sample being examined.

5.3.3 Capturing I-V curves.

During the capturing of the I-V curve, the operator is required to manually input the step size and range of forward biased voltage. The pA meter / dc voltage source applies the voltage across the sample and measures the current through it, while the computer monitors and records the I-V data for further analysis.

5.4 HIGH CURRENT MEASUREMENTS

5.4.1 System description and experimental procedure.

A dark I-V system was built in order to facilitate high current measurements. The system setup is shown in figure 5.3. The system components listed in figure 5.3, are, a 60V, 30A power supply; a dual output programmable power supply; a multimeter; a voltage transducer circuit box; and an industrial computer. A schematic representation of the system is given in figure 5.4. The system components and operation are discussed below.

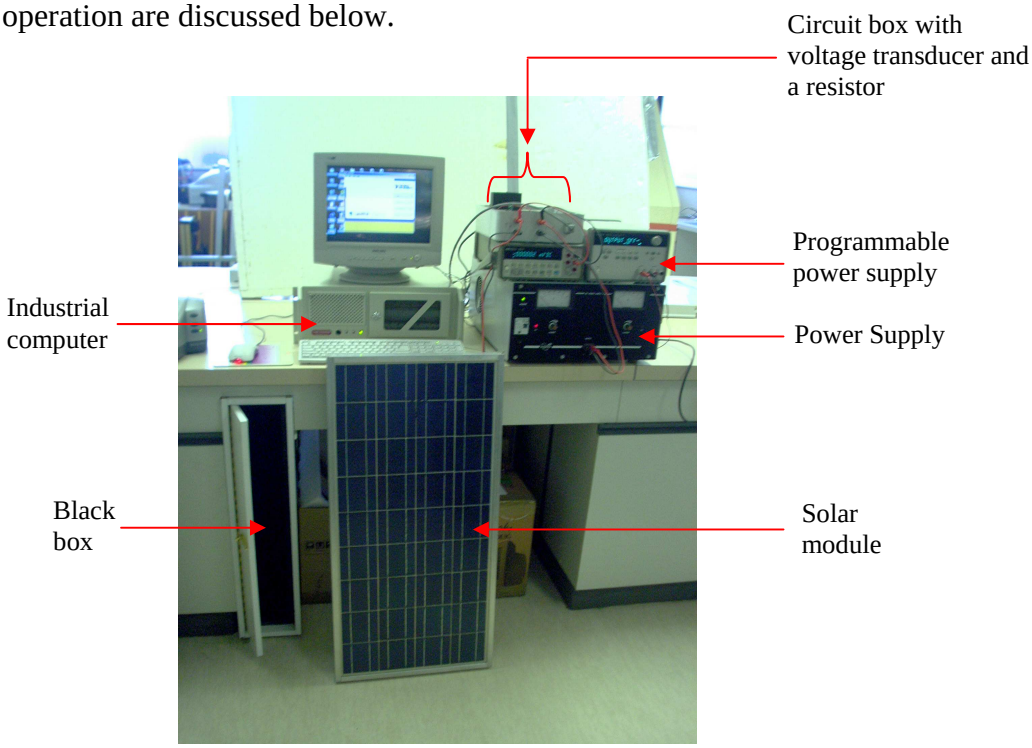

Figure 5.3: *Dark current-voltage measurement system unit.*

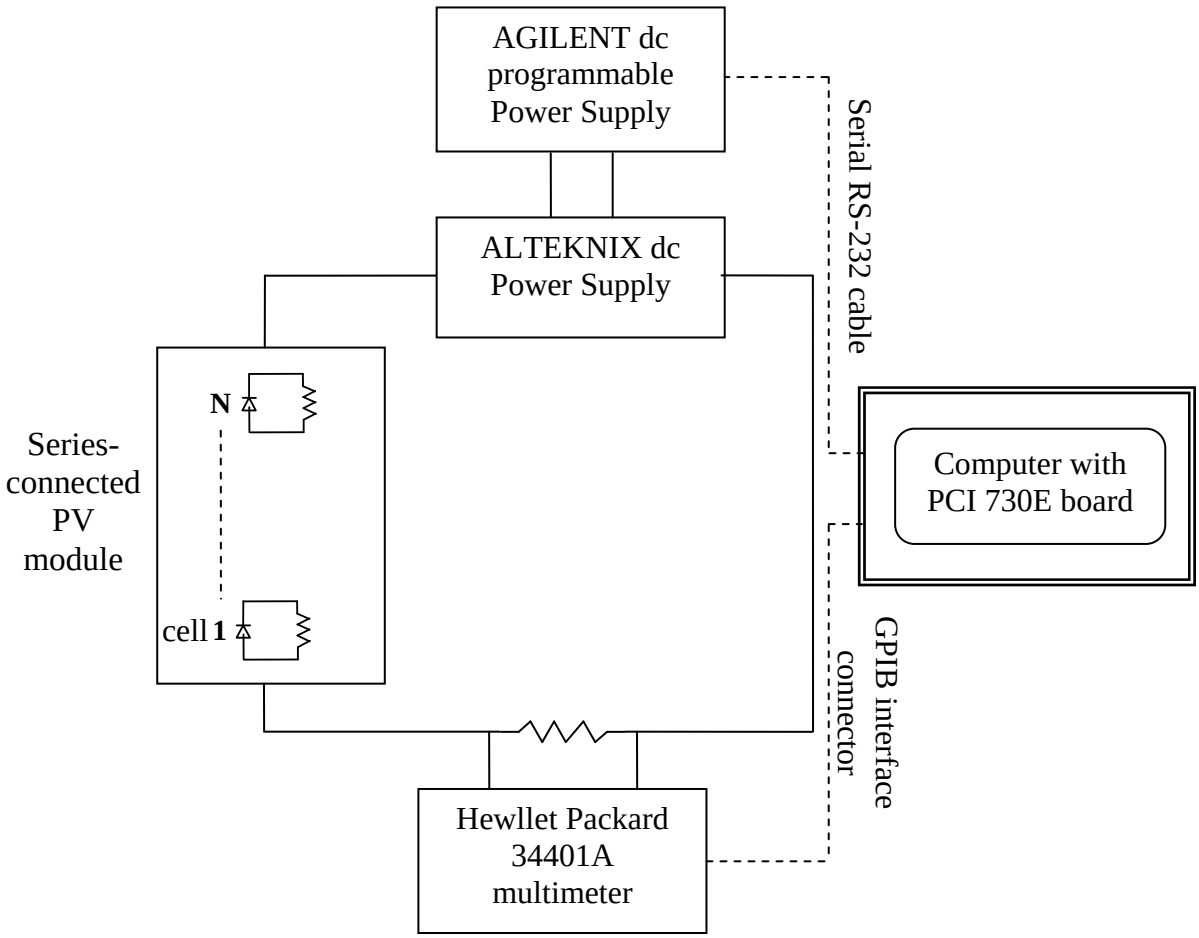

Figure 5.4: *Schematic diagram for dark I-V measurements system.*

5.4.1.1 ELTEKNIX 60/30 model power supply.

The ELTEKNIX 60/30 universal power supply (PSU) was used to apply forward-bias voltage across a PV module. The ELTEKNIX PSU consists of two analogue meters that are displayed on the front panel as voltage and current. With its output voltage range of 0 to 60V and current rating of 0 to 30A, the dark I-V measurement profiles of PV modules were obtained as described by King (1997). The PSU accepts an input range of 0-10 V dc, allowing automatic control by an isolated external source. In this study, the ELTEKNIX PSU was connected to the programmable power supply, for remotely controlling the voltage.

5.4.1.2 Agilent E3646A power supply.

The Agilent E3646A power supply (PSU) is a programmable power supply, and in this study it was used to remotely control the ELTEKNIX PSU. It allows the flexibility of selecting from dual output ranges displayed on its front panel, and the instrument is rated 8V at 3A or 20V at 1.5A. It also has the Standard Commands for Programmable Instrument Language Software that makes it easy to be programmed. For this study, the programming language, LabVIEW was used to control the Agilent PSU, which was connected to the computer via the RS-232 interface.

5.4.1.3 Agilent 34401A multimeter.

The Agilent 34401A digital multimeter was used to measure voltage drop across a wire which was incorporated in the system. It features test functions and built-in maths operations on the front panel. These features make it possible to manually adjust parameters such as setting an instrument address and selecting the appropriate interface. For this study the multimeter was set to accurately measure voltage. What makes this instrument valuable is its ability to measure voltage within 0.1 ± 1000 V dc range, and current in the range of 0.01 to 0.1 A. The accuracy for dc is 0.0015% and for ac 0.06%. This instrument was connected via a USB / GPIB interface bus to the industrial computer, and LabVIEW was used for interfacing.

5.4.1.4 Voltage transducer circuit box.

Another important feature in the high current measurement system is the circuit box which is referred to as the voltage transducer circuit box. It consists of an I-Q model voltage transducer and a 0.1Ω resistor wire, of which the latter was used with the multimeter to measure the current through the PV module being studied. The I-Q model voltage transducer was used for voltage measurements. This voltage transducer requires an input voltage of between $0-60$ V, and converts it to an output with a between $0-5$ V. The schematic representation of the voltage transducer is shown in Appendix A. This voltage transducer was connected between the module being studied and the industrial computer.

5.4.2 Data acquisition circuit.

The data acquisition circuit consists of a PCI-730E input/output board [Eagle Technology, 2003]. This board was used as an input board for the analogue signal to measure the transduced voltage. It offers 16-bit resolution with 25 pinouts for external connections. For analogue inputs, the board accepts input ranges of ± 2.5, V ± 5 V and ± 10 V. In this study, an input of ± 5 V was used, and the board was interfaced to a voltage transducer via a serial cable.

5.4.3 System software.

National Instrument's LabVIEW programming language was used as system software to obtain I-V data. LabVIEW has tools that provide support for data processing and acquisition [National Instrument]. It also has a variety of software drivers for remotely controlling instruments. The availability of software drivers for the instrumentation used in this study simplified the integration of the instruments into a system. LabVIEW offers software drivers for programmable power supplies, digital multimeters and the PCI-730E acquisition board.

5.4.4 System calibration.

This section describes calibration measurements of transduced voltage as a function of the 60/30 power supply voltage, and the current through a PV module that is being studied as a function of the voltage drop across a resistor. The diagrams and results are shown in APPENDIX A.

The voltage calibration was done by removing a PV module from the system illustrated in figure 5.4. The schematic representation of the system shown in figure A.1 of Appendix A, describes the calibration of voltage measurements. The remotely controlled ELTEKNIX PSU voltage measurements were manually recorded, while the PCI-730E board was used for transduced voltage measurements. The calibration produced a coefficient of correlation, R^2, very close to one, and the calibration curve is shown in figure A.3 of APPENDIX A.

The calibration of current was done using the system setup illustrated in figure A.2. of Appendix A. The ELTEKNIX PSU current measurements were manually recorded, and the voltage drop across the 0.1Ω resistor was measured by the digital multimeter that was connected to the computer. The calibration produced a coefficient of correlation, R^2, very close to one, and the calibration curve is shown in figure A.3. Figure A.4 illustrates the stability of the measurements.

5.4.5 Capturing I-V curves.

The I-V measurement curves were obtained subject to the instructions described in the system (presented in APPENDIX B). Using the LabVIEW instrument drivers, a LabVIEW programme was written to routinely control the system instrumentation. The programme measured the voltage applied to the PV module and current flowing through it, simultaneously generating I-V data points.

The calibration results calculated in Section 5.4.4 were used to obtain the current, I, as a function of the applied voltage, V, across a PV module. Thus, calibration equations A.1 and A.2 from APPENDX A can be modified to determine I and V:

$$V = 11.905 V_{trans} + 0.186 \tag{5.1}$$

and

$$I = 89.285 V_{drop} + 0.00178 \tag{5.2}$$

Equations 5.1 and 5.2 were incorporated in the LabVIEW program written for this study in order to generate I-V data points.

The LabVIEW programme written required the voltage step and range to be set manually before it run. Figure 5.8 illustrate the flow chart of the LabVIEW programme. When the programme is running, the programmable PSU remotely controls the 60/30 PSU which applies a voltage to the PV module, and this voltage is transduced and measured by the PCI-730E's appropriate channel, while the voltage drop across the resistor is measured by the multimeter. Using equations 5.1 and 5.2,

the measurement conversions are made to obtain a dark I-V curve. Figure 5.9 shows the output of the LabVIEW tool. The computer stores the measured data for further analysis.

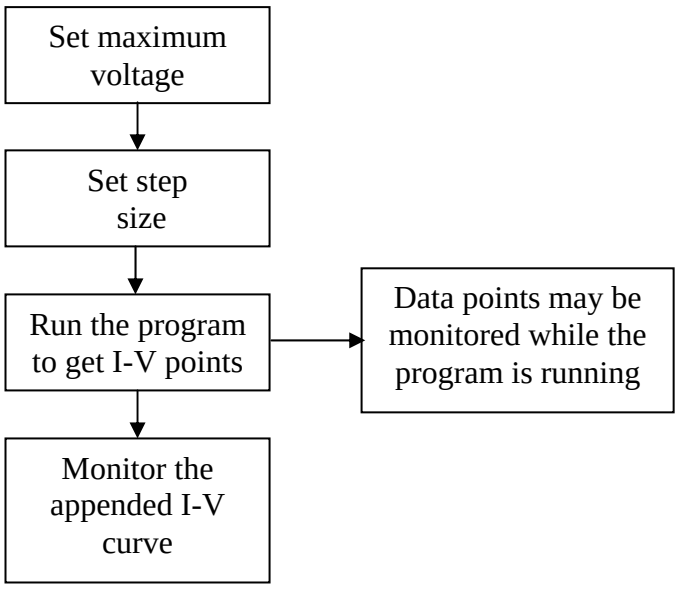

Figure 5.8: *Flow chart illustrating LabVIEW program used to obtain dark I-V curve.*

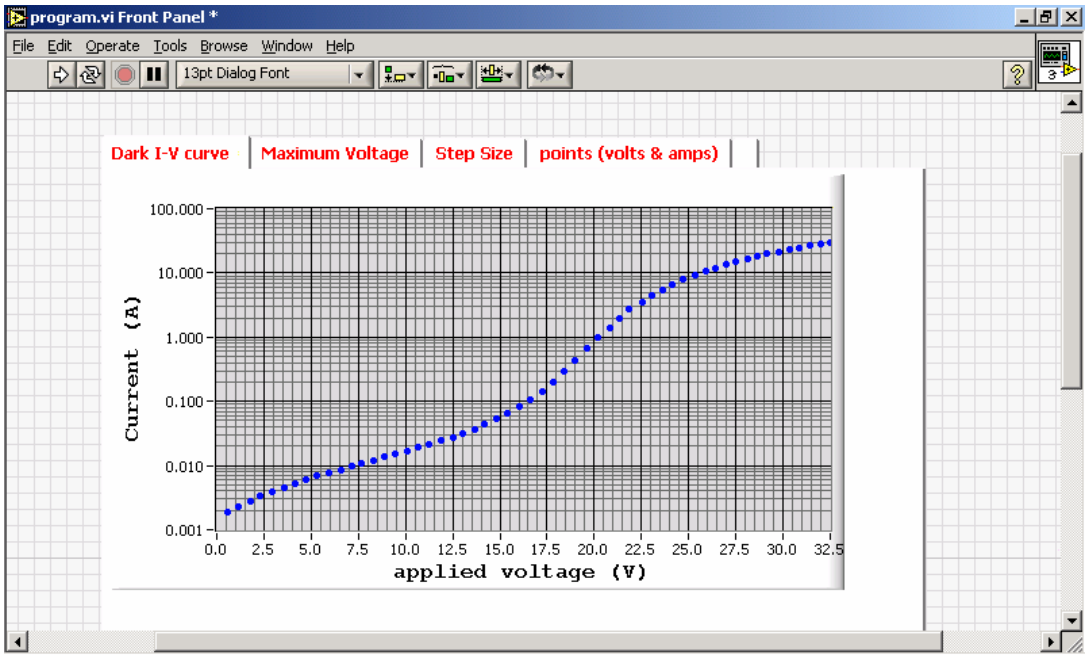

Figure 5.9: *LabVIEW's front panel showing I-V curve.*

The time it takes to obtain an I-V curve depends on the voltage step size; for example, using a 0.1V step size, it takes approximately 2-3 minutes to complete the measurements. When performing I-V measurements at different temperatures, however, the complete I-V curve was obtained in approximately 1-1.5 minutes and within $\pm 5\ ^0C$ of the cell temperature.

5.5 PARAMETER EXTRACTION METHOD

The dark I-V characteristics of solar cells and PV modules are described by equation 3.14. From equation 3.14, the device parameters I_{01}, I_{02}, R_s, R_{sh}, and n can be determined by fitting equation 3.14 to a set of measured I-V data points. Dark I-V measurements were performed using the low- and high-current measurement systems. In both systems, dark I-V data obtained were used to extract device parameters. The non-linear parameter estimation software, *FitAll* from MTR software, was used to fit equation 3.14 to the I-V data measured [King, 1997; MTR software, 1998].

The *FitAll* software has different iterative models to evaluate equation 3.14, R_{sh} can be estimated from the low-current regions, n and I_0 from the mid-current regions, and R_s from the high-current regions. In this study, two models from *FitAll* were used to obtain the parameters: the non-ideal model [MTR software, 1998; 76] and the low-range model for solar cells [MTR software, 1998; 136]. The parameters I_{02}, R_s, R_{sh}, and n can be obtained using the non-ideal model, while I_{02}, R_{sh}, and n can be estimated using the low range model.

5.6 RESULTS AND DISCUSSION

In this study, dark I-V measurements have been performed using the dark I-V systems described previously. The dark I-V characteristics have been commonly used to evaluate the performance parameters of PV cells and modules, and they also give indication of the influence of the parasitic series and shunt resistances on the module [Fang, 1978; Handy, 1967; Hamdy, 1987; King, 1997].

The shape and curvature of dark I-V profile indicates the effect of series and shunt resistances on the solar cell at high and low current ranges, respectively, while the linearity at mid current levels indicates non-ideal carrier recombination losses within the *p-n* junction of a solar cell [King, 1997].

This section presents the results obtained for PV modules of different types, using the low and high current measurement systems. Firstly, the results obtained using the low current measurement system are presented, and then the results from the high current measurement system are discussed. *FitAll* software has been used to fit equation 3.14 to the I-V data measured, and the performance parameters including I_{01}, I_{02}, R_s, R_{sh}, and n were obtained.

5.6.1 Low current measurements.

Figure 5.10 shows the two CIS test modules used in this study. The analysis of CIS-based solar cells and PV modules is presented in Chapter 4. These modules of six isolated solar cells are products from the University of Johannesburg (Rand Afrikaans University - RAU series). They have dimensions of 4 cm x 3 cm area. For this study, these mini modules are referred to as C20+ and SG mini modules, and the table in figure 5.4 indicates the schematic representation of both modules.

Dark I-V characteristic for both modules were obtained for each cell. During dark I-V measurements, forward biasing is achieved by making contacts on the areas illustrated in figure 5.4. Dark I-V characteristics of C20+ and SG CIS modules were obtained using the dark I-V system described in Section 5.3.

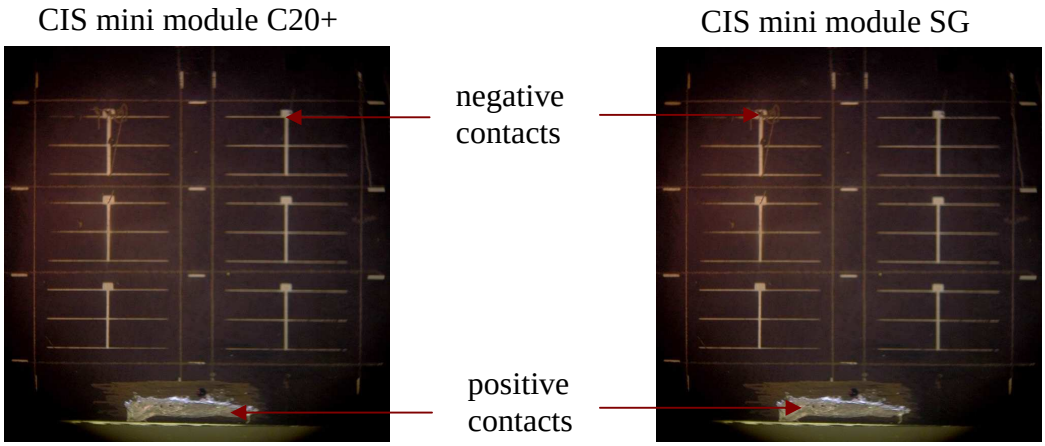

1	**4**
2	**5**
3	**6**

Figure 5.4: *CIS-based modules and table showing the number of cells in both modules.*

The dark I-V measurements of the individual cells of the CIS modules shown in figure 5.4 are illustrated in figures 5.5 and 5.6.

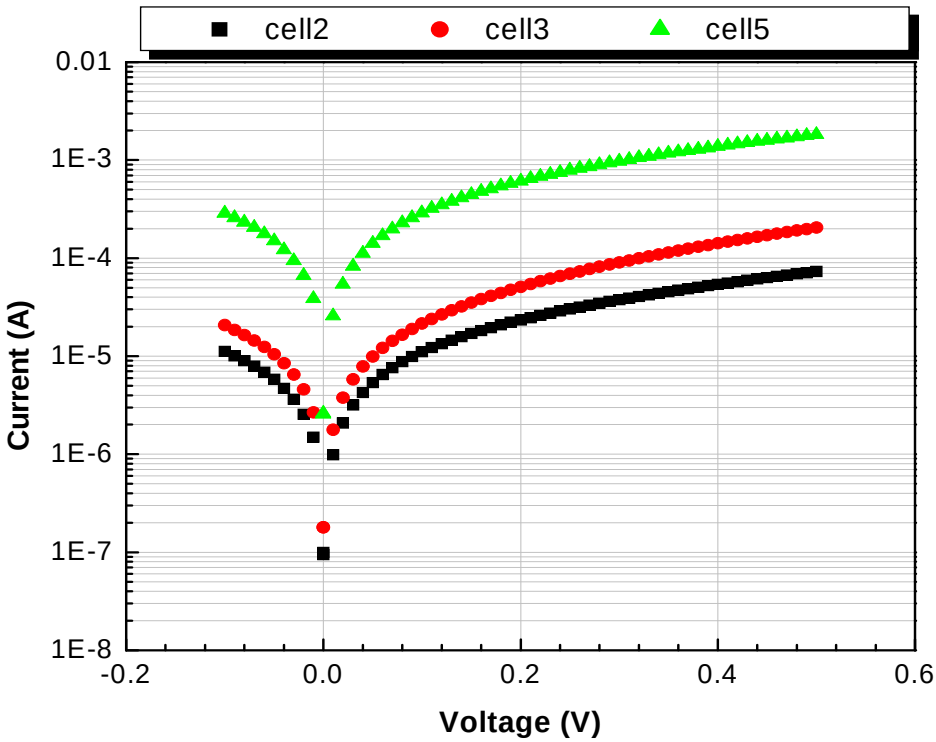

Figure 5.5: *Dark I-V measurements of C20+ CIS solar cells*

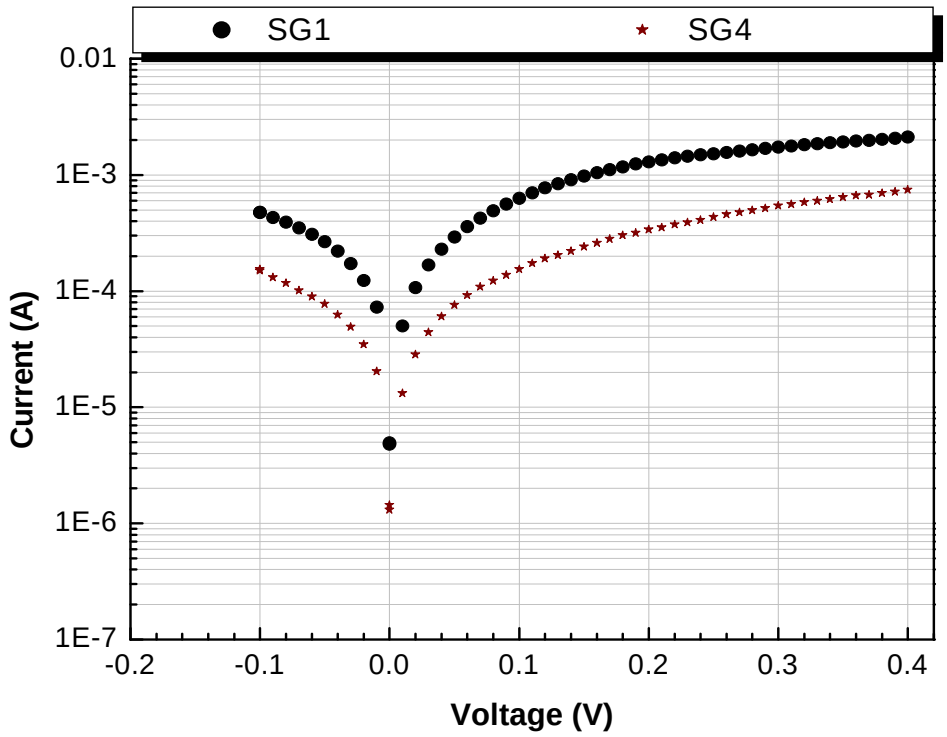

Figure 5.6: *Dark I-V measurements of SG CIS solar cells.*

In this study, dark I-V measurements were performed for both forward and reverse bias. Under forward bias (V > 0), the dark I-V measurement profiles indicate the effect of shunt resistances at low current ranges and the effect of series resistances at high current ranges with ideal regions at the mid current range. Reverse biasing (V < 0), however, allows the effect of reverse saturation current of a solar cell to be seen.

It is evident from figures 5.5 and 5.6 that the dark I-V measurements do not reveal all regions that describe the dark I-V profile. The deviations from the linearity at low measurement levels due to shunt resistances of the solar cell, are indicated. Regions influenced by series resistances of the cell and the non-ideal recombination losses with the *p-n* junction could not be explored because of current saturation at the higher current level ($\sim 10^{-2}$ A).

In order to estimate parameters for the dark I-V characteristics shown in figures 5.5 and 5.6, *FitAll* software was used to non-linearly fit equation 3.14 to extract the necessary parameters. The model used in this study was the low current range model

for solar cells. This model was chosen to best fit the measured dark I-V data. Figures 5.7 to 5.11 show the fitted dark I-V measurements of the curves shown in figures 5.5 and 5.6. The low current range model estimate parameters including R_{sh}, I_{02}, and n. Tables 5.1 lists estimated parameters for the corresponding measurements shown in figures 5.7 to 5.11. The standard deviations indicate that the estimated parameters accurately describe the dark I-V characteristics of the solar cell.

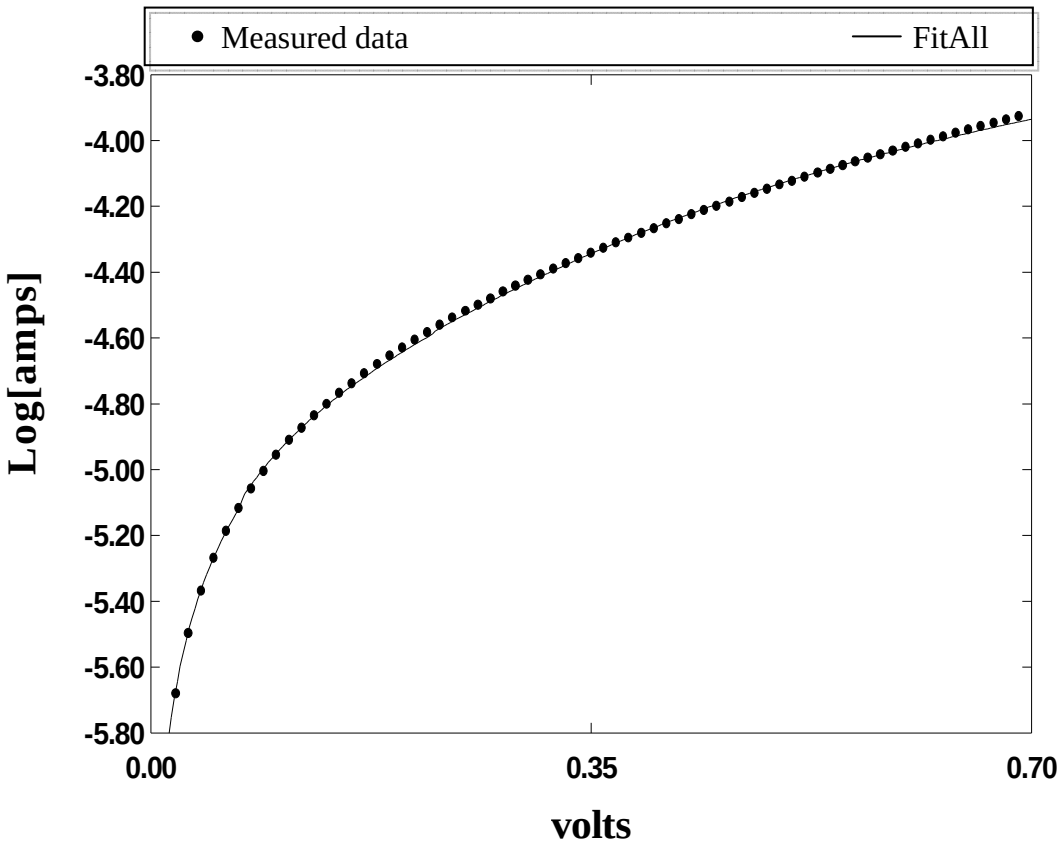

Figure 5.7: *Dark I-V measurements of C20+ cell2*

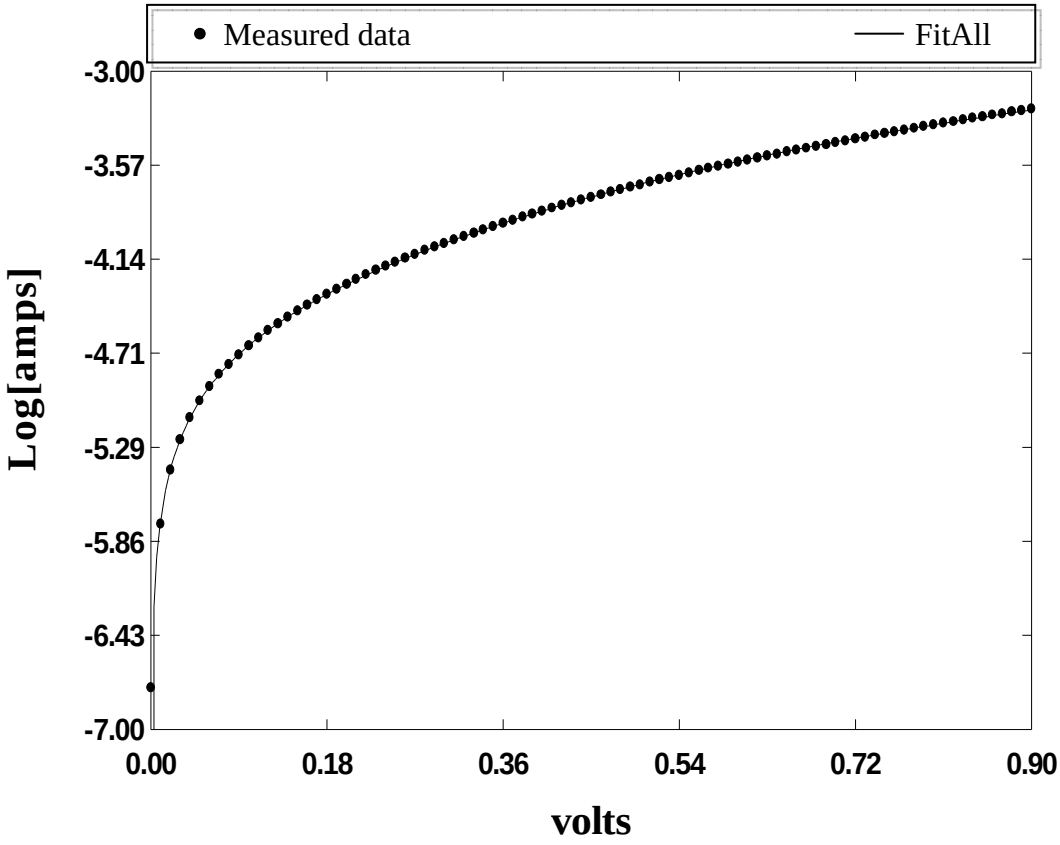

Figure 5.8: *Dark I-V measurements of C20+ cell3.*

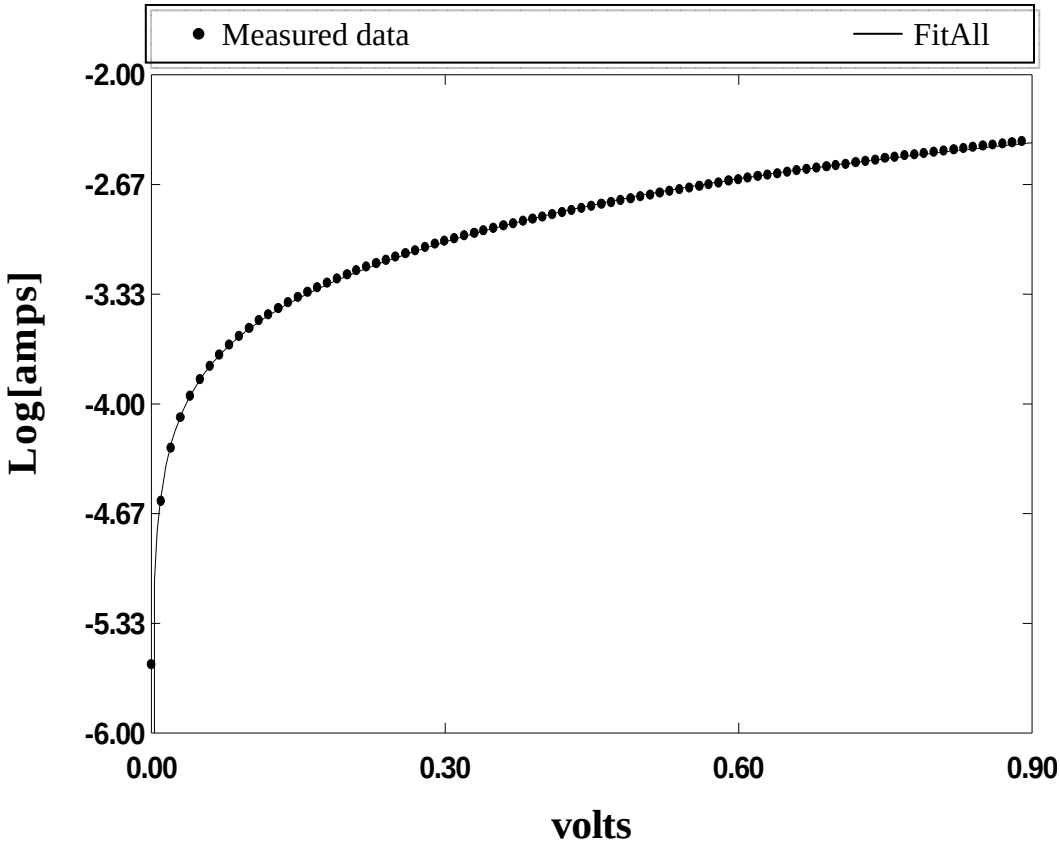

Figure 5.9: *Dark I-V measurements of C20+ cell5.*

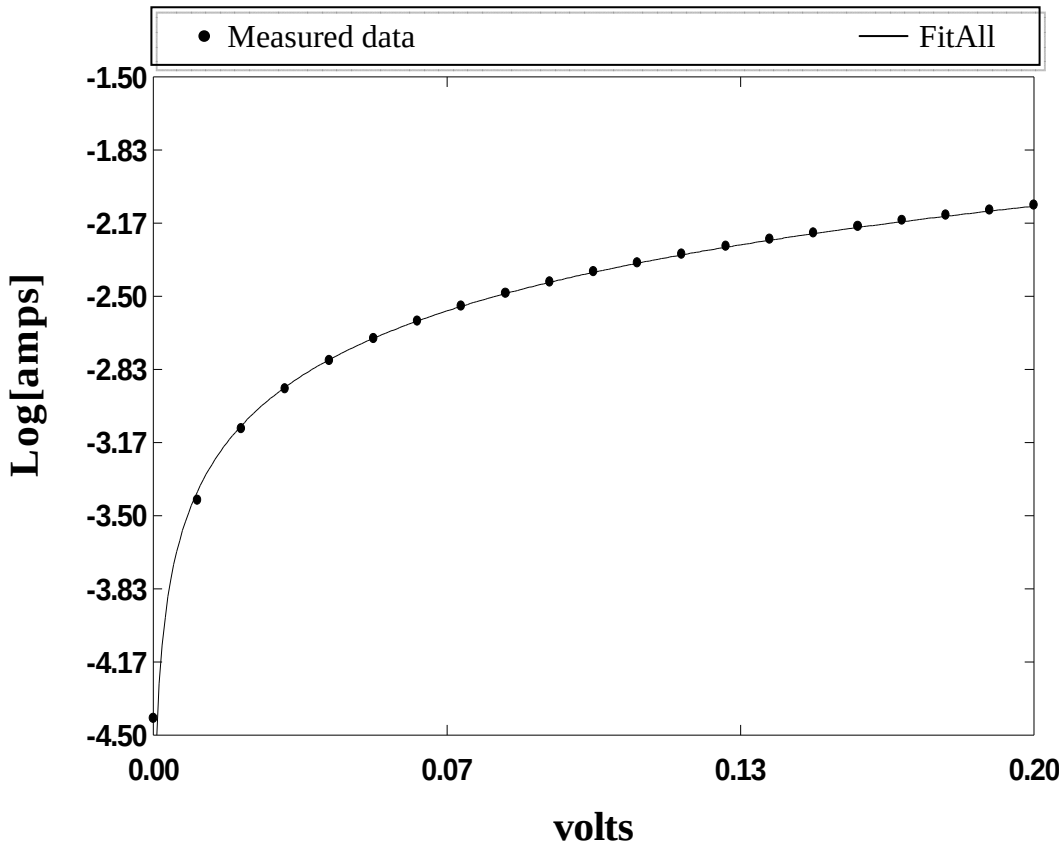

Figure 5.10: *Dark I-V measurements of SG1.*

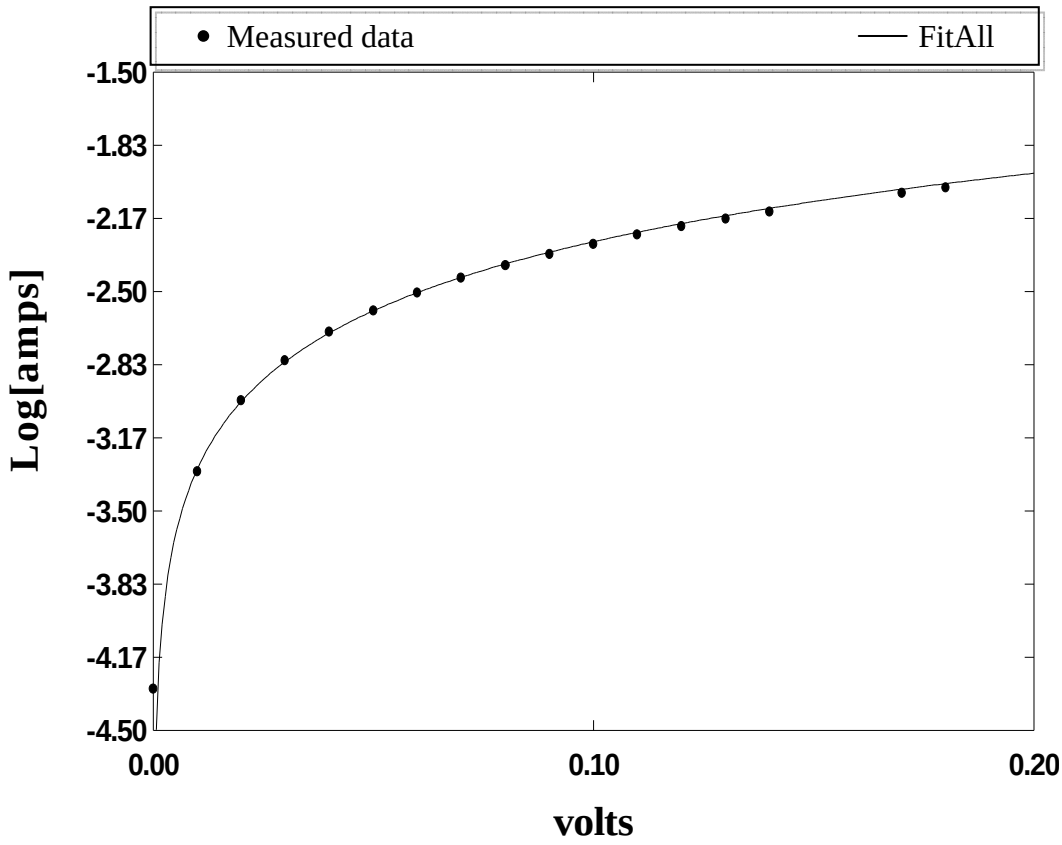

Figure 5.11: *Dark I-V measurements of SG4.*

Table 5.1: *Estimated parameters obtained using FitAll theoretical fit to the measured dark I-V data shown in figures 5.7 to 5.11. Also listed are the standard deviations of the fit.*

Module	Cell	R_{sh} (Ω)	I_0 (A)	n	Std dev.
C20+	2	1.016×10^{1}	4.666×10^{-10}	2.189	1.304×10^{-2}
	3	3.699×10^{1}	1.499×10^{-11}	1.391	2.063×10^{-3}
	5	1.796×10^{2}	6.489×10^{-8}	2.364	2.704×10^{-2}
SG	1	1.490×10^{2}	1.036×10^{-8}	1.746	4.191×10^{-2}
	4	2.092×10^{1}	4.780×10^{-8}	2	2.951×10^{-3}

With reference to figure 5.5, it is expected that the cells will have significantly different R_{sh} values because of the shape of the I-V curve in the low current range. This is indeed the case when comparing the fitted parameters with cell 5 having the highest R_{sh} (= 180 Ω) compared to R_{sh} = 10 Ω for cell 2. A smaller R_{sh} value implies current loss when the device is in operation, resulting in a reduction of fill factor of the module.

The saturation current arises when the electron-hole recombination changes in a *p-n* junction. During the injection process, recombination current or diode current is very much dependant on the number of injected carriers. Saturation current I_0 increases with an increase in the injection process

When comparing the other fitted parameters, I_0 and *n*, the values are also in agreement with the observed curves of figure 5.5. Despite having a high shunt resistance, the *p-n* junction of cell 5 is not as good as the other cells shown by the higher saturation current and diode ideality. Cell 3, with low I_0 and *n* and acceptable R_{sh} = 37 Ω is then the best cell on that test module.

A similar analysis of test module SG reveals that cells SG1 and 4 are superior to the other cells as is expected from figure 5.6.

5.6.2 High current measurements.

In this part of the study two CIS modules were used in conjunction with three Silicon modules. These five modules of different materials and technologies are: Edge-defined Film-fed Growth silicon (EFG-Si), amorphous silicon (a-Si), multicrystalline silicon (m-Si), and two CIS modules (ST 10 and ST 20).

The EFG-Si and m-Si modules used in this study were manufactured by Africa Solar. The CIS and a-Si modules were manufactured by Siemens Solar. The specifications of these modules are listed in table 5.2. The performance parameters maximum power, $P_{\max}$, open-circuit voltage, V_{oc} and short-circuit current, I_{sc}, obtained at standard test conditions (1000 W/m^2 irradiance, 25 °C cell temperature and AM 1.5 global spectrum) using the SPIRE SUN simulator, are also listed in table 5.2.

Table5.2: *Specifications of PV modules used in this study.*

Module	P_{max} **(W)**		V_{oc} **(V)**		I_{sc} **(A)**
	Manufacturer	STC	Manufacturer	STC	STC
ST 10	10	9.31	30	25.97	0.70
ST 20	20	20.11	25	23.92	1.48
EFG-Si	50	50.39	21	21.39	3.34
a-Si	14	7.40	14	23.18	0.73
m-Si	53	48.3	21.3	20.99	2.943

The dark I-V characteristics of the modules listed in 5.6 were obtained using the dark I-V system described in Section 5.4. The measurements were performed at room temperature. Figure 5.12 shows the dark I-V characteristics of the modules listed in table 5.2.

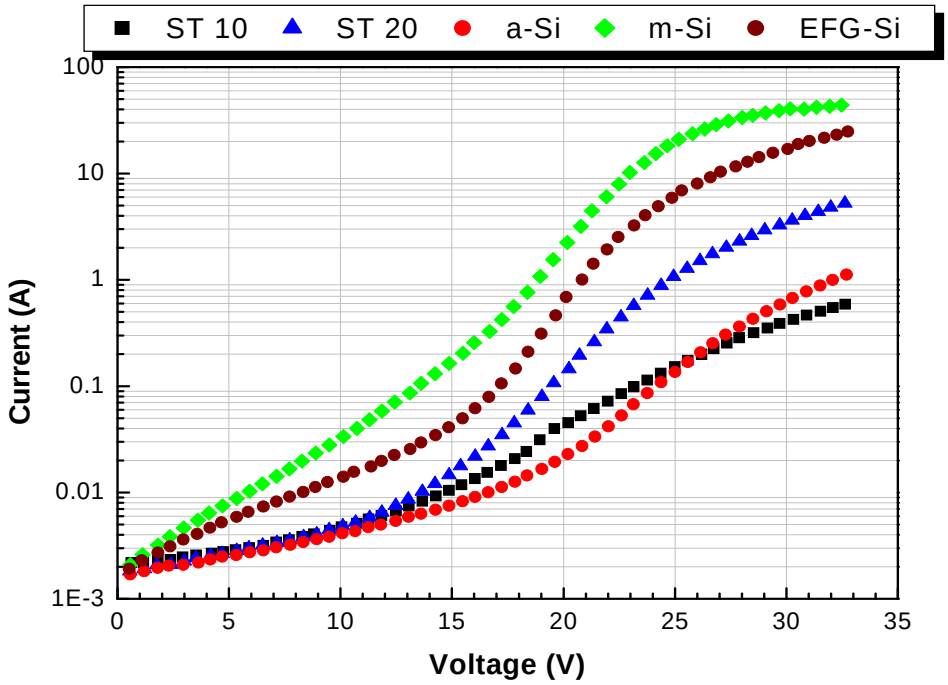

Figure 5.12: *Dark I-V measurements of different types of PV modules available commercially.*

Considering figure 5.12, it is evident that the dark I-V characteristics of the modules that have been studied, illustrate the different regions of dark I-V profile. The measurements were performed at low and high voltage ranges to increase the sensitivity of evaluating the effect of shunt and series resistances on modules. Figure 5.12 also reveals that thin film based modules, ST 10, ST 20 and a-Si, follow similar patterns at low current levels. This indicates that due to the different materials involved in making thin film solar cells, there exist interface states formed at the *p-n* junction between the two materials [Zweibel, 1990]. The interface states have been discussed in Chapter 4, and may cause unwanted shunting paths within the junction leading to the reduction of module power. It is further shown that multicrystalline modules (m-Si and EFG-Si) follow the same trend at low current levels. It is evident also that at low current ranges, there is a significant difference between modules based on crystalline materials and the based on thin film materials.

The deviation from the ideal curve at low current ranges is due to small shunt resistances, while the deviation at higher current levels is due to large series

resistances. EFG-Si has the highest deviation at higher current ranges as compared to ST 10, which showed a small deviation at high ranges. This implies that, when EFG-Si and ST 10 modules are under irradiance, there may be higher voltage losses due to series resistance in EFG-Si cells than in ST 10 cells.

In order to perform parameter extraction for the dark I-V measurements shown in figure 5.12, the non-ideal model from *FitAll* software was used. This model was chosen to obtain the best fit to the measured data. Figures 5.13 to 5.17 show the fitted dark I-V characteristics of the data shown in figure 5.12. The symbols represent the measured data and the solid line indicates the theoretical fit using the non-ideal model to estimate parameters.

Device parameters including I_0, R_s, R_{sh}, and n were obtained, and are listed in table 5.3. The corresponding standard deviations of estimated parameters are also listed. The standard deviation of the fit indicates that the estimated parameters are in good accordance with the real values.

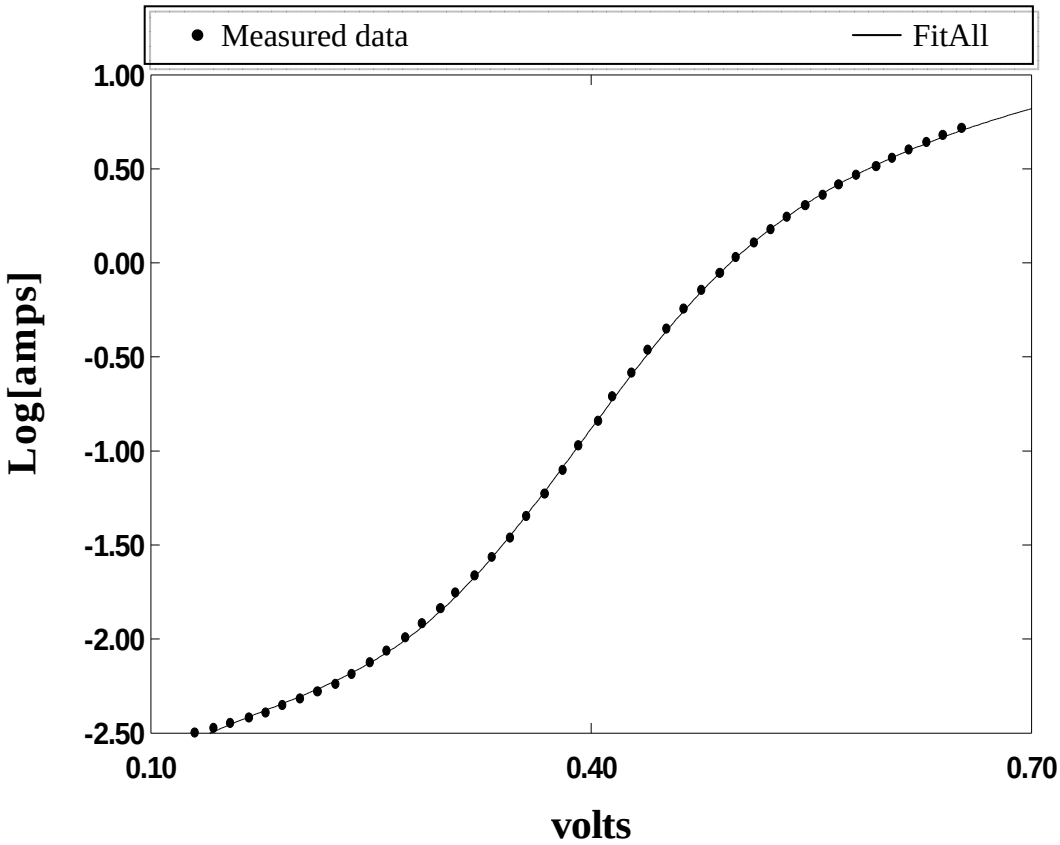

Figure 5.13: *Dark I-V measurements of a ST 10 solar cell.*

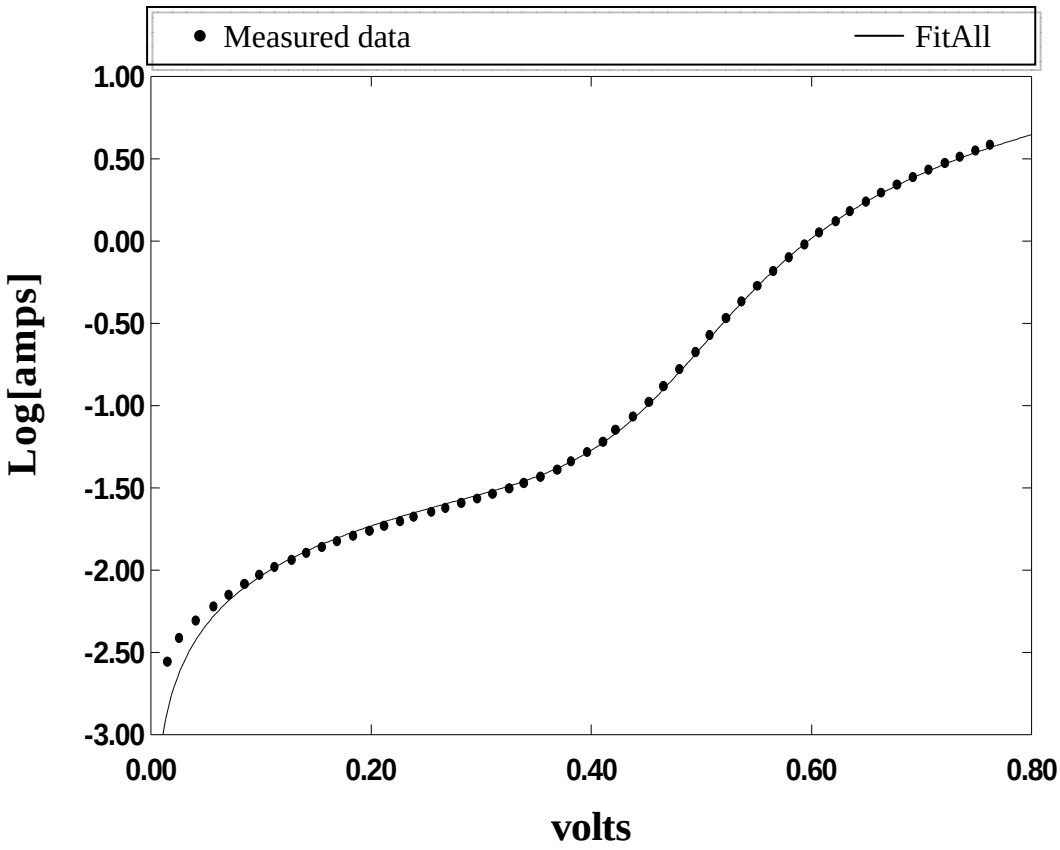

Figure 5.14: *Dark I-V measurements of a ST 20 solar cell.*

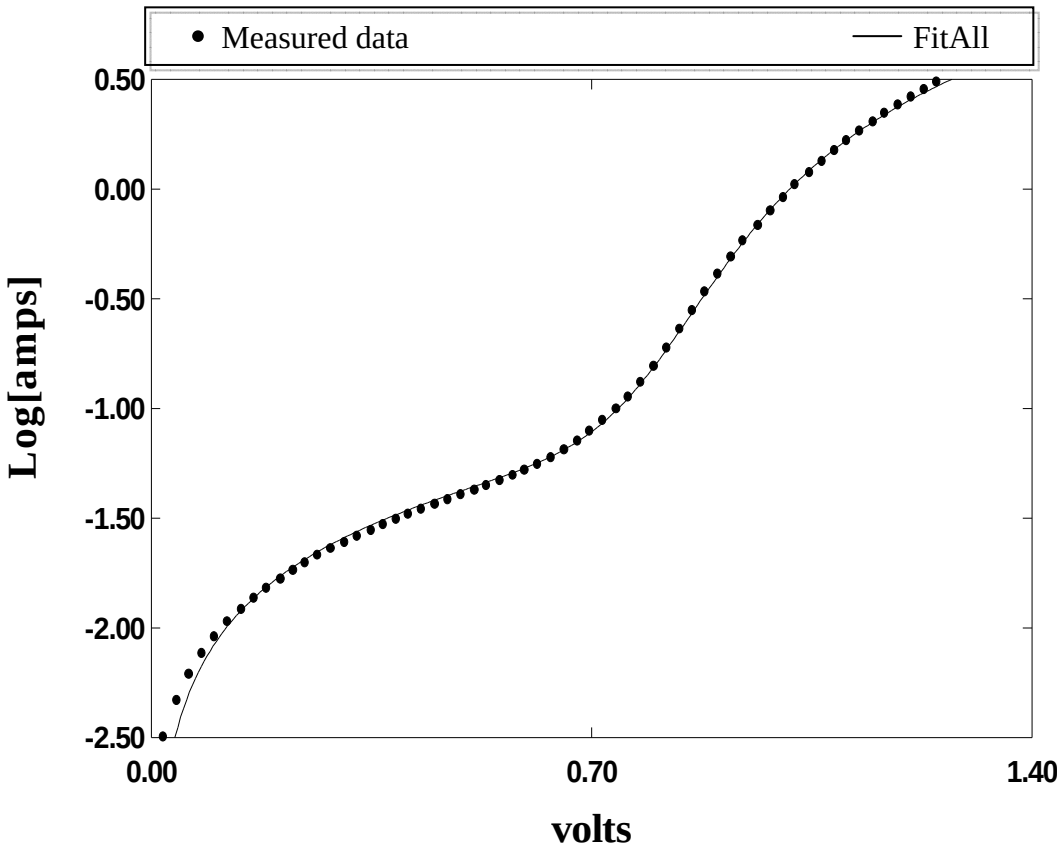

Figure 5.15: *Dark I-V measurements of an a-Si solar cell.*

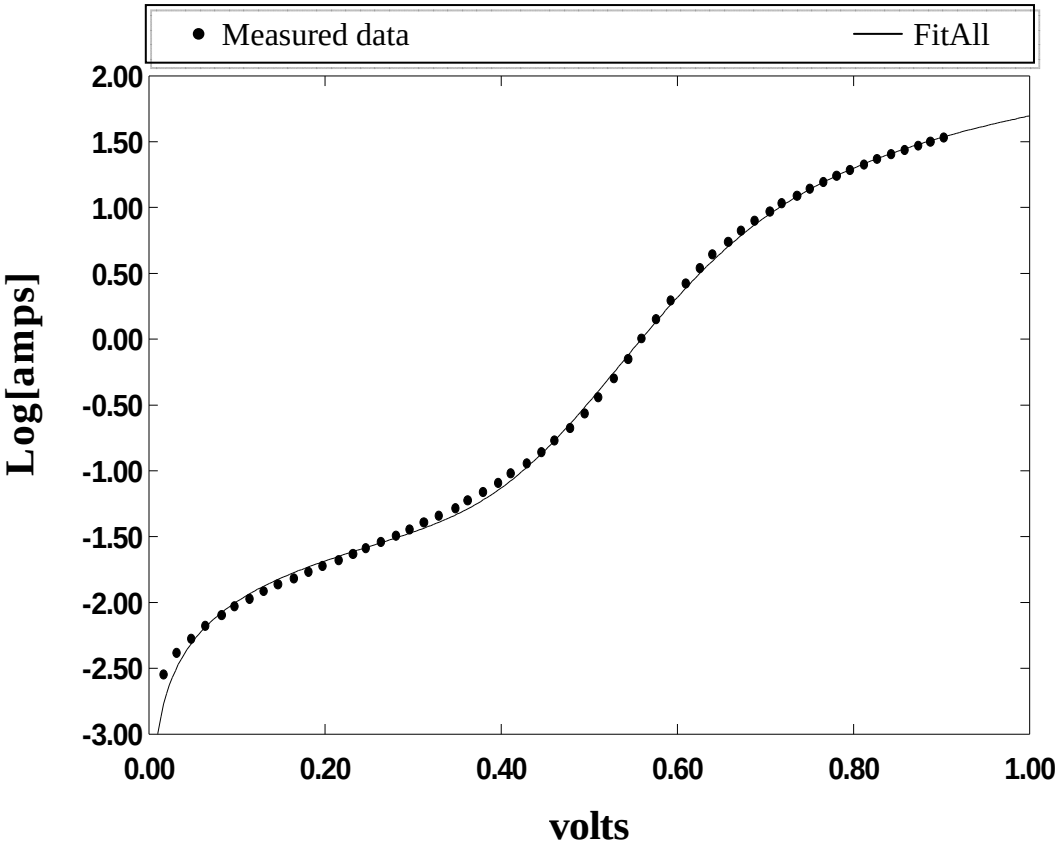

Figure 5.16: *Dark I-V measurements of an m-Si solar cell*

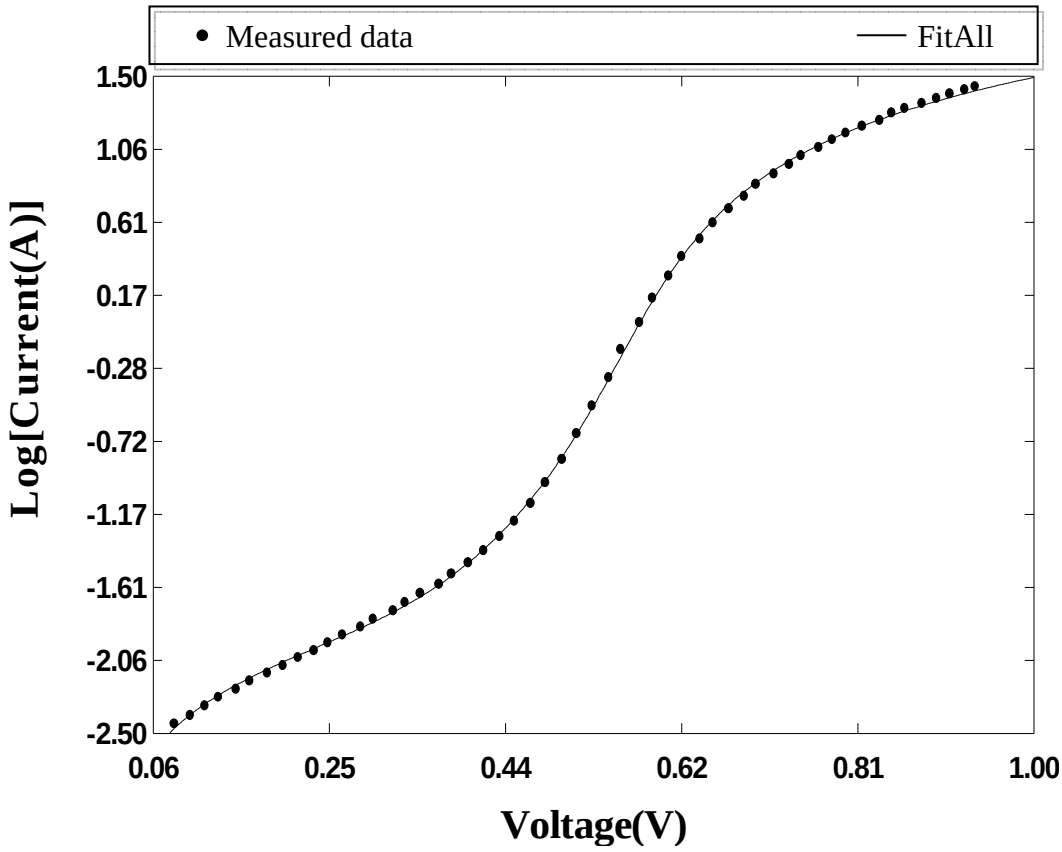

Figure 5.17: *Dark I-V measurements of an EFG-Si solar cell.*

Table 5.3: *Estimated parameters obtained using FitAll theoretical fit to the measured dark I-V data of the curves shown in figures 5.13 to 5.17. Also shown are the standard deviations of the fits.r*

Module	R_{sh} (Ω/ cell)	R_s (Ω)	I_0 (A)	n	Std dev.
ST 10	3.091×10^{1}	2.696×10^{-1}	2.073×10^{-6}	1.621	4.291×10^{-3}
ST 20	3.578×10^{1}	1.179×10^{-1}	6.673×10^{-6}	1.797	4.238×10^{-4}
a-Si	7.679×10^{1}	1.433×10^{-1}	2.967×10^{-7}	2.619	4.753×10^{-3}
m-Si	1.058×10^{1}	3.570×10^{-3}	3.129×10^{-5}	1.919	3.853×10^{-3}
EFG-Si	2.500×10^{1}	1.194×10^{-2}	6.545×10^{-7}	1.564	3.375×10^{-3}

The EFG-Si module with low *n* (= 1.564) and saturation current is then the best module compared to other tested modules. For the a-Si, however, which has the highest value of *n*, it can said that the module has a diode with poor quality. To compare series and shunt resistance values of modules, it is convenient to compare the known values of an entire module.

The series and shunt resistances of PV modules can be determined using the estimated values. By multiplying the estimated values obtained using *FitAll* theoretical fit with the number of cells of the module, series and shunt resistances are determined and listed in table 5.4.

Table5.4: *Calculated parasitic resistances of the module used in this study.*

Module	R_{sh} (Ω)	R_s (Ω)
ST 10	1514.74	13.21
ST 20	1717.84	8.62
a-Si	296.24	9.36
m-Si	442.4	0.10
EFG-Si	900.32	0.43

It is evident from the estimated parameters that the R_s values for the multicrystalline Silicon modules (m-Si and EFG-Si) are comparable and, as expected, are lower than the values for the thin film based modules (ST 10, ST 20 and a-Si) which have comparable R_s values. All tested modules have accepted shunt resistances.

5.6.3 Effect of parasitic resistances on PV modules.

Parasitic, series and shunt resistances of a solar cell are important parameters that affect its efficiency [van Dyk, 2004]. In this study, EFG-Si module was used to demonstrate the effect of series and shunt resistances. The I-V characteristics were obtained using the high-current measurement system described in Section 5.4.

5.6.3.1 Effect of series resistance.

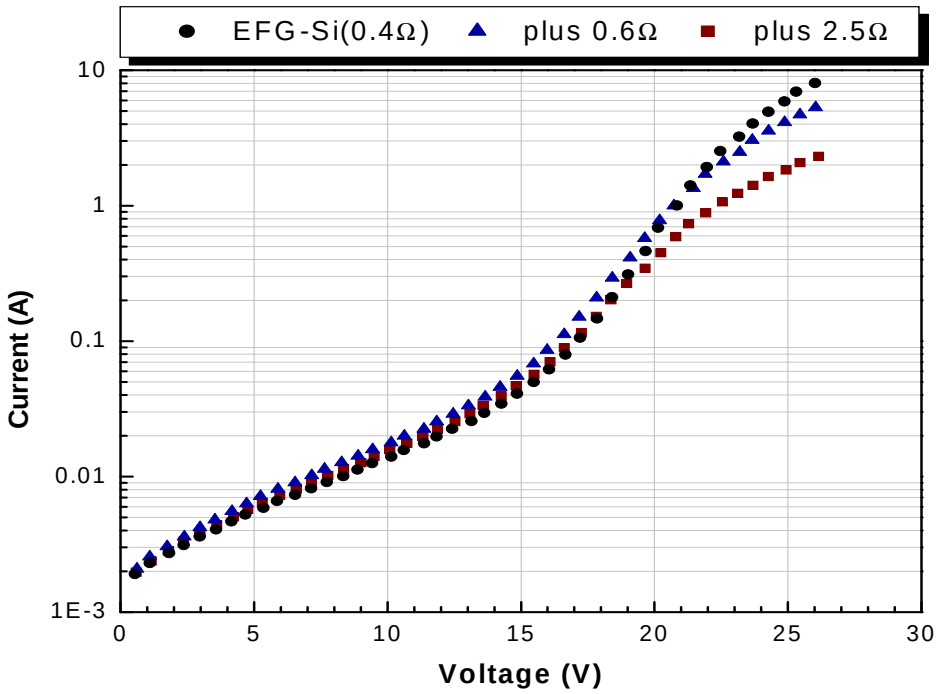

Figure 5.18: *Series resistance effect on the 36-cell series connected EFG-Si module.*

Figure 5.18 illustrates the effect of series resistance in a 36-cell series connected EFG-Si module. The deviations of the curves at high current levels are influenced by the addition of resistances connected in series with the module. It is evident that the

effect only occurs at high current levels. By increasing the series resistance, the current drops rapidly according to the amount of resistance added.

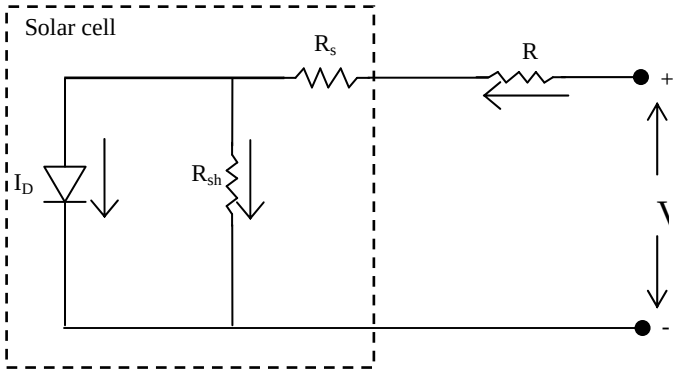

Figure 5.19: *Electric circuit illustrating the effect of series resistance.*

Figure 5.19 shows the circuit configuration for investigating the effect of series resistance. The resistance, R, is connected in series to the PV module and the value varied as recorded in figure 5.18. As resistance R increases, there is a significant voltage drop across it. This has a detrimental effect on solar cells and modules, with a reduction in fill factor and consequently loss in power.

5.6.3.2 Effect of shunt resistance

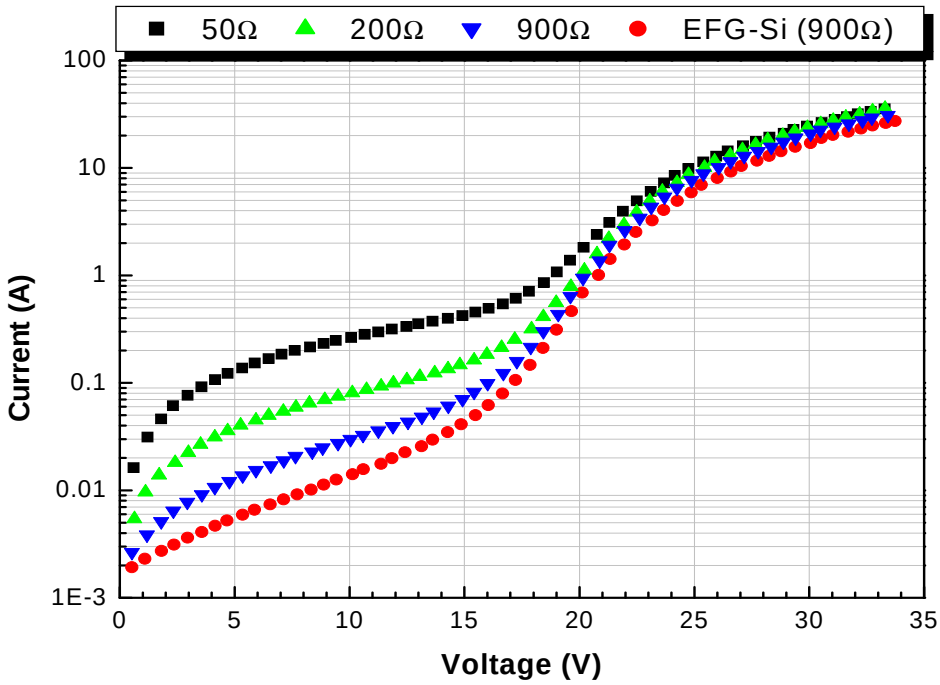

Figure 5.20: *Shunt resistance effect on the 36-cell series connected EFG-Si module.*

Shunts (local defects of the *p-n* junction) can noticeably decrease the cell efficiency, mainly by decreasing the short-circuit current, which results in the maximum power point occurring at lower voltage, thus reducing the fill factor. This could happen when the PV module is in operation, and is particularly detrimental to device performance at low irradiance levels. Figure 5.20 shows the dark I-V measurements of the EFG-Si module with a shunt resistance effect.

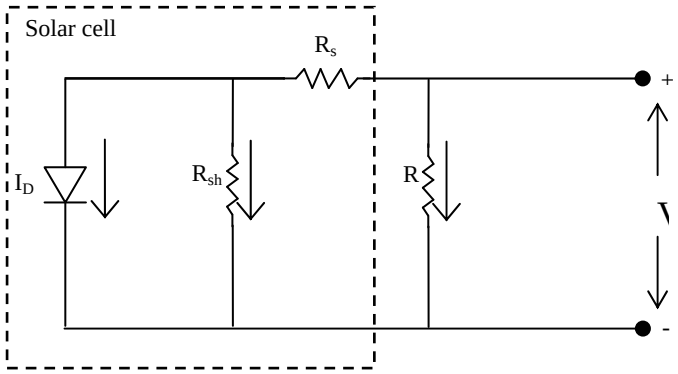

Figure 5.21: *Electric circuit illustrating the effect of shunt resistance.*

Figure 5.21 shows how the current flows in this situation, when the test resistance, R, is connected in parallel across the module. Since $R_s << R_{sh}$ we can neglect Rs for the purposes of this discussion. As expected, when any R is connected as shown, the effective resistance of the combination (R_{sh} and R) will be smaller than R_{sh}. Since R_{sh} was measured to be 900 Ω it was decided to use R values of 900 Ω and less. At R = 900 Ω, the effective resistance would be half of R_{sh} and the current in the low range where R_{sh} has the largest effect, will be doubled. This is clearly seen at any low test voltage, say 2.0 V. Further reduction in R increases the current as observed in the lower current range in figure 5.20.

It is worthwhile to note that using a variable resistor is a quick method to determine shunt resistance for a PV module. A test forward voltage is chosen and applied; say 2.0 V, and the current measured. A variable resistor is connected in parallel and the resistance adjusted to yield double the current. This resistance then matches the module shunt resistance. Using this method, shunt resistance of each of the module used in this study are listed in table 5.5.

Table 5.5: *Measurements of shunt resistance for each of the module used in this study.*

Module	R_{sh} (Ω)
ST 10	1275
ST 20	1590
a-Si	260
m-Si	400
EFG-Si	884

The R_{sh} values measured using the method described above agree with those estimated using *FittAll* theoretical fit software. This is evident from the small difference between values listed in table 5.5 and table 5.4. Therefore the method described above can be used for measuring shunt resistance of a PV module.

5.6.4 Effect of temperature on solar cells and PV modules

The dark I-V measurements were performed at 70 °C, 60 °C, 50 °C, 40 °C and 30 °C cell temperatures to facilitate investigation of the effect of temperature on dark I-V characteristics.

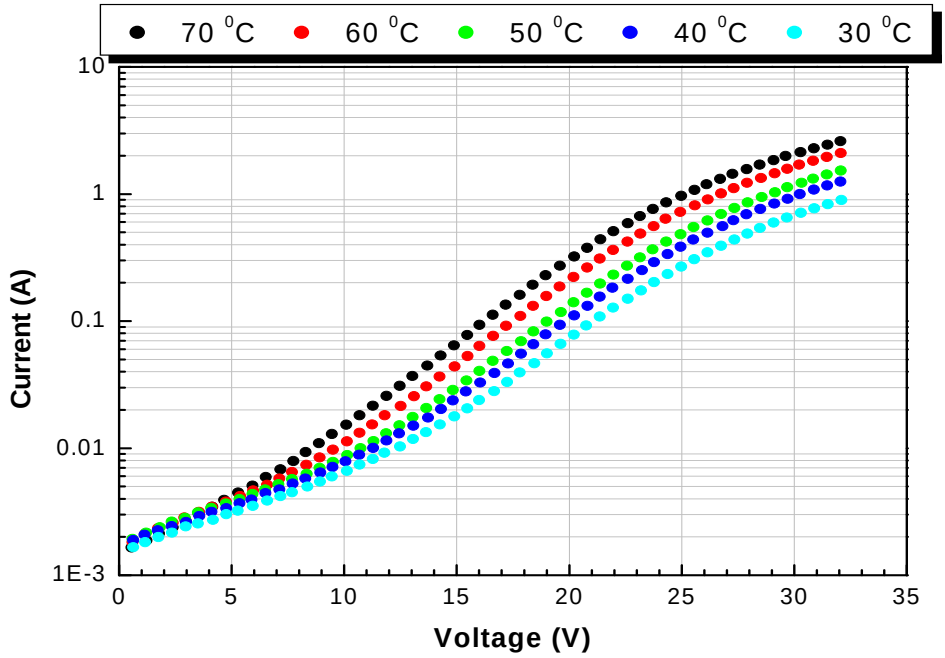

Figure 5.22: *Effect of temperature on ST 10 module.*

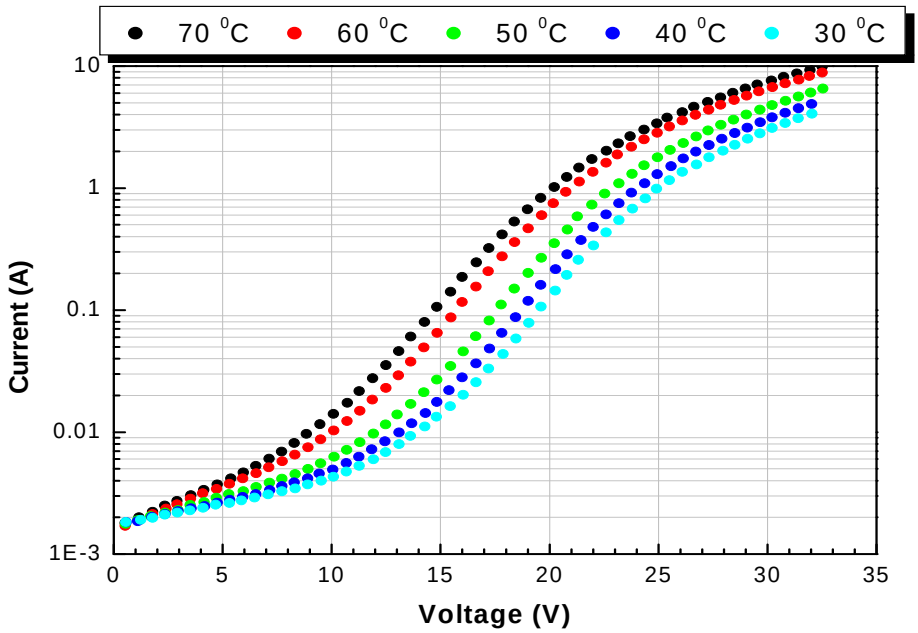

Figure 5.23: *Effect of temperature on ST 20 module.*

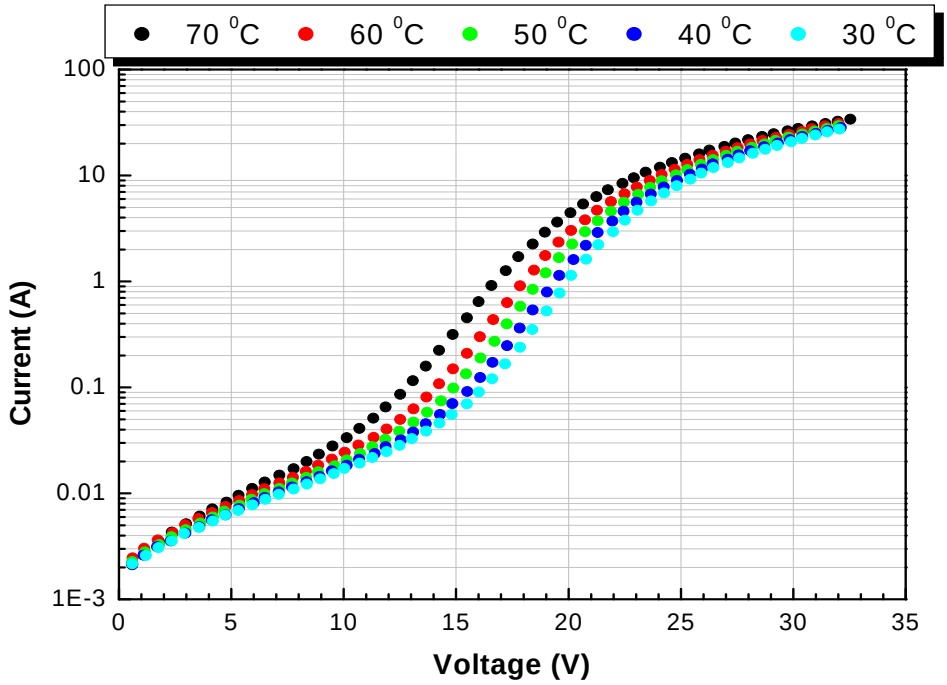

Figure 5.24: *Effect of temperature on EFG-Si module*

Figures 5.22 through 5.24 show the dark I-V curves measured at different temperatures for the ST 10, ST 20 and EFG-Si modules, respectively.

Referring to equation 3.14, it is expected that R_{sh} should be independent of temperature. This is indeed the case for all three modules. In the mid-voltage range there is an increase in current with increase in temperature. This indicates an effective reduction in recombination in the SCR which may be associated with the change in material bandgap in temperature and related reduction in band-edge recombination defects.

In the higher voltage range there is, however, a difference between the technologies. The EFG-Si exhibits a change in the effect of R_s, while the CIS modules (ST 10 and ST 20) show an increase in current with temperature in the mid and high-voltage ranges. The deviation from linearity in the effect of R_s for the CIS modules remains fairly constant, but there is a definite increase in R_s at higher temperatures for the EFG-Si module.

5.7 SUMMARY AND CONCLUSIONS

This study was originated with the intention of investigating factors that influence the performance of solar cells and photovoltaic modules. The dark I-V investigations provide useful information in understanding these factors contributing to low performance of solar modules. The analysis enables the determination of device parameters including parasitic, series and shunt resistance.

This study has presented the methodology for performing dark I-V characterization of solar cells and PV modules. The performance parameter values were based on the use of non-linear parameter estimation.

The series resistance in a solar cell limits the current while the shunt resistance provides a way for current to bypass the diode device. The work also demonstrated the effect of series and shunt resistance in the PV modules. The viability of the technique was demonstrated with the series and shunt resistance test measurements. It can be concluded that high shunt resistance reduces non linearity of the dark I-V behavior at lower current ranges. Whereas low series resistance limit the deviation of the dark I-V profile at higher current ranges. Also, the temperature dependence of PV modules was investigated.

Dark I-V analyses indicate the quality of the solar cell *p-n* junction device. Due to the absence of photogenerated currents, solar cell under darkness functions primarily as a diode.

5.8 REFERENCES.

Chegaar M., Ouennoughi Z. and Guechi, F. (2004), "Extracting dc parameters of solar cells under illumination." *Vacuum*, **75**, pp 367-372.

Fang C. and Hauser J. (1978), "Two Dimensional Analysis of Sheet Resistance and Contact Resistance in Solar cells," *Proceedings of the 12th IEEE Photovoltaic Specialists Conference.*

Hamdy M. and Call R. (1987), "Effect of Diode Identity Factor on Determination of Series Resistance of Solar Cells," *Solar Cells*, **20**, pp 119-126.

Handy R. (1967), "Theoretical Analysis of the Series Resistance of a Solar Cell," *Solid State Electronics*, **10**, pp 765-775.

James G. (2002), *The electrical characterisation of n-GaN and n-AlGaN*, University of Port Elizabeth, MSc-dissertation.

Kaminski A., Marchand J.J.and Laugier A. (1999), "I-V methods to extract junction parameters with special emphasis on low series resistance." *Solid-State Electronics*, **43**, pp 741-745.

King D.L., Hansen B.R., Kratochvil J.A. and Quintana M.A. (1997), "Dark Current-Voltage Measurements on Photovoltaic Modules as a Diagnostic or Manufacturing Tool," *Proceedings of the 26th IEEE Photovoltaic Specialists Conference*, pp 1125-1128.

MTR Software (1998), FitAll Nonlinear Regression Analysis: Research Edition, pp 130-141 (Function Reference).

National Instruments: www.ni.com/**labview**/

van Dyk E.E. and Meyer E.L. (2004), "Analysis of the effect of parasitic resistances on the performance of photovoltaic modules." *Renewable Energy*, **29**, pp 333-344.

Van Kerschaver E., Einhaus R., Szlufcik J., Nijs J., and Mertens R. (1997), *Proceedings of the 14th European Communities Photovoltaic Solar Energy Conference*, pp 2438.

Zweibel K. (1990), *Harnessing Solar Power*, Plenum Press, pp 87.

CHAPTER 6

LIGHT CURRENT-VOLTAGE CHARCTERISTICS OF SOLAR CELLS AND MODULES: INDOOR MEASUREMENTS

6.8 INTRODUCTION

When photovoltaic (PV) modules are deployed outdoors for operation, their performance is affected by environmental factors such as humidity and shading by clouds. This leads to the failure of PV modules to reach their optimum efficiencies. The internal structure of the solar cell may also have factors that impede the flow of current, leading to the reduction of power delivered to a load. The knowledge of a PV module's performance parameters from the measured current-voltage (I-V) characteristics is of vital importance for the quality control and evaluation of the performance of the module. It is therefore essential to evaluate the I-V characteristics of the PV module before they are deployed outdoors for operation.

The preceding chapter discussed the I-V characteristics of solar cells and (PV) modules without the use of a solar simulator, under dark conditions. The dark I-V measurements enabled the determination of diode properties and parasitic resistances. This chapter, however, analyzes light I-V characteristics of solar devices by using the light source unit known as a solar simulator which simulates the solar spectrum. The light I-V characteristics of a solar device are described by the solar device's electrical performance parameters. These include the open-circuit voltage, V_{oc}, the short-circuit current, I_{sc}, of the device, maximum power, P_{max}, voltage at maximum power, V_{max}, current at maximum power, I_{max}, fill factor and efficiency of the device.

The solar simulator simulates the AM 1.5 global spectrum with a light intensity of 1000W/m^2, and can be used to perform I-V measurements at standard test conditions (STC) of 1000 W/m^2 irradiance, AM 1.5 global spectrum and 25 °C cell temperature. To measure the efficiency of a PV module, the indoor measurements under a solar simulator are performed at STC.

In this chapter, the evaluation of PV modules using a solar simulator is presented. The simulator used in this study is described, and then the I-V measurements of $CuInSe_2$-based PV modules and of other technologies are presented and discussed.

6.9 SPIRE SUN 240 SIMULATOR

In this study, the indoor assessment was done by evaluating the I-V characteristics of PV modules with a SPIRE SUN 240 simulator unit that has been approved by the American Society for Testing Materials (ASTM). The SPIRE SUN simulator is designed to imitate the STC.

Figure 6.1 shows a photograph of the SPIRE SUN 240 simulator unit with a PV module mounted on the drawer which has an area 1.47 m^2. The instrumental unit displaying current and voltage measurement meters and dual dials for manually controlling the electronic load is also shown in the figure. The electronic load is capable of biasing the test module in a continuous sweep from short circuit to open circuit conditions, and the load is interfaced to a computer for automatic control to obtain the I-V measurements.

The heart of the SPIRE SUN simulator 240 is a pulsed xenon lamp mounted at the top end of the simulator facing down to provide uniform illumination over a large area of about the size of the unit's drawer. To measure module I-V characteristics, the electronic load takes I-V data readings, at a fixed level below the peak of each flash of the xenon lamp. This lamp is used because of its stability when simulating the global reference spectrum, AM 1.5.

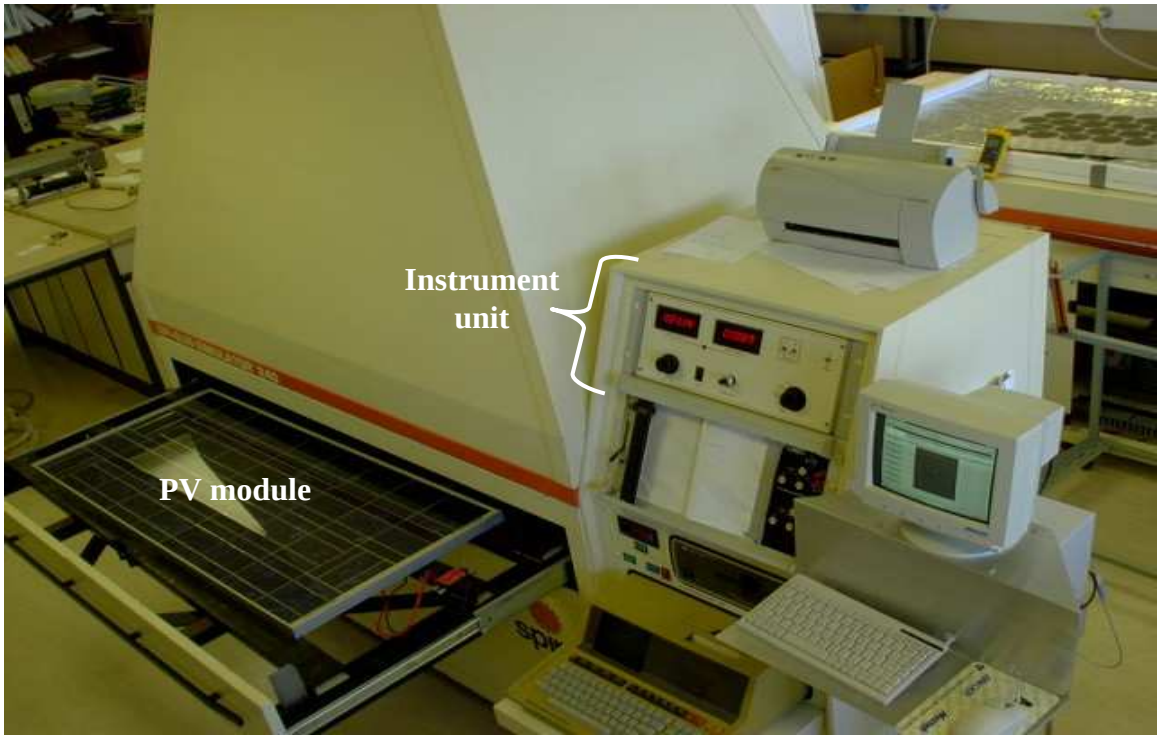

Figure 6.1: *SPIRE SUN simulator 240 used for this study [Gxasheka, 2003; 66].*

Figure 6.2 shows the spectral distribution of the xenon lamp and the AM 1.5 spectrum, illustrating the comparison between the two spectra. The xenon lamp uses 6 kW of power and its irradiance has a uniformity of $\pm 3\%$ over a large area of 80 cm x 130 cm. The xenon lamp requires a voltage range of 200 to 240V ac single phase on a 50A line, and it draws a current at about 43A at 240V ac [Spire Corporation].

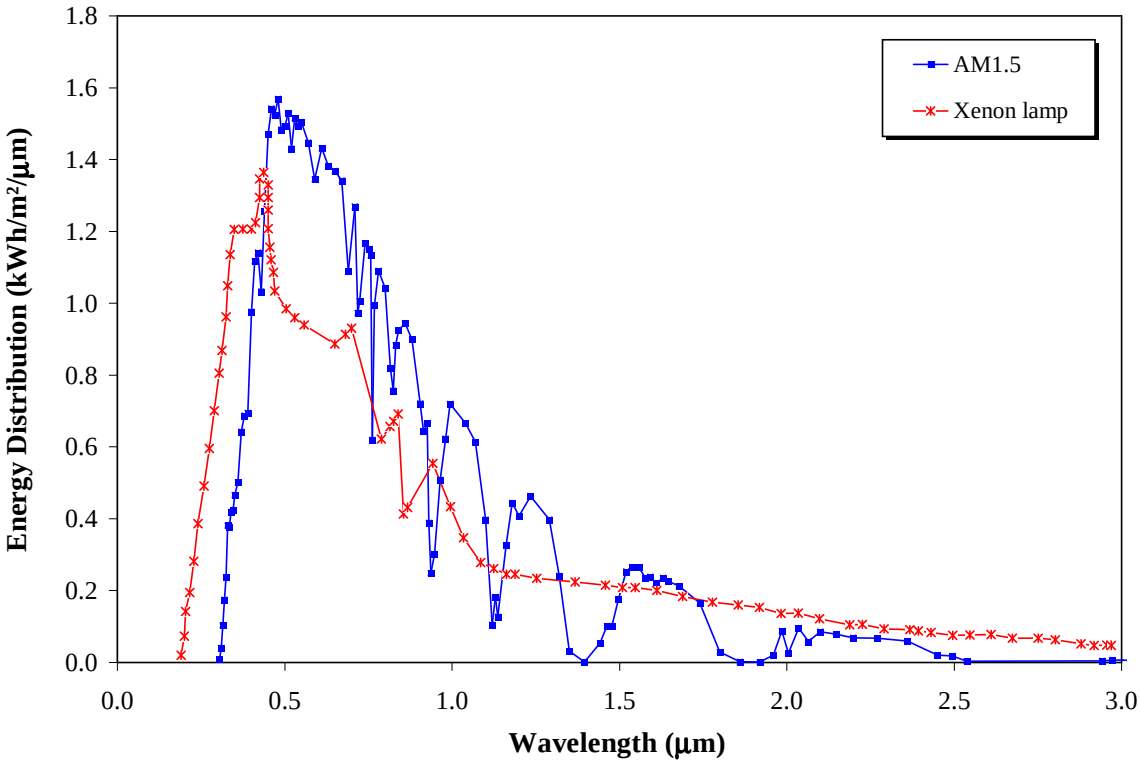

Figure 6.2: *Spectral distributions of pulsed xenon lamp and AM 1.5 [Spire Corporation].*

6.9.1 The simulator calibration

Prior to the measurement, the SPIRE SUN simulator is calibrated subject to the Siemens reference cell, which has an area 10.2 cm x 10.2 cm. This reference cell was pre-calibrated by the Siemens Solar Large Area Pulse Solar Simulator (LAPSS) [Siemens Solar], and consists of a single crystalline silicon (c-Si) cell surrounded by eight dummy cells which allow the distribution of temperature in the active cell to resemble the temperature of the cells in the tested PV module. The simulator is calibrated when I_{sc} of the reference cell is 3.181 A at 25 °C cell temperature. At this stage, I_{sc} is assumed to be directly proportional to the incident irradiance of 1000 W/m^2 [Meyer, 2002]. The c-Si reference cell allows accurate I-V measurements for other crystalline modules. There may however be errors when performing the I-V measurements of different technology modules due to the difference in their spectral responses [Meyer, 2002; 58; Gxasheka, 2003; 68].

6.9.2 Data Acquisition Circuit.

The SPIRE SUN simulator is interfaced to the computer via a data cable which allows the transmission of data between the electronic load and the computer. The data acquisition system consists of the PCI 730E and the PCI 848A acquisition boards.

The PCI 730E has been described in Chapter 5, and is an input/ output analog board with 16 channels. It is used to measure voltage and current simultaneously [Eagle Technology, 2002]. The PCI 848A card is used for digital output from the software program to open/ switch the relay to allow the I-V measurements.

6.10 SYSTEM SOFTWARE

HPVEE programming language has been used previously to perform the I-V measurements. In this study the HPVEE software was replaced with LabVIEW software which enabled the computer to control the electronic load to obtain a full set of I-V data points. The appropriate drivers provided by LabVIEW software for data acquisition were used in this study [National Instruments].

6.11 THE I-V CURVES.

This study used the LabVIEW programme written to measure module I-V characteristics. To measure the I-V curve, the programme controls the PCI 730E card to record voltage and current measurements. When the module is illuminated by the pulsed xenon lamp inside the SPIRE SUN simulator, the operator manually sets the electronic load to measure the V_{oc} and I_{sc} values of the module and the LabVIEW programme records these measurements. The programme then controls the electronic load automatically, obtaining the full set of measured I-V data points.

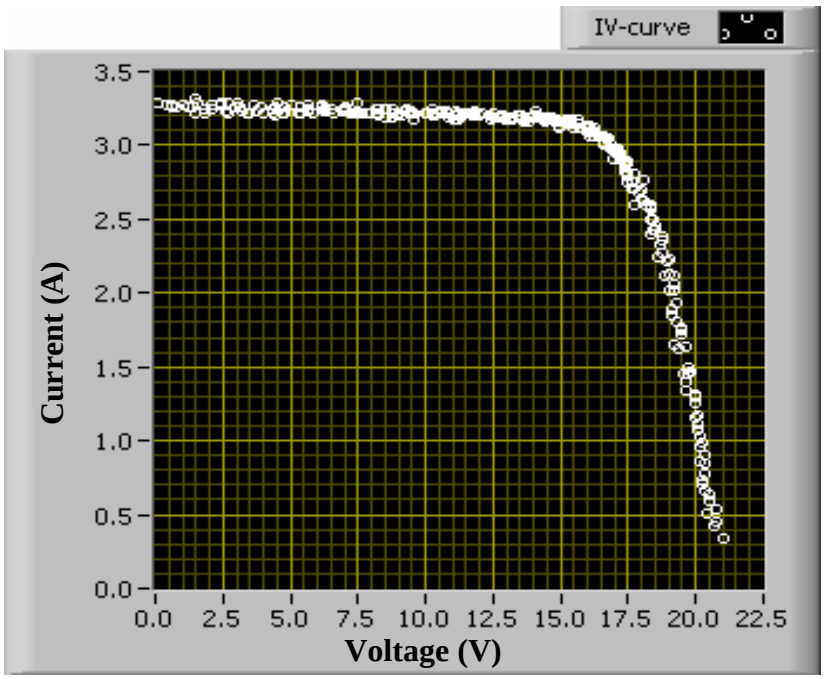

Figure 6.3: *LabVIEW tool showing a typical I-V curve of 36-cell series connected EFG-Si module measured during this study.*

6.12 RESULTS AND DISCUSSION

This section presents the results obtained for the light I-V characteristics of PV modules described by equation 3.17, by using the SPIRE SUN 240 simulator. The performance parameters obtained include V_{oc}, I_{sc}, P_{max}, fill factor and efficiency.

Table 6.1 lists the PV modules used in this study. The $CuInSe_2$-based (ST 10 and ST 20) modules are the products of Siemens Solar, the amorphous silicon (a-Si) was manufactured by PHOENIX GOLD, and the Edge-defined Filmed Growth multicrystalline silicon (EFG-Si) module was manufactured by Suncorp Manufacturing (PTY) Ltd. The manufacturers rated peak powers of these modules and their aperture areas are also listed in table 6.1.

Table 6.1: *Power ratings and aperture areas of the modules used in this study.*

Module	P_{max} (W)	Area (m^2)
ST 10	10	0.118
ST 20	20	0.231
a-Si	14	0.294
EFG-Si	50	0.390

I-V measurements were obtained at STC for the modules listed in table 6.1. The effect of varying the irradiance level on the module parameters is investigated and the results are presented and discussed. The parasitic resistances of the modules used in this study, are determined using the method described in Chapter 3.

6.12.1 The I-V measurements of PV modules at STC

Figure 6.3 shows the I-V characteristics of the PV modules listed in table 6.1 and table 6.2 lists the performance parameters obtained from these I-V curves. As expected, there is a large spread in the output power of the devices. A comparison of the measured and specified power of each module reveals that the a-Si module is producing much less power than it should. This reduced power, 7.4 W, compared to the 14 W specified is the subject of another study on performance of thin-film modules currently underway at the Nelson Mandela Metropolitan University. This large degradation in power is most likely due to material defects leading to lower current collection. In addition, the ratio of P_{max} to the product of V_{oc} and I_{sc}, the fill factor (FF), is much less for the thin-film modules. This is typical for these technologies, but is unusually low for the ST 10 module and very low for the a-Si module. This is indicative of poor material and *p-n* junction quality. This in turn results in lower shunt resistance values. The figure also reveals, as expected that the thin-film modules have higher R_s than for the EFG-Si module.

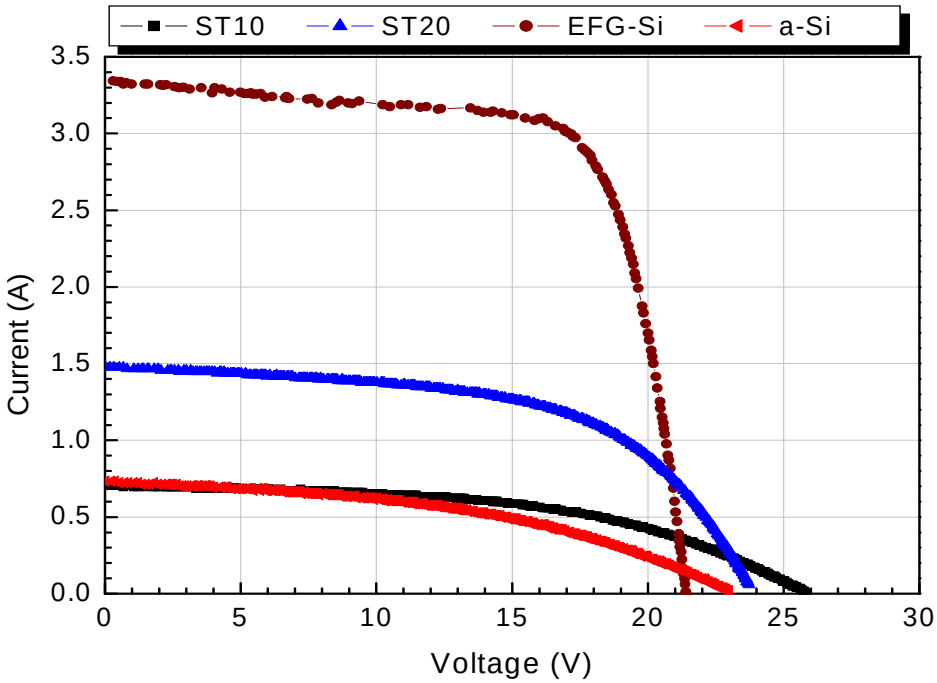

Figure 6.3: *The I-V characteristics of the modules listed in table 6.1.*

Table 6.2: *Electrical parameters of the I-V measurements of the modules used in this study.*

Module	V_{oc} (V)	I_{sc} (A)	P_{max} (W)	FF (%)	η (%)
ST 10	25.97	0.70	9.31	51.22	7.88
ST 20	23.92	1.48	20.11	57.00	8.68
a-Si	23.18	0.73	7.40	43.60	2.51
EFG-Si	21.08	3.19	49.49	73.67	12.69

In order to compare these parasitic resistances and also the fill factors of the modules used in this study, the normalized I-V characteristics of each module were obtained by dividing the voltage and current with the V_{oc} and I_{sc}, respectively. Figure 6.4 shows the normalized I-V characteristics of the modules.

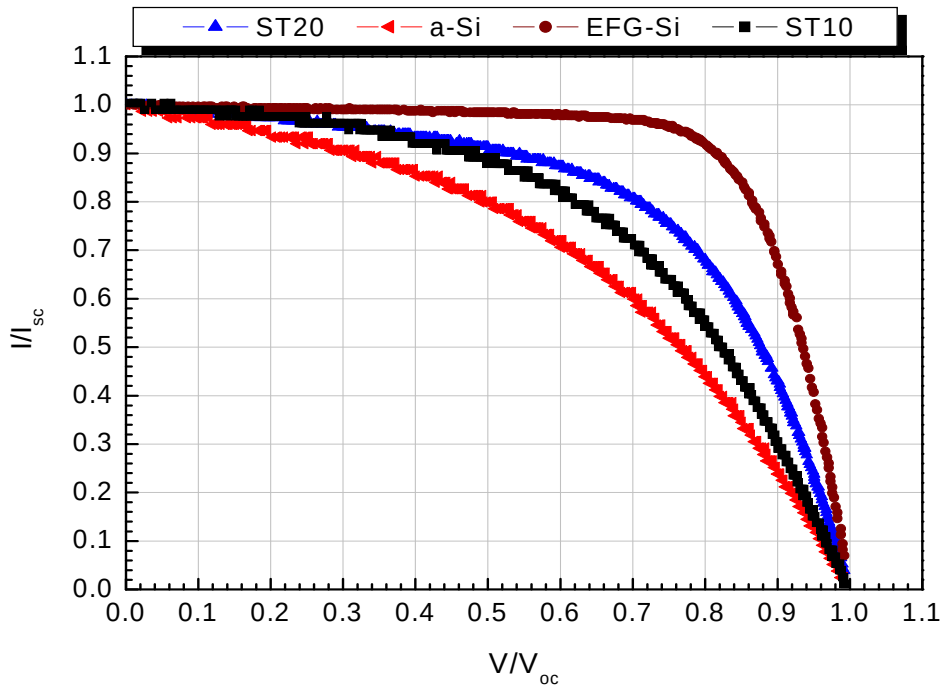

Figure 6.4: *The normalized I-V characteristics of the modules shown in figure 6.3.*

The figure clearly illustrates the differences in the parasitic resistances and the fill factors. It must be noted that such a comparison of normalized I-V data must not be used to qualify one technology as better than the other, but rather as a visual representation of how the parasitic resistances and FF affect the I-V curves. The determination of R_s and R_{sh} is discussed later in this chapter.

6.12.2 The effect of irradiance on PV modules

When PV modules are deployed outdoors, their I-V characteristics change due to the continual changing of the irradiance levels. It is therefore appropriate to perform indoor measurements at different irradiance levels for the PV modules. The irradiance levels affect the efficiency of the module, in that at very high irradiance levels the efficiency is affected by the series resistance, R_s of the cells in the module, while at low irradiance levels, shunt resistance, R_{sh} influences the current, leading to a reduction in efficiency, especially below 300 W/m^2 irradiance levels [McMahon, 1995]. The procedure of measuring module I-V characteristics at different irradiance levels also enables the determination of R_s as described in Chapter 3. The simulator

was used to obtain I-V measurements at different irradiance levels by using four screen filters to reduce the irradiance of the pulsed xenon lamp. The I-V characteristics of the module under test were obtained each time a filter was added between the module and the xenon lamp. The number of filters added determines the irradiance level. Table 6.3 lists the irradiance corresponding to the number of filters. The corresponding measurement errors are also listed.

Table 6.3: *Irradiance levels obtained due to number of filters [Gxasheka, 2003; and Meyer, 2002].*

Number of filters	Irradiance (W/m^2)	Relative Error (%)
0	1000	-
1	614	0.18
2	375	0.17
3	229	0.61
4	169	1.57

Figure 6.5 shows the conversion efficiency as a function of the irradiance level. Often this procedure is helpful to check whether a module has cells that have low shunt resistance. If there were no shunts present within the module, there would be no efficiency losses as the level of irradiance falls below 1000 W/m^2 [McMahon, 1996]. From figure 6.5, it is evident that EFG-Si is the better performer due to the increase in efficiency as irradiance reduces. It is mentioned in the earlier studies that, at low irradiance levels, crystalline modules perform better than the thin-film based modules [Meyer, 2002; 210].

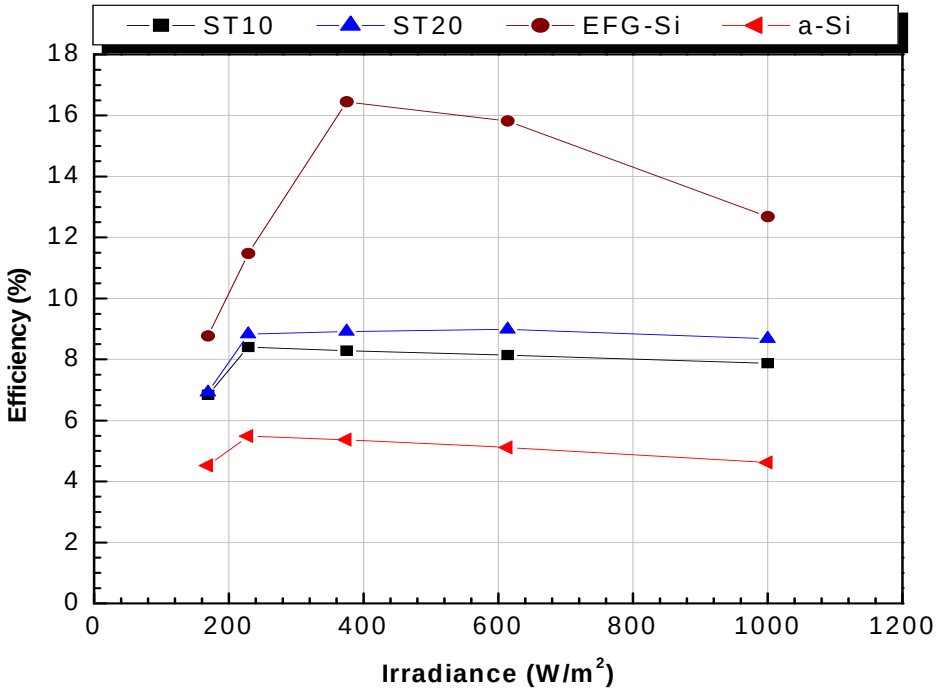

Figure 6.5: *Efficiency of the modules used in this study as a function of irradiance level.*

Figure 6.6 shows the normalized efficiency of the measurements shown in figure 6.5. The efficiencies were normalized to the STC efficiency at 1000 W/m^2. It is clear that the normalized efficiency measurements enable the identification of modules with relatively low shunt resistances. It is shown that efficiency increases with a reduction in irradiance level for all the modules used in this study. This indicates, therefore, that the modules tested are all expected to have cells with high shunt resistance.

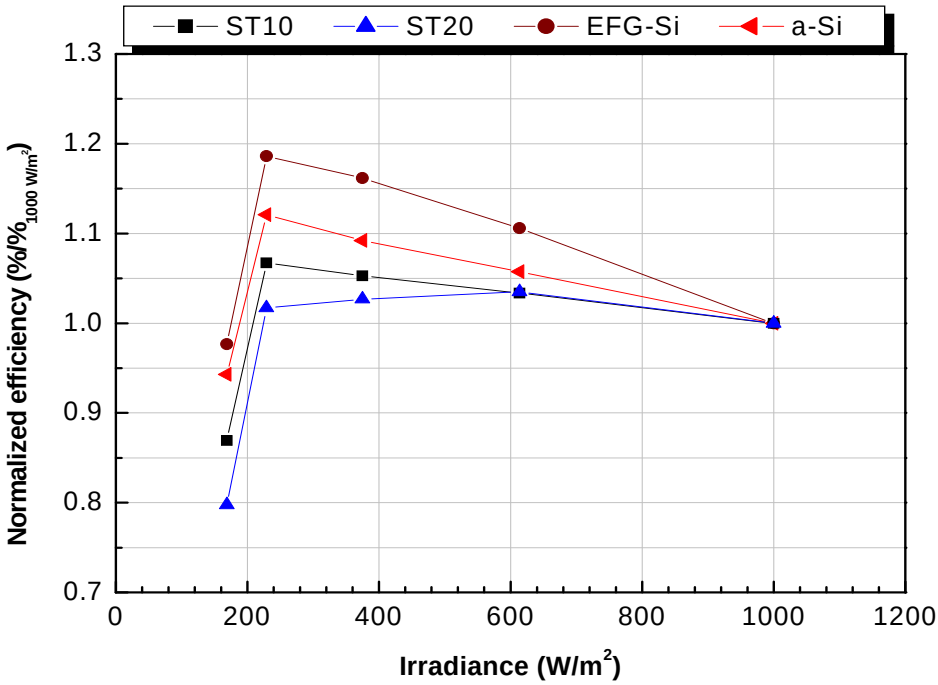

Figure 6.6: *The normalized efficiency as a function irradiance level of the measurements shown in figure 6.5.*

The shunt resistance of a module can also be measured by the Two-terminal diagnostic method of determining the individual cell in the module [McMahon, 1996; Meyer, 2002]. In this study, the determination of the average shunt resistance of a module was done by the method described in Chapter 3. The results are presented in the following section.

6.12.3 The determination of series and shunt resistances

Figure 6.7 shows the I-V characteristics of the 48-cell $CuInSe_2$ module measured with the SPIRE SUN simulator at STC. The slope of the I-V characteristics at I_{sc} indicates R_{sh}, and the slope at V_{oc} indicates R_s, of the module [van Dyk, 2004]. Table 6.4 lists R_{sh} and R_s values using this method for the modules used in this study. This method was used only to estimates R_{sh} and R_s values of the PV modules; it does not give accurate measurements. More accurate methods for determining parasitic resistances of a PV module are discussed below.

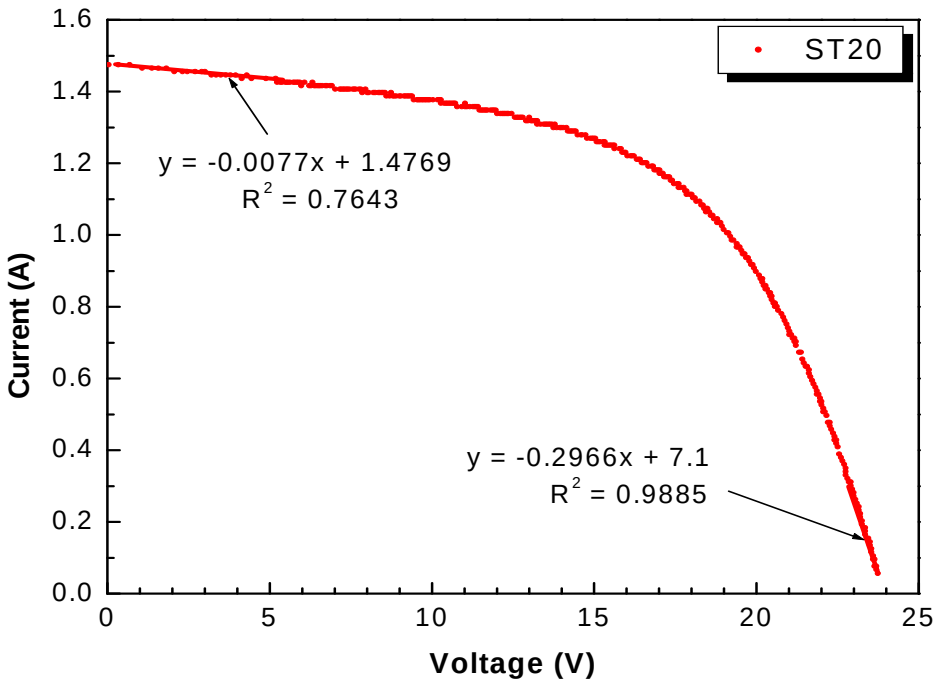

Figure 6.7: *I-V characteristics of ST 20 module measured at STC. Also shown are the linear equations at I_{sc} and V_{oc}.*

Table 6.4: *Parasitic resistances obtained from the slopes of the I-V curves for the modules used in this study.*

Module	R_{sh} (Ω)	R_s (Ω)
ST10	294.11	11.52
ST20	129.87	3.37
a-Si	121.95	12.90
EFG-Si	138.89	0.81

The more accurate methods for determining R_s and R_{sh}, include the method described in Chapter 5 for determining R_{sh} of a PV module, while the method of determining R_s is described in Chapter 3. This method of determining R_s from the slope of the module I-V curves is independent of the R_{sh}, the saturation currents and the ideality factor of the module [Schroder, 1998]. This implies that this method gives better

results as compared to other methods. As an illustrative example, the I-V characteristic measurements of the ST 20 module at different irradiance levels, 614 W/m^2 and 1000 W/m^2, are considered in figure 6.8.

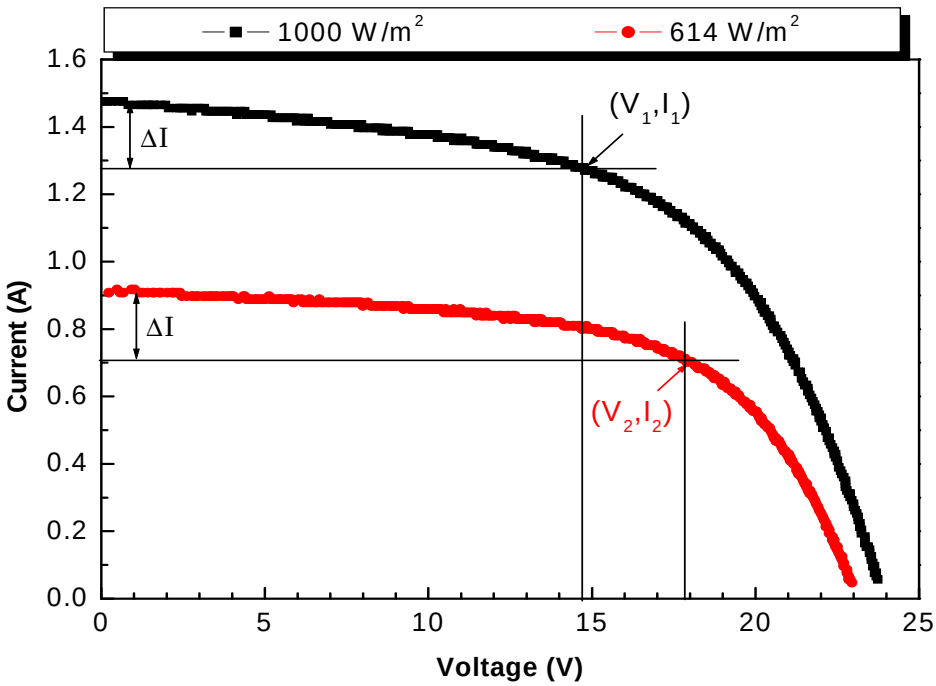

Figure 6.8: *I-V characteristics of a ST 20 module at two irradiance levels, 614 W/m^2 and 1000 W/m^2.*

The fixed current, $\Delta I = 0.2$ A, is the current measured from the respective I_{sc} of each I-V curve. This yields the slope of the I-V curve described by equation 3.27. From equation 3.27:

$$R_s = \frac{V_2 - V_1}{I_1 - I_2}$$

$$= \frac{17.75 - 14.73}{1.28 - 0.71}$$

$$\therefore R_s = 5.32\,\Omega$$

The same procedure was followed to determine R_s of the ST 10, a-Si and EFG-Si modules used in this study, and the results are listed in table 6.5. In each measurements, the fixed current $\Delta I = 0.2$ A was used.

Table 6.5: *R_s obtained from the I-V curves of the tested modules.*

Module	R_s (Ω)
ST10	9.76
ST20	5.32
a-Si	7.93
EFG-Si	0.47

It is, therefore, necessary to compare other methods considered in this study with this method for determining R_s. Table 6.6 summarizes R_s values obtained using the method described in this section and the dark I-V measurements discussed in Chapter 5.

Table 6.6: *R_s measurements obtained from the light and dark I-V characteristics of the modules used in this study.*

Module	R_s (Ω)	
	Light	**Dark**
ST10	9.76	13.21
ST20	5.32	8.62
a-Si	7.93	9.36
EFG-Si	0.47	0.43

From table 6.6 it is clear that the two methods for determining R_s agree with each other. This is indeed the case as the difference between measurements is small for each module. Comparing these measurements with those listed in table 6.4, there is a significant difference for other modules such as EFG-Si. The different can be attributed to the fact that the measurements of R_s and R_{sh} from the slopes of the I-V characteristics give a rough indication of the true values [van Dyk, 2004] although for R_s values are comparable with other methods for determining R_s.

It is interesting to note that the R_s measurements of the thin-film based (ST10, ST20 and a-Si) modules are much larger than the R_s values of the crystalline EFG-Si module. This may be due to the deposition of layers during the fabrication processes of thin film-based modules and due to the fact that they are highly sensitive to daily thermal cycling when deployed outdoors.

EFG-Si module has small R_s as compared to other modules. The study earlier showed that the increasing R_s values reduce the output power and the fill factor of the module leading to the reduction in efficiency [van Dyk, 2004]. EFG-Si with low R_s (= 0.4 Ω) value, has better quality performance compared to other modules studied.

As expected from the I-V curve, a-Si module has high R_s (= 12.9 Ω). This then contributes to its low fill factor. This module when deployed outdoors it is expected to perform poorly. From the methods used, the R_s value for the ST 10 is high (=11.52 Ω) as expected from the I-V curves.

6.13 SUMMARY AND CONCLUSIONS

In this chapter, two copper indium diselenide (CIS) modules were used to investigate light I-V characteristics of the PV modules. The investigation was done with reference to the I-V characterization of PV modules of other technologies, crystalline EFG-Si and amorphous silicon (a-Si) modules. The I-V measurements of the PV modules used were subjected to an indoor assessment procedure and the results were presented and discussed. The measurements included the electrical performance at STC; effect of irradiance levels on PV modules; and the measurement of parasitic resistances.

The electrical performance parameters measured at STC include V_{oc}, I_{sc}, P_{max}, FF and efficiencies of the modules used. These parameters confirmed that the low rated a-Si module has poor quality and the EFG-Si with higher power ratings can perform better when deployed outdoors. From the I-V measurements under reduced simulated

irradiance, it was indicated that the conversion efficiency measured for each of the PV modules used increases with the reduction in irradiance level.

It is, therefore, concluded that I-V characteristics at STC provide a good understanding of the quality of PV modules. The indoor measurement procedure is by a good method of predicting the performance of the PV modules when deployed outdoors.

6.14 REFERENCES

Eagle Technology: www.eagle.co.za

Gxasheka A.R. (2003), *On the monitoring of current-voltage characteristics of photovoltaic modules*, University of Port Elizabeth, MSc-dissertation, pp 66.

McMahon T.J. and Basso T.S. (1995), "Two-terminal diagnostic for cells in series-connected photovoltaic modules," *presented at the ASME International Solar Energy Conference*, Lahaina, HI.

McMahon T.J., Basso T.S. and Rummel S.R. (1996), "Cell shunt resistance and photovoltaic module performance," *Proceedings of the 25th IEEE PV Specialists Conference*, pp 1291-1294.

Meyer E.L. (2002), *On the Reliability, Degradation and Failure of Photovoltaic Modules*, University of Port Elizabeth, PhD-thesis, pp 57.

National Instruments: www.ni.com/**labview**/

Schroder D.K. (1998), *Semiconductor Material and Device Characterization*, John Wiley and Sons, pp 210-211.

Spire Corporation, Bedford, MA. *Spi-Sun Simulator 240 Solar Panel I-V System, Installation, operation and maintenance manual.*

van Dyk E.E. and Meyer E.L. (2004), "Analysis of the effect of parasitic resistances on the performance of Photovoltaic Modules," *Renewable Energy*, **29**, pp 333-344.

CHAPTER 7

CONCLUSIONS

The primary objective of this study was to develop an assessment procedure capable of describing the current-voltage (I-V) characteristics of $CuInSe_2$ solar cells and modules and other photovoltaic (PV) modules of different technologies. The outline was as follows:

- Design, build and use a system capable of performing dark I-V characteristics of PV modules.
- To utilize and modify the system used to perform light I-V characteristics of PV modules.
- To study the effects of parasitic resistance and irradiance on the I-V characteristics of solar cells and PV modules.

The system was designed and implemented for performing dark I-V characteristics of PV modules. The motive to build and implement the system capable of performing a full dark I-V profile, was due to the failure of the system described in section 5.3 for which the instruments allowed measurements below 10^{-2} A. The dark I-V system built allowed current measurements above 10^{-2} A of the dark I-V characteristics of PV modules. The results have showed that the dark I-V profile was extended to four orders of magnitude. The stability of this system enabled the determination of shunt and series resistances influence on PV modules.

An investigation on the influence of temperature on the of PV module showed that some of the modules are affected in different parts of their dark I-V characteristics. This was the case for ST 10, ST 20 and EFG-Si modules.

The light I-V measurements were performed using the solar simulator to measure I-V characteristics at standard test conditions (STC) and to study the effects of irradiance on each of the module used in this study. The results showed that the modules used in

this study have cells with high shunt resistances. This was concluded from the fact that in all modules the efficiency increases as the irradiance levels reduced.

The results obtained in this study proved that I-V characteristics of a PV device can predict the device performance when deployed outdoors. Finally, this study shows that I-V characteristics of a solar cell and PV module can be regarded as a useful tool to better understand the device parameters.

APPENDIX A

CALIBRATION RESULTS OF THE DARK CURRENT-VOLTAGE MEASUREMENTS SYSTEM

A.1: Introduction

The calibration results of the dark current-voltage system described in Chapter 5, is given below.

A.2: Calibration algorithm

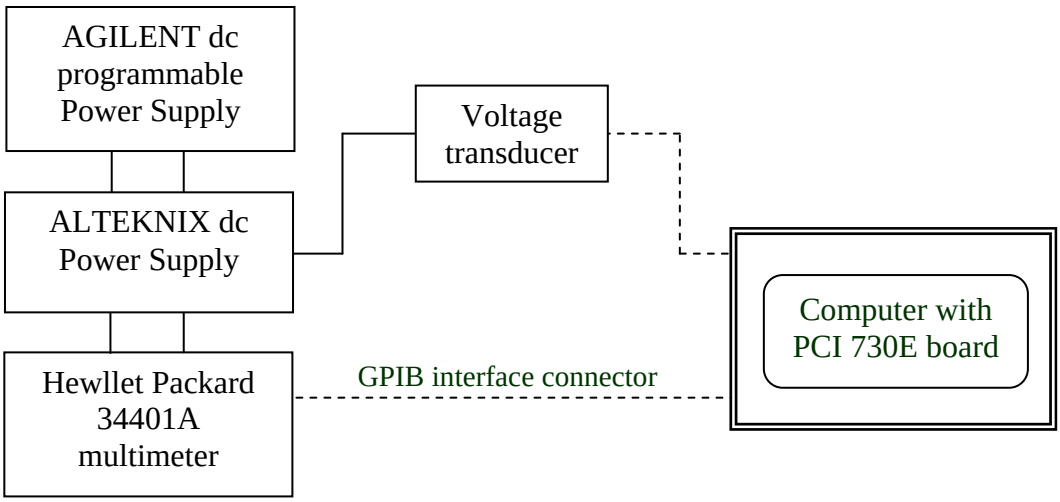

Figure A.1: *Schematic representation for voltage calibration.*

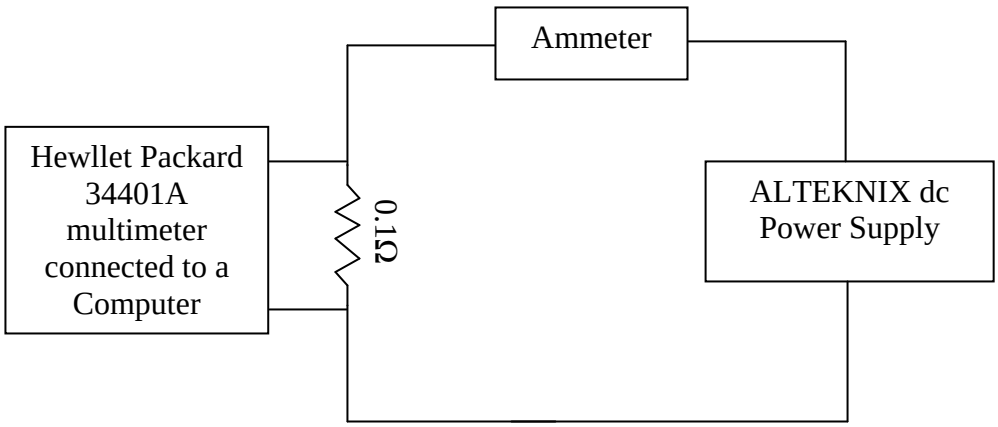

Figure A.2: *Schematic representation for current calibration.*

Voltage calibration

- ✓ Programmable power supply was connected to the back panel of the 60/30 power supply: positive to *'10V INPUT'* and negative to *'COM'*;
- ✓ Front panel output terminals were connected to the input terminals of the voltage transducer;
- ✓ Manually, the front panel voltage was set to maximum;
- ✓ Digital multimeter was connected across output terminals to monitor the voltage measurements;
- ✓ The computer program controlled the programmable power supply, which in turn driven the 60/30 power supply;
- ✓ The computer measured and recorded the 60/30 power supply voltage and the transduced voltage (using PCI730E data acquisition card);
- ✓ The controlled power supply voltage (PSU voltage) and transduced voltage (V_{trans}) plot, is shown in figure 5.7.
- ✓ The linear equation (i) shown in the table below was obtained and was incorporated into the software program of measuring I-V curve

Current calibration

- ✓ Front panel terminals of the 60/30 power supply were connected in series with the 0.1Ω resistor wire;
- ✓ The ammeter was connected to measure the current through the circuit;
- ✓ Manually, the current was controlled using the front panel current control;
- ✓ Voltage drop across the resistor was recorded as the controlled current changed;
- ✓ Figure 5.7a show the relation between the voltage drop across the resistor and current through the circuit;
- ✓ Figure 5.7b illustrate the stability of the measurements
- ✓ The linear equation (ii) shown below was obtained which was incorporated into the software program of measuring I-V curve

A.3: Calibration curves

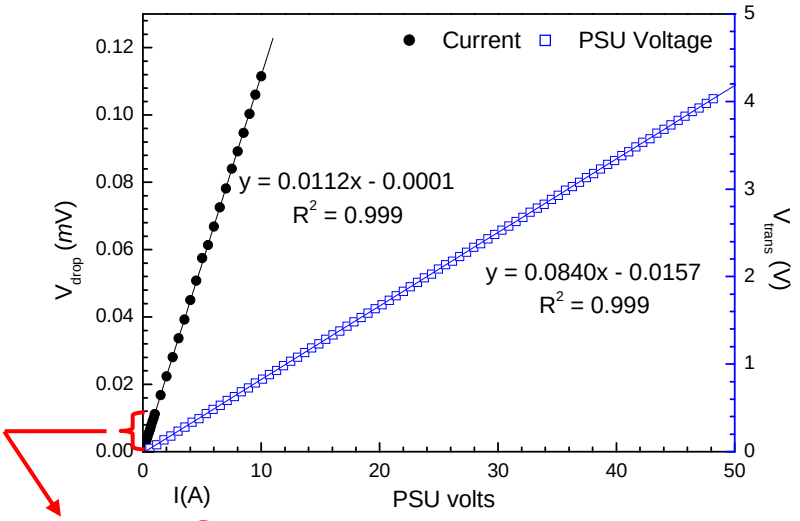

Figure A.3: *Calibration of voltage and current measurements.*

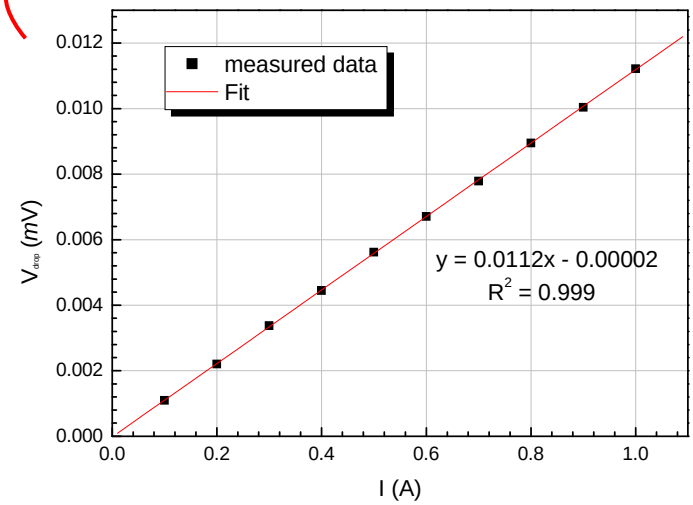

Figure A.4: *Stability curve of current measurements in the region indicated in figure A.3.*

$$V_{trans} = 0.0840V_{PSU} - 0.0157 \quad \textbf{A.1}$$

$$V_{drop} = 0.0112I - 0.00002 \quad \textbf{A.2}$$

APPENDIX B

ALGORITHM OF THE DARK CURRENT-VOLTAGE MEASUREMENTS SYSTEM

The programme for obtaining the dark current-voltage measurements was written in LabVIEW as was indicated in Chapter 5. The algorithm of the guide instructions is given below.

Setup connections

HP 34401A Multimeter

- Selecting GPIB address 22:
-
    - turn on the **MENU** by pressing [Shift] [>]
    - scroll to **E: 1/0 MENU** using [>]
    - access the commands level within **E: 1/0 MENU** using [v]
    - move to the **1: HP – 1B ADDR** command within this level using [>]
    - use [v] to move down to edit ADDR parameter
    - move the flashing cursor over to edit and set ADDR 22 using [>] [v]
    - then [Auto/ Man] to save changes.

Check by switching Power button Off and On to see if the correct ADDRESS has been chosen.

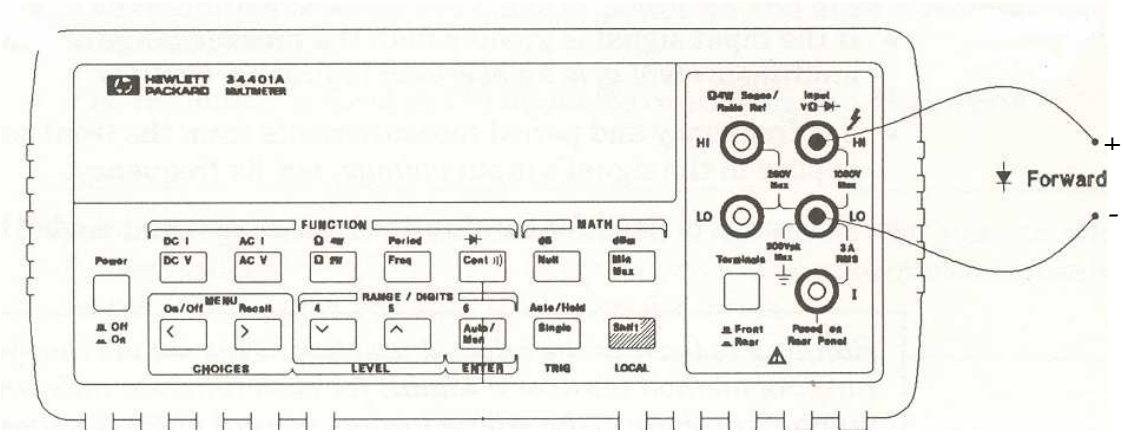

Agilent E3646A Dual Output DC Power Supply

- Selecting RS-232:

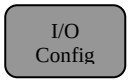

- ➢ and use the knob to move across to the RS-232
- ➢ to select RS-232 and confirm 9600 BAUD & NONE 8 BITS

Check by switching Power button Off and On to see if the RS-232 has been set.

Curve capturing

- ✓ Open **DarkIV** LabView file from ***Dark IV system*** folder;
- ✓ And follow the instructions given on the program

APPENDIX C

RESEARCH OUTPUTS ASSOCIATED WITH THIS STUDY

National Conference : N. M. Thantsha and E. E. van Dyk
"Shunt resistance measurements of the CuInSe2-based solar cells and modules"
49th South African Institute of Physics Conference, University of Free State, Bloemfontein (2004)

N. M. Thantsha and E. E. van Dyk
"Investigating electrical parameters in the photovoltaic modules"
50th South African Institute of Physics Conference, University of Pretoria (2005)

General Presentations : N. M. Thantsha
"The influence of parasitic resistances on the performance of solar cells"
UPE Physics Seminar Series No. 34 (2004)

Publications : N. M. Thantsha and E. E. van Dyk, *" Analysis of electrical characteristics of photovoltaic modules,"* South African Journal of Science, **101**, pp 288-289.